















Characterization of low-mass companions to *Kepler* objects of interest observed with APOGEE-N

CALEB I. CAÑAS ^{1,2,3,*} CHAD F. BENDER ⁴ SUVRATH MAHADEVAN ^{2,3,5} DMITRY BIZYAEV ^{6,7}
NATHAN DE LEE ^{8,9} SCOTT W. FLEMING ¹⁰ FRED HEARTY ^{2,3} STEVEN R. MAJEWSKI ¹¹
CHRISTIAN NITSCHHELM ¹² DONALD P. SCHNEIDER ^{2,3} JAVIER SERNA ¹³ KEIVAN G. STASSUN ⁹
GUÐMUNDUR STEFÁNSSON ^{14,†} GUY S. STRINGFELLOW ¹⁵ AND JOHN C. WILSON¹¹

¹*NASA Goddard Space Flight Center, 8800 Greenbelt Road, Greenbelt, MD 20771, USA*

²*Department of Astronomy & Astrophysics, The Pennsylvania State University, 525 Davey Laboratory, University Park, PA 16802, USA*

³*Center for Exoplanets and Habitable Worlds, The Pennsylvania State University, 525 Davey Laboratory, University Park, PA 16802, USA*

⁴*Steward Observatory, The University of Arizona, 933 N. Cherry Avenue, Tucson, AZ 85721, USA*

⁵*ETH Zurich, Institute for Particle Physics & Astrophysics, Zurich, Switzerland*

⁶*Apache Point Observatory and New Mexico State University, P.O. Box 59, Sunspot, NM, 88349-0059, USA*

⁷*Sternberg Astronomical Institute, Moscow State University, Moscow*

⁸*Department of Physics, Geology, and Engineering Technology, Northern Kentucky University, Highland Heights, KY 41099, USA*

⁹*Department of Physics & Astronomy, Vanderbilt University, Nashville, TN 37235, USA*

¹⁰*Space Telescope Science Institute, 3700 San Martin Dr., Baltimore, MD 21218, USA*

¹¹*Department of Astronomy, University of Virginia, Charlottesville, VA 22904, USA*

¹²*Centro de Astronomía (CITEVA), Universidad de Antofagasta, Avenida Angamos 601, Antofagasta 1270300, Chile*

¹³*Instituto de Astronomía, Universidad Autónoma de México, Ensenada, B.C, México*

¹⁴*Department of Astrophysical Sciences, Princeton University, 4 Ivy Lane, Princeton, NJ 08540, USA*

¹⁵*Center for Astrophysics and Space Astronomy, Department of Astrophysical and Planetary Sciences, University of Colorado, Boulder, CO 80309, USA*

ABSTRACT

We report the characterization of 28 low-mass ($0.02 M_{\odot} \leq M_2 \leq 0.25 M_{\odot}$) companions to *Kepler* objects of interest (KOIs), eight of which were previously designated confirmed planets. These objects were detected as transiting companions to Sun-like stars (G and F dwarfs) by the *Kepler* mission and are confirmed as single-lined spectroscopic binaries in the current work using the northern multiplexed Apache Point Observatory Galactic Evolution Experiment near-infrared spectrograph (APOGEE-N) as part of the third and fourth Sloan Digital Sky Surveys. We have observed hundreds of KOIs using APOGEE-N and collected a total of 43,175 spectra with a median of 19 visits and a median baseline of ~ 1.9 years per target. We jointly model the *Kepler* photometry and APOGEE-N radial velocities to derive fundamental parameters for this subset of 28 transiting companions. The radii for most of these low-mass com-

panions are over-inflated (by $\sim 10\%$) when compared to theoretical models. Tidally locked M dwarfs on short period orbits show the largest amount of inflation, but inflation is also evident for companions that are well separated from the host star. We demonstrate that APOGEE-N data provides reliable radial velocities when compared to precise high-resolution spectrographs that enable detailed characterization of individual systems and the inference of orbital elements for faint ($H > 12$) KOIs. The data from the entire APOGEE-KOI program is public and presents an opportunity to characterize an extensive subset of the binary population observed by *Kepler*.

1. INTRODUCTION

Precise physical parameters, including the mass and radius, are important to understand the formation and evolution low-mass M dwarfs and brown dwarfs. M dwarfs are primary targets for recent spectroscopic and photometric surveys, such as Mearth (Irwin et al. 2015), NGTS (Wheatley et al. 2018), SPECULOOS (Delrez et al. 2018), CARMENES (Reiners et al. 2018), and the Habitable-zone Planet Finder (HPF; Mahadevan et al. 2012, 2014), because their smaller radii and masses relative to Sun-like stars yield deeper transits and larger RV amplitudes, which facilitates the detection of exoplanets in these systems. M dwarfs are also lucrative targets for the search for habitable planets because their habitable zones are closer-in than Sun-like stars (e.g., Kopparapu et al. 2013, 2017; Wandel 2018).

The characterization of any exoplanetary system is fundamentally limited by how well the stellar parameters (including the mass, radius, and age) can be constrained. Accurate stellar radii and masses are required to derive accurate planet radii and masses, which are necessary to understand the population of exoplanets. Some examples which require precise planetary parameters include refining the mass-radius relationship for exoplanets (e.g., Chen & Kipping 2017; Wolfgang et al. 2016; Kanodia et al. 2019; Ulmer-Moll et al. 2019), inferring atmospheric

properties (Batalha et al. 2019), or recovering the planetary interior structure (e.g., Dorn et al. 2015; Otegi et al. 2020).

Brown dwarfs are objects with masses spanning $\sim 13 M_J < M < \sim 80 M_J$, where the lower and upper mass limits are the deuterium-burning and hydrogen-burning mass limits, respectively (e.g., Chabrier et al. 2014; Baraffe et al. 2015). The “brown dwarf desert” is the low occurrence rate ($\lesssim 1\%$) of brown dwarfs as companions to Sun-like stars on close orbits (< 5 au) and it has been extensively studied via radial velocity surveys (e.g., Grether & Lineweaver 2006; Troup et al. 2016; Grieves et al. 2017; Triaud et al. 2017; Kiefer et al. 2019, 2021) and transit surveys (Sahlmann et al. 2011; Csizmadia & CoRot Team 2016; Santerne et al. 2016). This feature may be correlated with the transition in the formation processes of gas giants and stars but the limited number of brown dwarfs with precisely determined ($> 3\sigma$) properties has prevented a detailed statistical analysis of the population (e.g., Ma & Ge 2014; Maldonado & Villaver 2017). Additional brown dwarf systems with precise masses and radii to increase the population of transiting brown dwarfs will be useful to examine if formation mechanisms have a role in the observed desert.

The physical parameters for low-mass stars and brown dwarfs are often derived using evolutionary models (e.g., Baraffe et al. 2015) and the uncertainties in these models or relationships will extend to the derived planetary parame-

* NASA Postdoctoral Program Fellow

† Henry Norris Russell Fellow

ters. The theoretical mass-radius relationships for M dwarfs are known to be insufficient to accurately derive the parameters of M dwarfs for exoplanetary studies (e.g., López-Morales 2007; Parsons et al. 2018) and have motivated empirical mass-radius relationships (e.g., Stassun et al. 2012; Mann et al. 2015, 2019) for low-mass stars. Theoretical models for brown dwarfs have similarly shown scatter in the mass-radius relationship (e.g., Burrows et al. 2011; Marley et al. 2021). A larger sample of very low-mass M dwarfs and brown dwarfs with accurate fundamental parameters, including mass and radius, are required to reliably calibrate and improve the predictions from existing theoretical relationships. Direct measurements of these parameters are beneficial for our theoretical understanding of these stars and substellar companions and can constrain the set of plausible stellar evolutionary models (e.g., Torres et al. 2010; Stevens et al. 2018).

In this paper, we present stellar parameters for a subset of objects from a spectroscopic survey of *Kepler* objects of interest (KOIs) outlined by Fleming et al. (2015) and conducted as part of the Sloan Digital Sky survey IV (Blanton et al. 2017). Our sample includes brown dwarfs and fully convective M dwarf companions to F and G host stars. We present a summary of the spectroscopic survey, derive stellar and orbital parameters for the systems, and compare the fundamental parameters to the predictions of evolutionary models. The paper is structured as follows: Section 2 describes the spectroscopic survey and the subset of targets presented in this work while Section 3 provides a description of all observations. Section 4 provides a discussion of the models and fit to photometry and RVs. In Section 5 we compare the derived properties to theoretical models for brown dwarfs and low-mass stars while in Section 6 we provide further discussion of the nature of these

transiting brown dwarfs and M dwarfs. We end with a summary of our key results in Section 7.

2. THE APOGEE-KOI PROGRAM

The *Kepler* mission (Borucki et al. 2010; Koch et al. 2010) was launched in 2009 to examine the frequency of Earth-sized exoplanets within the habitable zone of their host stars (Bryson et al. 2021). It has revolutionized our understanding of exoplanets and stars by providing nearly continuous observations of $\sim 200,000$ stars. The photometric observations of most stars were conducted in long cadence mode (~ 29.4 minutes) with exquisite precision (~ 80 ppm for 6 hour timescales of Sun-like stars; see Christiansen et al. 2012) that are well suited for planetary and asteroseismic analysis. In its final data release (DR25; Thompson et al. 2018), *Kepler* identified > 8000 *Kepler* objects of interest (KOIs), or periodic transit-like events that were most likely astrophysical in nature.

To address the difficulty of removing false positive signals from genuine planetary candidates, candidate vetting and validation are used to identify the signals with the highest probability of being genuine planets. Vetting of KOIs can be performed without additional data by relying on high-quality space-based photometry (e.g., the existence of a deep secondary eclipse, centroid offsets, or ellipsoidal variations, Bryson et al. 2013; Mullally et al. 2016b; Thompson et al. 2018) or with additional data from programs designed to characterize KOIs, including spectroscopic observations (e.g., Ehrenreich et al. 2011; Matson et al. 2017; Petigura et al. 2017), photometric deblending (e.g., Torres et al. 2011; Kirk et al. 2016), or adaptive-optic observations (Law et al. 2014; Ziegler et al. 2017, 2018). Candidate validation evaluates a transiting signal for common signs of false positive scenarios (e.g., background eclipsing binaries or hierarchical eclipsing binaries) using constraints from photometry or external datasets including RVs and high-contrast imaging. Al-

gorithms designed to statistically validate KOIs include BLENDER (Torres et al. 2011), VESPA (Morton 2012), and PASTIS (Díaz et al. 2014; Santerne et al. 2015).

Only VESPA has been applied to the entire KOI sample (Morton et al. 2016) but not all validated signals are genuine planets (e.g., Cañas et al. 2018). The mass of the transiting companion is one of the most important dynamical probes to determine if a KOI is a genuine planet or an astrophysical false positive (a stellar binary, e.g., Fleming et al. 2015; Parviainen et al. 2019). A traditional RV spectrograph observes one object at a time and limits surveys to either extensively observe a small subset of KOIs (e.g., Santerne et al. 2016) or to sparsely observe (≤ 2 epochs) a much larger population (e.g., Petigura et al. 2017). We designed the APOGEE-KOI program (Fleming et al. 2015) to address the bottleneck in spectroscopic follow-up of the KOI program. It was a pilot program under the third Sloan Digital Sky Survey (SDSS-III; Eisenstein et al. 2011) and an ancillary program as part of the fourth Sloan Digital Sky Survey (SDSS-IV; Blanton et al. 2017).

This program used the northern Apache Point Observatory (APO) Galactic Evolution Experiment (APOGEE) spectrograph (APOGEE-N; Wilson et al. 2012, 2019) located on the Sloan 2.5-meter telescope (Gunn et al. 2006) at APO. APOGEE-N was designed for the original APOGEE survey to conduct a detailed chemical and kinematic study of the galactic stellar population by observing $\sim 146,000$ red giant stars (Majewski et al. 2017; Zasowski et al. 2017). APOGEE-N is a multi-object, fiber-fed, near-infrared spectrograph capable of observing up to three hundred objects simultaneously at high-resolution ($R \sim 22,500$) in the H-band (1.514 – 1.696 μm). It achieves a radial velocity precision of $\lesssim 0.5 \text{ km s}^{-1}$ for most stars with $H < 15$ and an RV precision of $\sim 100 \text{ m s}^{-1}$ for stars with $H < 11$ (see Jönsson et al. 2020).

APOGEE-N achieves an average signal-to-noise ratio per pixel of 100 on a $H = 11$ star in a single visit with one hour of total integration time.

As discussed in Majewski et al. (2017), the design of the APOGEE-N spectrograph and the bandpass enable various ancillary science projects within the survey. The field-of-view (FOV) for APOGEE-N has a radius of 1.49° which coincidentally provides an opportunity to use the multiplexing capabilities of APOGEE-N and simultaneously observe multiple KOIs from one *Kepler* CCD module. A *Kepler* CCD module is approximately the same size as the APOGEE-N FOV. The multiplexing also makes APOGEE-N more efficient (~ 3 times more efficient; Fleming et al. 2015) than high-precision single-target spectrographs at achieving an RV precision of $\gtrsim 100 \text{ m s}^{-1}$. The primary science goals of the APOGEE-KOI program are presented in Fleming et al. (2015) and include (i) dynamical vetting and refinement of KOIs, (ii) searching for any dependencies on disposition with stellar or candidate parameters, and (iii) improving our understanding of binarity rates and the effects of stellar multiplicity on the planet host population.

The APOGEE-KOI program began in 2013 under SDSS-III and completed observations in 2020 as part of SDSS-IV. It targeted ~ 1600 KOIs for a median of 19 epochs per target and a median baseline of 683 days (1.87 years). The *Kepler* field is only accessible for observations over a limited range of local sidereal time (LST) for ground-based observations. The bulk of the observations with the APOGEE-N spectrograph for our program occurred between LSTs of 18 – 20 hours where over-subscription with other APOGEE programs ultimately set the temporal baseline for the various APOGEE-KOI fields.

The targets for the APOGEE-KOI program include confirmed planets, planetary candidates, and false positive systems. Figure 1

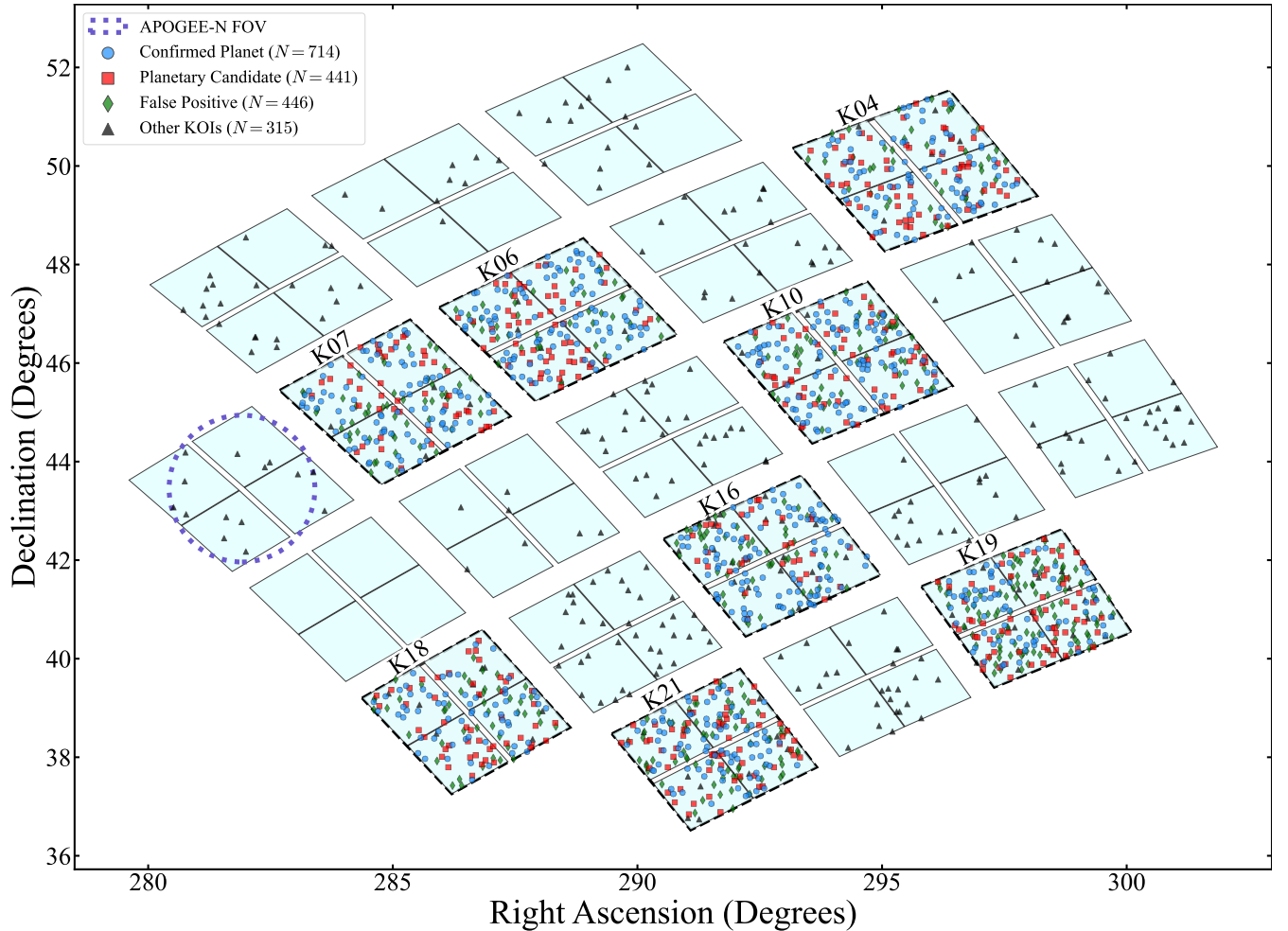


Figure 1. A plot of the KOIs listed in Table 1 and observed by our program overlaid on the *Kepler* footprint from Mullally et al. (2016a). The APOGEE-KOI field is listed above the CCD modules from the *Kepler* field observed as part of our program between 2013 – 2020. The 1.49° APOGEE-N FOV is plotted as a dotted circle. The marker reflects the DR25 disposition from the NASA Exoplanet Archive. The APOGEE-KOI program observed 714 confirmed planets (blue circles), 441 planetary candidates (red squares), and 446 false positives (green diamonds) for a median of 19 visits. For reference, KOIs not observed as part of this program but observed multiple times with APOGEE-N are shown as black triangles.

displays the observed *Kepler* footprint¹ along with the targets observed with APOGEE-N. The KOIs in these fields were chosen based on various characteristics. Selection of a KOI for the survey required (i) a disposition from the

¹ <https://keplergo.github.io/KeplerScienceWebsite/the-kepler-space-telescope.html#field-of-view>

NASA Exoplanet Archive² of either planetary candidate, confirmed planet, or false positive, (ii) an H-band magnitude < 14 , (iii) a position within the field of view of the instrument (1.5° from the center of each module), (iv) a position greater than $100''$ from the center of the plug plates, and (v) a separation from other targets

² The KOI catalogs used to identify targets were dated July 2013 for K16, K10, and K21, March 2016 for K04, February 2017 for K06 and K07, and April 2018 for K18 and K19.

larger than $\sim 72''$. These requirements were placed to ensure targets (i) would have a signal-to-noise ratio (SNR) that could ensure single-visit precision $< 0.5 \text{ km s}^{-1}$, (ii) lie within the plate boundary, and (iii) that fibers were separated enough to physically allow for drilling the position on aluminum plug plates (see Owen et al. 1994). Fiber collision errors (when the targets were separated by less than $\sim 72''$) were avoided by prioritizing targets using *Kepler* disposition and magnitude. Confirmed planets had the highest priority, followed by planetary candidates, and then false positive systems with a preference for cooler host stars. If any two conflicting targets had the same disposition, we preferentially selected the KOI with a brighter *Kepler* magnitude. In each field we were able to accommodate all confirmed and planetary candidate KOIs, barring any fiber collisions. This selection criteria provides > 200 KOIs per plate with a small number of fibers (10–30) allocated to stars observed by *Kepler* but not known to have transiting companions (no disposition in the respective KOI list), other APOGEE programs, or for telluric and sky calibration. We note that the selection criterion slightly changed as the APOGEE-KOI program progressed because the *Kepler* team refined its KOI pipeline.

CCD Module K16 was observed as part of SDSS-III and a description of the APOGEE-KOI program with preliminary results was reported by Fleming et al. (2015). The observations for CCD module K16 began in September 2013 and were completed in June 2014 while observations for CCD modules K10 and K21 began in October 2014 and were completed in April 2017. Observations for CCD modules K04, K06, and K07 began in May 2017 and ended early 2019. An expansion of APOGEE-N programs (see Beaton et al. 2021) to fill an excess of bright time allowed for the inclusion of two additional fields, K18 and K19, which were observed between 2019 and 2020. The targets

in our program can be identified in the DR17 (Abdurro’uf et al. 2022) allStar catalog³ with the target flags APOGEE_RV_MONITOR_KEPLER (for module K16) or APOGEE2_KOI for all other CCD modules. For ease of reference, Table 1 provides a list of the stars, including non-KOIs, observed as part of the APOGEE-KOI program and various identifiers (2MASS, KIC, TIC, Gaia DR3).

3. OBSERVATIONS

In this manuscript, we present an analysis of a subset of the APOGEE-KOI program: the 28 KOIs listed in Table 2. These KOIs were selected for further analysis based on a fit of the Keplerian radial velocity (RV) curve to the derived APOGEE-N RVs (see Section 3.3) using *radvel* (Fulton et al. 2018). In this fit, the ephemeris was fixed to the value contained in the DR25 KOI catalog. Using the best-fitting orbital parameters and the DR25 stellar table provided by Mathur et al. (2017), we estimated the $M_2 \sin i$ for the observed KOI sample. The targets selected for analysis were KOIs found to have low-mass ($M_2 < 0.25 M_\odot$) transiting companions that had (i) no indication of secondary light in the APOGEE-N spectra (e.g., no additional peaks in the cross-correlation function) and (ii) deep occultations identified by the *Kepler* team. We selected this sample to ensure the system had a negligible flux ratio and could be modeled as a single-lined spectroscopic binary.

3.1. Photometry with *Kepler*

Kepler observed our targets for the entirety of the original mission in long-cadence mode (30 min cadence) with data from 2009 May 13 through 2013 May 11. Some targets were ob-

³ https://data.sdss.org/datamodel/files/APOGEE_ASPCAP/APRED_VERS/ASPCAP_VERS/allStar.html

Table 1. Stars observed by the APOGEE-KOI program.

APOGEE ID	KIC ID	KOI	<i>Kepler</i> Name ^a	TIC	Gaia DR3	Visits	Temporal Baseline (days)	S/N ^b	Disposition ^c	Module ^d
2M19494889+4100395	5812701	12	Kepler-448	169461816	2073860662955260416	18	768	109	CONFIRMED	K19
2M19075308+4652061	9941662	13	Kepler-13	158324245	2130632159136095104	25	2664	155	CONFIRMED	K06
2M18523991+4524110	9071386	23		164458426	2107001760170220032	18	683	68	FALSE POSITIVE	K07
2M19170279+4748558	10593759	25		158984684	2127940314153495680	18	661	41	FALSE POSITIVE	K06
2M19083956+3922369	4247791	28		121121622	2100409638208481536	15	1623	123	FALSE POSITIVE	K18
2M19475229+4055363	5725087	33		168813467	2076775949311326592	20	1506	342	FALSE POSITIVE	K19
2M19253263+4159249	6521045	41	Kepler-100	159654016	2101733244046205568	28	452	104	CONFIRMED	K16
2M18523616+4508233	8866102	42	Kepler-410 A	164458714	2106904148451706752	23	2503	109	CONFIRMED	K07
2M19285977+4609535	9527334	49	Kepler-461	63206513	2126801563705846528	20	1861	33	CONFIRMED	K10
2M19254039+3840204	3544595	69	Kepler-93	137151335	2052747119115620352	21	1928	287	CONFIRMED	K21
⋮										
2M19554332+3959497	4866028			171500649	2073514248077061632	7	1116	95		K19
2M19560588+4127518	6152072			171512615		7	1116	112		K19
2M19563075+4149418	6471048			171968838	2075370945254291200	7	2244	84		K19
2M19563429+4014532	5130305			171878493	2073541387961862272	7	1116	120		K19
2M19565344+4202296	6637066			268493357	2075380565981543680	29	2690	257		K19
2M19570991+4022505	5219533			171977166	2073549432450598656	20	1506	208		K19
2M19572477+4038084	5479821			171975736	2075057721882739456	7	1116	122		K19
2M19580129+4139138	6315593			172378715	2075172345974035840	22	1506	179		K19
2M19582041+4012465	5132589			172426403	2074282596228937856	7	1116	138		K19
2M19582996+4037459	5481306			172423983	2075048376034233600	19	768	8		K19
2M19583347+4028296	5309121			172424885	2075037621435984000	7	1116	132		K19

NOTE—This table is published in its entirety in the machine-readable format and contains 2279 entries. A portion is shown here for guidance regarding its form and content.

^a The *Kepler* name from the NASA Exoplanet Archive^a.

^b The median S/N per pixel of all visits from the `allVisit` catalog^b.

^c NASA Exoplanet Archive disposition of the first transiting signal from the supplemental DR25 table^c.

^d The *Kepler* CCD module as identified in Figure 1.

^a https://exoplanetarchive.ipac.caltech.edu/docs/API_keplernames_columns.html

^b https://data.sdss.org/datamodel/files/APOGEE_ASPCAP/APRED_VERS/ASPCAP_VERS/allVisit.html

^c https://exoplanetarchive.ipac.caltech.edu/docs/PurposeOfKOITable.html#q1-q17_sup_dr25

served in short-cadence (2 min cadence) mode. A summary of the photometry used in this work is included in Table 2. The *Kepler* team used a fully automated vetting pipeline (see Coughlin et al. 2016; Mullally et al. 2016b; Twicken et al. 2016) designed to maximize the reliability of the final catalog.

For the analysis in this manuscript, we use the entire pre-search data-conditioned (PDC-SAP; Stumpe et al. 2012; Smith et al. 2012) light curves available at the Mikulski Archive for Space Telescopes (MAST). We use the PDCSAP light curves from all available quarters of *Kepler* and exclude observations with non-zero data quality flags. These flags indicate poor-quality data due to conditions such as spacecraft events or cosmic ray hits and are described in the *Kepler* Archive Manual (see Table 2-3 in Thompson et al. 2016). We do not perform additional processing or apply outlier rejection beyond the data quality flags. The detrending of the raw photometry is described in detail in Appendix A. General information for each target is listed in Table 3.

3.2. Adaptive optics imaging with Robo-AO

23 KOIs (see Table 3) were observed as part of the Robo-AO *Kepler* planetary candidate survey (Law et al. 2014; Baranec et al. 2016; Ziegler et al. 2017, 2018).⁴ These observations were performed using the Robo-AO laser adaptive optics system (Baranec et al. 2013, 2014) on the 2.1-m telescope at Kitt Peak National Observatory (Jensen-Clem et al. 2018) with a 1.85-m circular aperture mask on the primary mirror. The typical seeing at the Kitt Peak Observatory is between 0.8 – 1.6", with a median seeing of 1.3" (Jensen-Clem et al. 2018) while the typical diffraction limited FWHM resolution of the Robo-AO system is 0.15" (Ziegler et al. 2018). Robo-AO observed most of these KOIs using

a long-pass filter with a hard cut off at 600 nm that was designed to approximate the *Kepler* bandpass at redder wavelengths and suppress blue wavelengths to minimize the impact on adaptive optics performance. KOI-1356 was observed using the Sloan *i'* filter. The adaptive optics data set acquired by Robo-AO was reduced using the Robo-AO pipeline (Law et al. 2014) which (i) performs PSF subtraction, (ii) perform an automated search for companions, and (iii) calculates constraints of the nearby star sensitivity with a 5σ contrast curve. Ziegler et al. (2018) presents a detailed description of the data reduction pipeline.

3.3. Doppler spectroscopy with APOGEE-N

For this work, we use the publicly available DR17 data⁵. The APOGEE data pipeline (Nidever et al. 2015) performs sky subtraction, telluric and barycentric correction, and wavelength and flux calibration for each observation and has been shown to achieve a typical RV precision of ~ 100 m s⁻¹ for most stars with $H < 11$ (Jönsson et al. 2020). In this work, we do not use archival DR17 RVs but instead derive RVs using the processed DR17 spectra (the `apVisit` files⁶). While the APOGEE data pipeline provides radial velocity measurements, we performed additional post-processing on the spectrum to remove residual sky emission lines prior to analysis and derive RVs following the procedure described in Cañas et al. (2019a). Briefly, we identified the best-fit synthetic spectrum by cross-correlating the highest S/N spectra using synthetic spectra generated from MARCs models (Gustafsson et al. 2008) that were specifically generated for the APOGEE-N survey (see Mészáros et al. 2012;

⁵ See https://www.sdss.org/dr17/irspec/spectro_data/ to access the data for individual systems.

⁶ See https://data.sdss.org/datamodel/files/APOGEE_REDUX/APRED_VERS/visit/TELESCOPE/FIELD/PLATE_ID/MJD5/apVisit.html for more information.

⁴ Data is publicly available on <http://roboaokepler.com/>

Zamora et al. 2015; Holtzman et al. 2018). The best-matching synthetic spectrum with the largest cross-correlation value was used to derive the reported radial velocities. The values for the best-fitting spectra are reported in Table 4. The uncertainties for each observation were calculated by following the maximum-likelihood approach presented by Zucker (2003). The median RV precision of our sample with APOGEE-N is 262 m s^{-1} . The derived RVs, the 1σ uncertainties, and the S/N per pixel are presented in Table 5.

3.4. High-resolution Doppler spectroscopy with SOPHIE

KOI-129, KOI-219, KOI-415, KOI-466, KOI-855, and KOI-1288 were observed with the SOPHIE spectrograph as part of observations of the *Kepler* field (Ehrenreich et al. 2011). SOPHIE is a cross-dispersed, environmentally stabilized echelle spectrograph covering the wavelength region of $3872 - 6943 \text{ \AA}$ that is located on the 1.93m telescope at the Observatoire de Haute Provence (Bouchy et al. 2009; Perruchot et al. 2008). The observations for these targets were acquired between 2013 June and 2018 September and were obtained using an exposure time of 1800s in high-efficiency mode, which provides a resolution of $R \sim 40,000$. The high-efficiency mode collects 2.5 times more light than high-resolution mode.

Briefly, the SOPHIE pipeline (Bouchy et al. 2009) performs bias subtraction, optimal extraction using the Horne algorithm (Horne 1986), cosmic-ray rejection, spectral flat-field correction, and wavelength-calibration. The wavelength-calibrated spectra are cross-correlated with a grid of numerical binary masks for various spectral types (F0, G2, K0, K5, M4) consisting of 1 and 0 value-zones, where

the non-zero regions correspond to the theoretical positions and widths of the stellar absorption lines at zero velocity (see further discussion in Baranne et al. 1996; Pepe et al. 2002). The reported RV is the minimum of the cross-correlation function and is determined by fitting a Gaussian function. The corresponding uncertainties are derived semi-empirically using the cross-correlation function and account for photon noise, uncertainties in the wavelength calibration, and systematic instrumental error. The RVs for KOI-415 were obtained from Moutou et al. (2013) while all other RVs were retrieved using the SOPHIE archive⁷. The median RV precision of our sample with SOPHIE is 31 m s^{-1} . The derived RVs, the 1σ uncertainties, and the S/N per pixel at 555nm (order index 26) are presented in Table 5.

3.5. High-resolution Doppler spectroscopy with HPF

KOI-631 was observed with the HPF spectrograph between 2019 March 3 and 2019 July 17. HPF is a high-resolution ($R \sim 55,000$), fiber-fed (Kanodia et al. 2018), temperature controlled (Stefánsson et al. 2016), near-infrared ($\lambda \sim 8080 - 12780 \text{ \AA}$) spectrograph located on the 10m Hobby-Eberly Telescope (HET; Ramsey et al. 1998; Hill et al. 2021) at McDonald Observatory in Texas. Observations are executed in a queue by the HET resident astronomers (Shetrone et al. 2007).

We used the HxRGproc tool⁸ (Ninan et al. 2018) to process the data and perform bias noise removal, nonlinearity correction, cosmic-ray correction, and slope/flux and variance image calculation. The one-dimensional spectra were extracted following the procedures in Ninan et al. (2018), Kaplan et al. (2019), and Metcalf et al. (2019). The wavelength solu-

⁷ <http://atlas.obs-hp.fr/sophie/>

⁸ <https://github.com/indiajoe/HxRGproc>

Table 4. MARCS template parameters used to derive APOGEE-N RVs.

APOGEE ID	KIC ID	KOI ID	T_e	$\log g_*$	[Fe/H]	$v \sin i_*$ ^a
			(K)	(dex)	(dex)	(km s ⁻¹)
2M18523991+4524110	9071386	23	6250	4.5	0.25	17
2M19395458+3840421	3558981	52	5250	4.5	0.25	18
2M19480226+5022203	11974540	129	6250	4.5	-0.25	23
2M19492647+4025473	5297298	130	6000	4.5	0.0	0
2M19424111+4035566	5376836	182	5750	4.5	0.0	22
2M19485138+4139505	6305192	219	5750	4.5	0.0	8
2M19223275+3842276	3642741	242	5750	4.5	0.25	6
2M19073111+3922421	4247092	403	6000	4.5	0.0	11
2M19331345+4136229	6289650	415	5750	4.5	0.0	5
2M19043647+4519572	9008220	466	5750	4.5	0.0	0
2M19214782+3951172	4742414	631	5500	4.5	0.25	0
2M19371604+5004488	11818800	777	5250	4.0	-0.5	13
2M19473316+4123459	6061119	846	5750	4.5	0.0	8
2M19270249+4156386	6522242	855	5000	4.5	-0.5	0
2M19001520+4410043	8218274	1064	6500	4.5	-0.25	46
2M18535277+4503088	8801343	1247	6000	4.5	-0.25	37
2M19160484+4807113	10790387	1288	6200	5.0	0.25	0
2M19320489+4230318	7037540	1347	6000	4.5	-0.25	7
2M19282877+4255540	7363829	1356	5750	4.5	0.25	5
2M19460177+4927262	11517719	1416	5750	4.5	-0.5	36
2M19191325+4629301	9705459	1448	5250	4.0	0.0	21
2M19344052+4622453	9653622	2513	5750	4.5	-0.25	9
2M19254244+4209507	6690171	3320	5000	4.0	0.0	6
2M19273337+3921423	4263529	3358	5250	4.5	0.0	7
2M19520793+3952594	4773392	4367	6250	5.0	0.0	5
2M19543478+4217089	6805414	5329	6000	4.5	0.0	11
2M19480000+4117241	5979863	6018	5500	4.5	-0.25	1
2M19352118+4207199	6698670	6760	5500	4.5	0.0	7

The step sizes for T_e , $\log g_*$, and [Fe/H] are from the APOGEE-N MARCS library grid ($\Delta T_e = 250$ K, $\Delta \log g_* = 0.5$ dex, $\Delta[\text{Fe}/\text{H}] = 0.25$ dex) while search adopts $\Delta v \sin i_* = 1$ km s⁻¹. We note these are nominal values that are the best fit to the highest S/N observation and not to the co-added template used by ASPCAP to derive calibrated spectroscopic parameters.

^aWe caution that values of $v \sin i_* \lesssim 8$ km s⁻¹ are below the APOGEE-N resolution limit (Gilhool et al. 2018).

tion and drift correction were extrapolated using laser frequency comb (LFC) frames obtained from routine calibrations (see Appendix A in Stefánsson et al. 2020). The HPF RVs and the uncertainties were derived analogously to the APOGEE-N RVs albeit using the synthetic spectra from the PHOENIX-generated library by Husser et al. (2013). We performed the (i) telluric correction using the TERRASPEC code (see Bender et al. 2012; Lock-

wood et al. 2014) and (ii) barycentric correction using barycorrpy (Kanodia & Wright 2018), a Python implementation of the algorithms from Wright & Eastman (2014). The median RV precision of our sample with SOPHIE is 31 m s⁻¹. The derived RVs, the 1σ uncertainties, and the S/N per pixel are presented in Table 5.

4. SED, PHOTOMETRIC, AND RV MODELING

Table 5. RVs of the KOI systems listed in Table 2.

BJD _{TDB}	RV	σ	S/N ^a	Instrument
	(m s ⁻¹)	(m s ⁻¹)		
KOI-23:				
2457879.87238	-58634	159	74	APOGEE-N
2457908.78365	-71305	199	53	APOGEE-N
2457918.77059	-70905	148	75	APOGEE-N
2457919.78831	-50636	173	60	APOGEE-N
2457920.79793	-37443	133	105	APOGEE-N
2457938.76514	-46787	181	51	APOGEE-N
2457940.71654	-54188	173	59	APOGEE-N
2457941.71519	-72086	163	78	APOGEE-N
2458007.74254	-72976	142	73	APOGEE-N
2458188.01380	-38493	179	48	APOGEE-N
2458209.98654	-67836	214	39	APOGEE-N
2458234.98148	-37938	157	62	APOGEE-N
2458237.92302	-70895	143	78	APOGEE-N
2458238.91768	-50766	157	74	APOGEE-N
2458261.83229	-64566	200	48	APOGEE-N
2458290.77684	-45956	149	74	APOGEE-N
2458385.59155	-38125	144	84	APOGEE-N
2458562.98452	-46216	134	74	APOGEE-N
				⋮
KOI-6760:				
2456557.73352	-41353	120	72	APOGEE-N
2456559.72345	-23038	112	77	APOGEE-N
2456560.72118	-19307	116	77	APOGEE-N
2456584.63236	-38816	110	76	APOGEE-N
2456585.63086	-46714	118	74	APOGEE-N
2456757.89303	-40635	124	63	APOGEE-N
2456758.90238	-47634	512	13	APOGEE-N
2456760.90580	-52692	142	54	APOGEE-N
2456761.87290	-50127	385	16	APOGEE-N
2456762.86869	-44404	129	59	APOGEE-N
2456763.88121	-35845	134	52	APOGEE-N
2456783.83569	-48448	156	36	APOGEE-N
2456784.82203	-42122	143	44	APOGEE-N
2456785.82551	-32454	132	59	APOGEE-N
2456786.79852	-23422	139	52	APOGEE-N
2456787.80942	-19312	122	59	APOGEE-N
2456788.84316	-25087	183	25	APOGEE-N
2456812.74627	-46955	135	52	APOGEE-N
2456814.75554	-52803	128	54	APOGEE-N
2456815.78559	-50712	118	67	APOGEE-N
2456816.76635	-45836	212	26	APOGEE-N
2456817.76205	-37487	128	56	APOGEE-N
2456818.76465	-27841	123	59	APOGEE-N
2456819.76229	-20577	107	56	APOGEE-N
2456820.75608	-21332	108	67	APOGEE-N

NOTE—This table is published in its entirety in the machine-readable format. A portion is shown here for guidance regarding its form and content.

^aAll S/N estimates are per pixel. The APOGEE-N, SOPHIE, and HPF S/N are the median values per 1D extracted pixel at 1600nm (“green” chip), 555nm (order index 26), and 1070nm (order index 18) with resolution elements of ~ 2 pixels, ~ 5 pixels, and ~ 3 pixels, respectively.

We employ the EXOFASTv2 analysis package (Eastman et al. 2019) to jointly model the photometry, RVs, and the spectral energy density. The SED model uses the precomputed bolometric corrections⁹ from the MIST model grids (Dotter 2016; Choi et al. 2016). EXOFASTv2 models the RVs with a standard Keplerian curve in which the eccentricity and argument of periastron are modeled as $\sqrt{e} \sin \omega_*$ and $\sqrt{e} \cos \omega_*$. The light curves are modeled following the formalism from Mandel & Agol (2002) with a quadratic limb-darkening law. For the long-cadence *Kepler* photometry, we use the `longcadence` option to supersample the light curve model to the average of 10 samples over a duration of 29.425 minutes centered on the input time. The photometric model for targets with an occultation includes an additional component in the form of a thermal emission parameter and assumes uniform limb darkening for the occultation. EXOFASTv2 accounts for light travel time in the models but ignores any relativistic effects. We use the default convergence criteria described in Eastman et al. (2019) for all systems.

The SED fit for each target used Gaussian priors on the (i) broadband photometry listed in Table 6, (ii) host star spectroscopic parameters from the APOGEE Stellar Parameter and Chemical Abundances Pipeline (ASPCAP; García Pérez et al. 2016), (iii) maximum visual extinction from estimates of Galactic dust extinction (Green et al. 2018), and (iv) distance estimates from Bailer-Jones et al. (2018). The spectroscopic parameters from ASPCAP are derived using the combined visit APOGEE-N spectrum, empirically calibrated, and determined to be reliable (see Wilson et al. 2018; Jönsson et al. 2020; Wilson et al. 2022). The uncertainties for all calibrated spectro-

scopic parameters (`TEFF_ERR`, `LOGG_ERR`, and `FE_H_ERR` in the DR17 `allStar` file) are underestimated for our targets because the systematic errors (e.g., due to imperfect LSF-matching, synthetic model atmospheres, synthetic spectra, etc.) may be larger than the statistical errors (see discussions in García Pérez et al. 2016; Holtzman et al. 2015, 2018). We employ the equations in Section 5.4 of Jönsson et al. (2020) to estimate more reliable uncertainties for these spectroscopic parameters.

We note that our models ignore the impact of ellipsoidal variations, reflected light, and star spots. These effects are presumed to be removed in the reduction of *Kepler* photometry, which relies on a Gaussian process model to remove spot-induced photometric variability and does not incorporate a star spot model nor account for contamination from persistent spots or faculae that may be present in all transits (e.g., Irwin et al. 2011; McCullough et al. 2014; Rackham et al. 2017, 2018). The effect is most significant for active M dwarfs but for Sun-like stars it can produce contamination of tens of ppm (Rackham et al. 2019) and for fairly active stars with evolving photometric variability (such as KOI-1416), the rotation signal can produce significant transit depth modulations (e.g., Croll et al. 2015; Pan et al. 2020). The SED fit treats these systems as single-star systems even in the WISE bands and although these are single-lined binaries in the APOGEE-N *H*-band spectra, some contamination may occur in the infrared. The SED fit also relies on theoretical model grids for the SED analysis which provide another source of systematic uncertainty (e.g., Serenelli et al. 2021; Dieterich et al. 2021) and, together with the simple treatment of photometric variability, may be a source of systematic uncertainties that are comparable to the quoted statistical uncertainties.

The derived stellar parameters are listed in Table 7, the model system parameters are listed

⁹ http://waps.cfa.harvard.edu/MIST/model_grids.html#bolometric

in Table 8¹⁰, and the derived physical parameters are listed in Table 9. Two examples of the model fit for the brown dwarf KOI-1288.01 and the M dwarf KOI-1416.01 are shown in Figures 2a and 2b, respectively.

5. COMPARISON TO THEORETICAL MODELS

The derived masses (M_2) and radii (R_2) of the 28 KOI companions are displayed in Figure 3 along with the published set of masses and radii (compiled from Parsons et al. 2018; Chaturvedi et al. 2018; Carmichael et al. 2020; Grieves et al. 2021; Acton et al. 2021; van Roestel et al. 2021; Cañas et al. 2022) for objects spanning 10 – 300 M_J ($\sim 0.10 - 0.29 M_\odot$). We compare the measured masses and radii to the values predicted using evolution tracks from Marley et al. (2021) (Sonora21), Phillips et al. (2020) (ATMO20), Baraffe et al. (1998) (BCAH98) and Baraffe et al. (2015) (BHAC15). All evolutionary models are calculated for solar metallicity ($[M/H] = 0$) except the BCAH98 models which are calculated for metal-poor stars ($[M/H] = -0.5$).

There are four systems (KOI-403, KOI-2513, KOI-3358, KOI-4367) where the radius is poorly constrained ($\sigma_{R_2} > 1 R_J$) due to the grazing nature of the transits. Of the 24 remaining systems, all but four are larger than evolutionary tracks of comparable age would suggest. Figures 3(b) and 3(c) display the 24 non-grazing substellar and very-low mass (10 – 110 M_J) and M dwarf ($> 140 M_J$) companions, respectively, colored to the median age derived from the SED fit.

For the sample of APOGEE-N KOIs, the disagreement between predicted and observed radii is within 2σ of the measured radius. Regardless of the choice of evolutionary model (Sonora21,

ATMO20, BCAH98, BHAC15), almost all non-grazing KOIs systems are discrepant by 9.1% when compared to a track of comparable age. The M dwarf companions to KOI-846, KOI-1416, and KOI-1247 are inflated by more than $\sim 10\%$ compared to the other M dwarfs in Figure 3(c) and have $R_2 > 2.3 R_J$. KOI-1247 is tidally locked and the light curve reveals ellipsoidal variations while KOI-1416 is almost tidally locked, such that tidal interactions with the respective host stars may be the source for inflation. Our photometric model ignores the effects of ellipsoidal variability such that the reported radii may be biased and underestimate the formal uncertainties. The *Kepler* photometry for KOI-846 reveals a short rotation period (see Appendix B) < 3 days, which is smaller than the average rotation period of $\gtrsim 4$ days for a G0/F8 dwarf seen in the *Kepler* sample (e.g., Nielsen et al. 2013; McQuillan et al. 2014). The rapid rotation period is in agreement with the young age derived from the SED, suggesting that the companion may be a young, rapidly rotating, active M dwarf which are thought to be inflated due to magnetic activity (Morales et al. 2008; Jackson et al. 2018). The amount of inflation for all other non-grazing systems is smaller than KOI-1247, KOI-1416, and KOI-846 but persists regardless of orbital period (see Figure 4) such that tidal interactions cannot account for the inflation seen in the sample. Two systems, KOI-52 and KOI-5329, are $\sim 7\%$ smaller than predicted but do not have any indication (e.g., a high RUWE, RV trend, or companions detected with Robo-AO) that an unresolved stellar companion could exist and be a source of dilution. The median offset of the APOGEE-N KOIs is 0.13 R_J (9.1%) and does not correlate with orbital period or stellar age (see Figure 4).

The inflation regardless of age or tidal interactions is in agreement with the observed discrepancy in measurements from detached eclipsing

¹⁰ Our fits use the $\sqrt{e} \sin \omega_*$ and $\sqrt{e} \cos \omega_*$ parameterization; e and ω_* are not direct model parameters but derived values

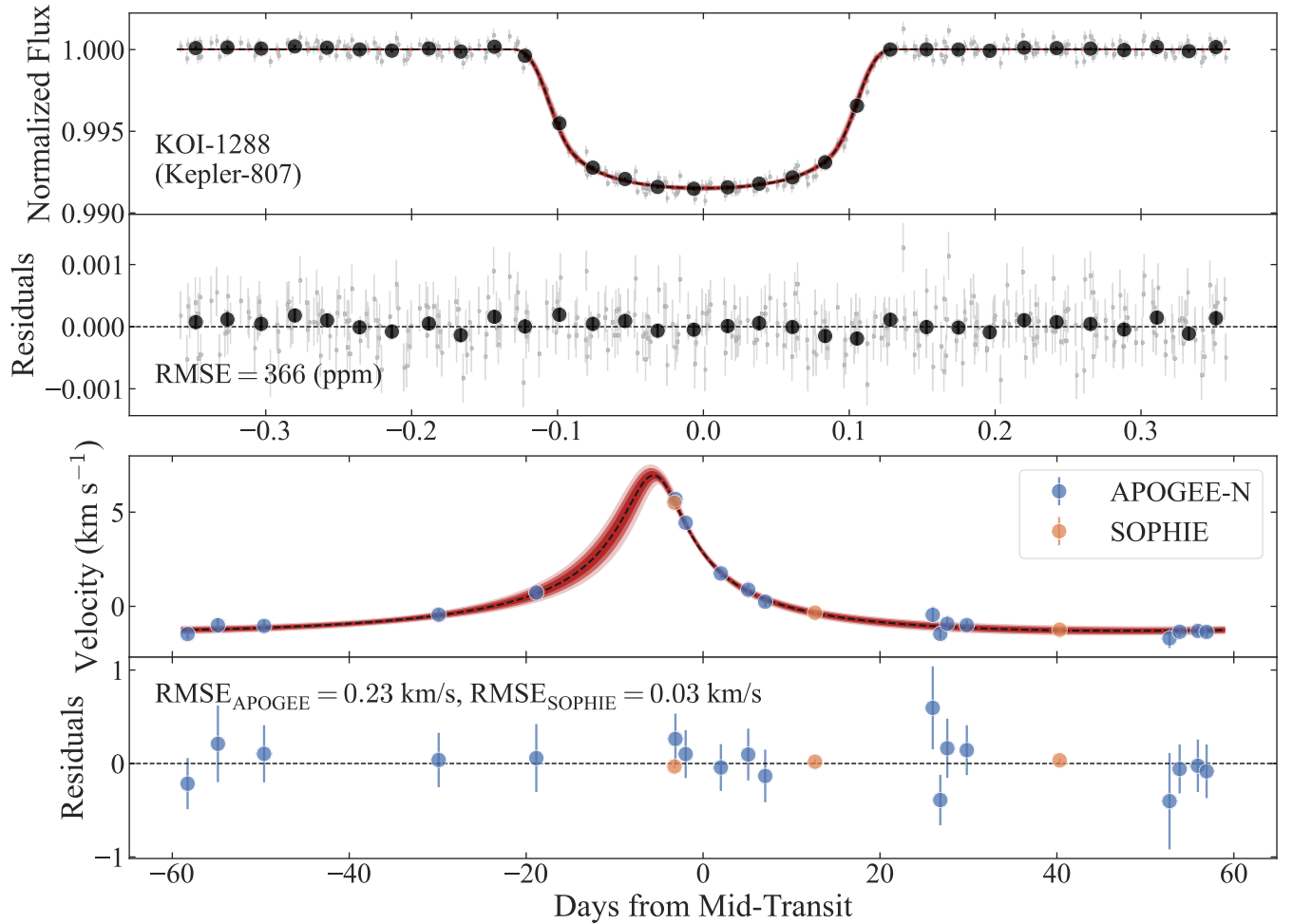


Figure 2a. Top. The *Kepler* photometry for KOI-1288 after phase-folding to the derived ephemeris. The large circles represent 30 min bins of the raw photometry. **Bottom.** The RVs after removing instrumental offsets and phase-folding the data to the derived ephemeris. In each panel, the 1σ (darkest), 2σ , and 3σ (brightest) extent of the models are shown for reference. The complete figure set for the KOIs (28 images) is available in the online journal.

M dwarf binaries. [Parsons et al. \(2018\)](#) used a sample of detached eclipsing M dwarf binaries to demonstrate that the mass-radius relationship for M dwarfs contained a lot of “scatter” relative to theoretical predictions from evolutionary models by [Baraffe et al. \(2003\)](#) and [Baraffe et al. \(2015\)](#). This discrepancy between theoretical models and measured values was first observed with high-precision data for low-mass eclipsing binaries (e.g., [Torres & Ribas 2002](#); [Ribas 2003](#); [López-Morales & Ribas 2005](#); [Morales et al. 2009](#)) where the measured radii were seen to exceed the predictions at fixed masses from evolutionary models by 5–10%. Additional mass and

radius measurements of eclipsing M dwarf binaries (e.g., [Kraus et al. 2011](#); [Birkby et al. 2012](#)) and fully convective M dwarfs with measured rotation periods ([Kesseli et al. 2018](#)) similarly reported a radius inflation of 10–15% relative to theoretical models that could not be ascribed to binarity or age.

For the subset of short-period binary systems, tidal interactions with the host star are thought to be the source of the inconsistency with stellar models. Tidal interactions with a close stellar companion may enhance stellar activity due to magnetic locking, disk disruption, tidal effects, or angular momentum exchange ([López-](#)

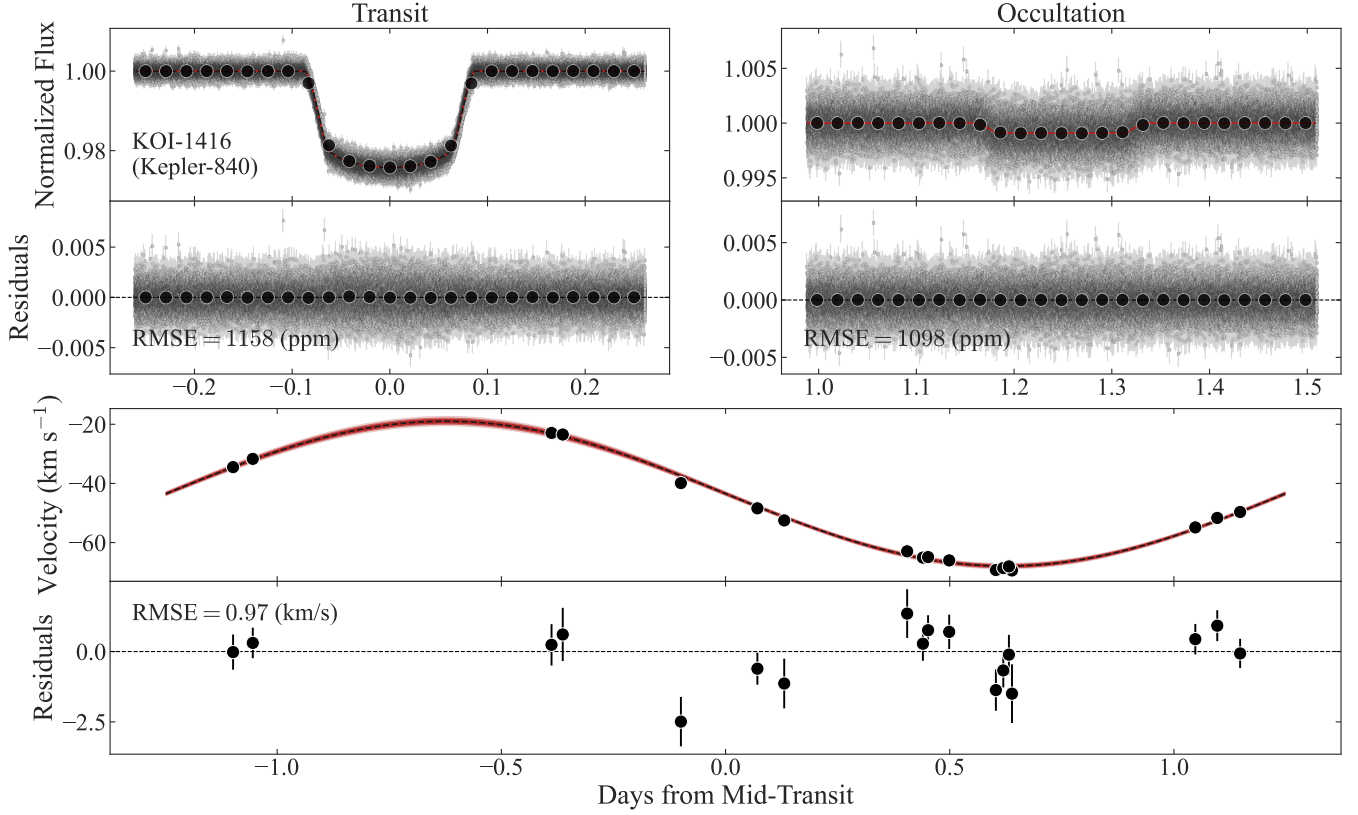


Figure 2b. Figure 2 (cont.). **Top.** The *Kepler* photometry for KOI-1416 centered on the transit and occultation after phase-folding to the derived ephemeris. The large circles represent 30 min bins of the raw data. **Bottom.** The APOGEE-N RVs after phase-folding the data to the derived ephemeris. In each panel, the 1σ (darkest), 2σ , and 3σ (brightest) extent of the models are shown for reference. The complete figure set for the KOIs (28 images) is available in the online journal.

Morales 2007; Chabrier et al. 2007; Morgan et al. 2012; Stassun et al. 2012), which could increase star-spot coverage and/or increase the magnetic field strength. Strong magnetic fields could inhibit convective heat transport (e.g., Chabrier et al. 2007; Strassmeier 2009; Feiden & Chaboyer 2013; Feiden 2016), provide magnetic pressure support (e.g., MacDonald & Mullan 2017), or result in dark magnetic spots (e.g., Spruit 1992; Chabrier et al. 2007; Morales et al. 2010; Somers & Pinsonneault 2015) which could serve to increase the stellar radius. Most of the KOIs analyzed in this work are well-separated ($a/R_1 > 10$) from their host stars (see Figure 4) and are not tidally locked (see Appendix B), such that enhanced magnetic activity induced due to binarity cannot explain the inflation.

The stellar companions ($M_2 \gtrsim 80M_J$) to the KOIs in this work are mid- to late-M dwarfs and observations of such low-mass stars (e.g., West et al. 2015; Newton et al. 2017) have shown this population can be magnetically active. In this low-mass regime, the inflation has also been shown to correlate with metrics of stellar and magnetic activity (e.g., Stassun et al. 2012). The scatter on the mass-radius diagram for these 28 KOI companions is comparable to previous work on M dwarf eclipsing binaries (e.g., Parsons et al. 2018; Chaturvedi et al. 2018) and may be endemic to low-mass stars due to their intrinsic stellar activity.

6. DISCUSSION

6.1. Detailing the five brown dwarfs observed

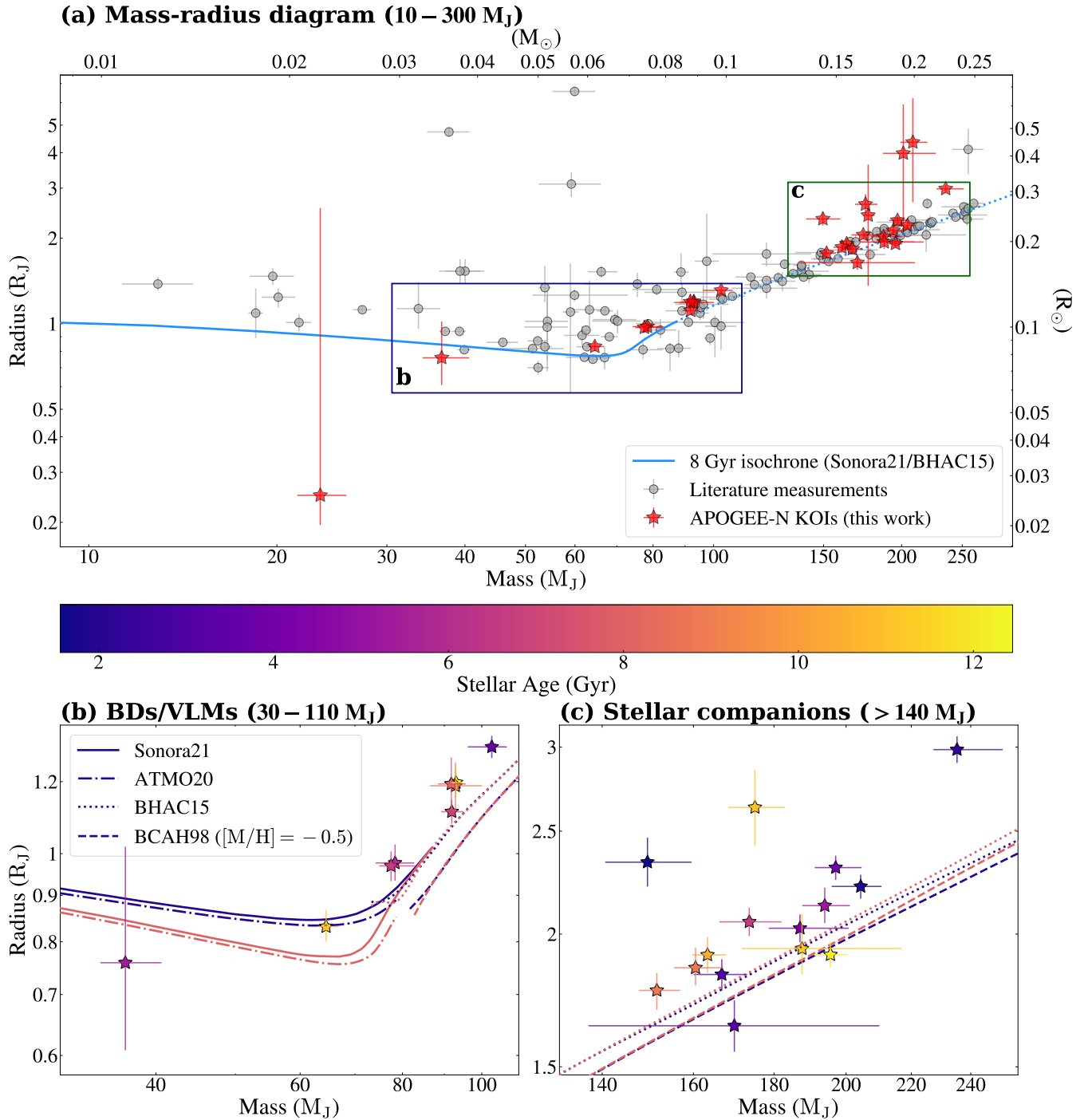


Figure 3. (a). The mass-radius diagram spanning the regime of substellar companions and convective M dwarfs. The KOIs characterized in this work are shown as red stars while the published objects are grey circles. A nominal isochrone of 8 Gyrs (the median SED age for the 28 KOIs) is plotted for reference. 24 objects are non-grazing and have larger radii than theoretical models predict. The regions shown in panels (b) and (c) are marked with rectangles. (b). The mass-radius diagram for the nine non-grazing KOI companions spanning $30 M_J < M_2 < 110 M_J$. (c) The mass-radius diagram for the 15 non-grazing KOI companions spanning $140 M_J < M_2 < 250 M_J$. The objects in panels (b) and (c) are colored based on the age estimated from the SED fit. Evolutionary tracks for 2 and 8 Gyrs from models by Marley et al. (2021) (Sonora21), Phillips et al. (2020) (ATMO20), Baraffe et al. (1998) (BCAH98), and Baraffe et al. (2015) (BHAC15) are plotted for reference and use the same color scale as the stars.

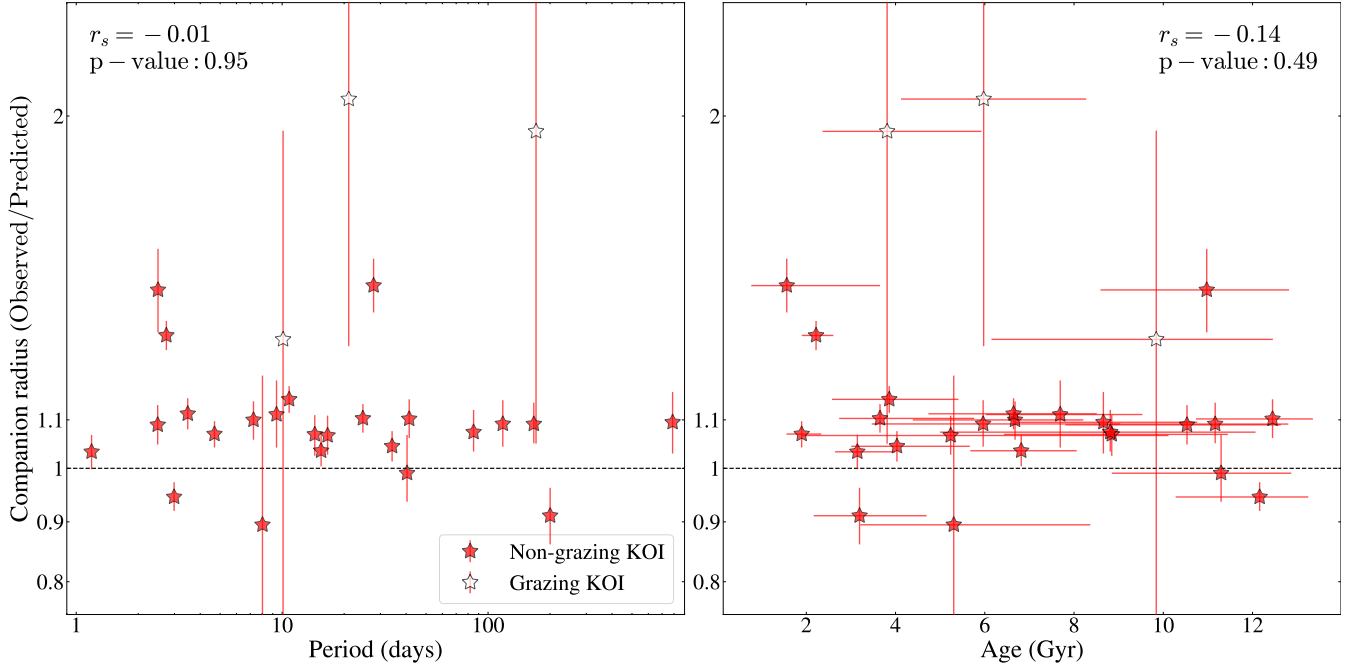


Figure 4. The ratio between the measured radius and the predicted radius from the evolutionary models of Baraffe et al. (2015) and Marley et al. (2021) as a function of the period (left panel) and stellar age (right panel). In each panel, non-grazing KOIs are plotted as red stars while grazing KOIs are shown as white stars. For clarity, KOI-2513 is not shown on this plot because of the large uncertainty on radius. Each system is compared to the prediction from evolutionary models at the median age determined from the SED fit. The Spearman correlation (r_s) and associated p-value are listed for each panel. On average, the observed radii are 9.1% larger than the predicted radii.

The sample of 28 KOI systems includes 5 brown dwarf companions: KOI-2513, KOI-219, KOI-415, KOI-242, and KOI-1288. Two of these, KOI-415 (Moutou et al. 2013) and KOI-242 (Cañas et al. 2018), were previously published but are included in this work to provide updated system parameters. The other three objects are newly discovered substellar companions orbiting early G or late F dwarfs. These objects are described in greater detail below.

- **KOI-2513** is a faint ($V = 14.99$, $H = 13.45$), metal-poor ($[\text{Fe}/\text{H}] = -0.37 \pm 0.02$) G dwarf with a grazing companion on a 19-day orbit detected by *Kepler*. While the grazing nature precludes a precise measurement of the radius, it does allow us to constrain the mass. The Keplerian fit to the APOGEE-N RVs indicate the transiting companion is a low-

mass brown dwarf with $M_2 = 23_{-2}^{+3} M_J$ on a slightly eccentric orbit ($e = 0.38 \pm 0.04$). No bright ($\Delta\text{mag} < 3$) companions are detected within $4''$ using Robo-AO. The distance is poorly constrained by Gaia and the RUWE is similarly large. Future releases from Gaia will improve these measurements to determine if there may be an unresolved, faint ($\Delta\text{mag} > 3$) companion nearby (e.g., Belokurov et al. 2020).

- **KOI-219 (Kepler-494)** is a faint ($V = 14.39$, $H = 12.54$), metal-rich ($[\text{Fe}/\text{H}] = 0.016 \pm 0.02$) G dwarf with a transiting companion on an 8-day orbit detected by *Kepler*. This object was statistically validated by Morton et al. (2016) and given the designation Kepler-494 b. The Keplerian fit to the APOGEE-N

RVs indicate the transiting companion is an intermediate-mass brown dwarf with $M_2 = 37_{-2}^{+4} M_J$ on a slightly eccentric orbit ($e = 0.26 \pm 0.02$). No bright ($\Delta\text{mag} < 4$) companions are detected within $4''$ using Robo-AO. Like KOI-2513, the distance is poorly constrained by Gaia and the RUWE is similarly large and future releases from Gaia will improve these measurements.

- **KOI-415** is a faint ($V = 14.34$, $H = 12.67$), metal-poor ($[\text{Fe}/\text{H}] = -0.24 \pm 0.02$), slightly evolved G dwarf with a transiting companion on a 167-day orbit detected by *Kepler*. This object was initially published as a brown dwarf by Moutou et al. (2013) using SOPHIE data. We update the orbit and physical parameters using a joint fit with *Kepler*, APOGEE-N, and SOPHIE. KOI-415.01 has a mass of $M_2 = 65_{-1}^{+2} M_J$, a radius of $R_2 = 0.83_{-0.03}^{+0.04} R_J$, and is on a very eccentric orbit ($e = 0.701 \pm 0.002$). No bright ($\Delta\text{mag} < 4$) companions are detected within $4''$ using Robo-AO.
- **KOI-1288 (Kepler-807)** is a faint ($V = 15.30$, $H = 13.77$), solar metallicity ($[\text{Fe}/\text{H}] = 0.04 \pm 0.02$) late F dwarf with a transiting companion on a 118-day orbit detected by *Kepler*. This object was statistically validated by Morton et al. (2016) and given the designation Kepler-807 b. The Keplerian fit to the APOGEE-N RVs indicate the transiting companion is near the hydrogen-burning mass limit and is either a high-mass brown dwarf or a very low-mass star with $M_2 = 78 \pm 4 M_J$ on a very eccentric orbit ($e = 0.69 \pm 0.01$). No bright ($\Delta\text{mag} < 3$) companions are detected within $4''$ using Robo-AO.
- **KOI-242** is a faint ($V = 15.01$, $H = 13.14$), metal-rich ($[\text{Fe}/\text{H}] = 0.26 \pm 0.01$),

slightly evolved G dwarf with a transiting companion on a 7.25-day orbit detected by *Kepler*. This object was initially published as an object near the hydrogen-burning mass limit by Cañas et al. (2018) using APOGEE-N data (from DR14). We update the orbit and physical parameters using a joint fit with *Kepler* and the complete set of APOGEE-N RVs. KOI-242.01 has a mass of $M_2 = 77_{-3}^{+5} M_J$, a radius of $R_2 = 0.97 \pm 0.04 R_J$, and is on a circular orbit ($e = 0.007_{-0.005}^{+0.008}$). No bright ($\Delta\text{mag} < 3$) companions are detected within $4''$ using Robo-AO.

None of the aforementioned objects show secondary light in the APOGEE-N spectra. The host stars of these objects are evolving off the main sequence with KOI-242 being the only object formally on the subgiant branch. KOI-242.01 is the only brown dwarf in our sample found to have a circular orbit and this may be due to the subgiant nature of its host star ($a/R_\star < 10$).

6.2. Tidal evolution in low-mass binaries

A comparison of the KOI sample on the period-eccentricity diagram (see Figure 5) with published substellar and M dwarf companions shows that the overall population is consistent with the circularization period of ~ 10 days for nearby field binaries orbiting Sun-like stars (e.g., Duquennoy & Mayor 1991; Meibom & Mathieu 2005; Raghavan et al. 2010). We compare the sample of KOIs with the maximum eccentricity a system unaffected by tides may have (Halbwachs et al. 2005) assuming a circularization period of 10 days. With the exception of the intermediate-mass brown dwarf KOI-219.01, the KOI sample shows the expected circularization for short-period systems caused by tidal forces. The M dwarf companions ($M_2 > 140 M_J$) to the KOIs in our sample adhere to

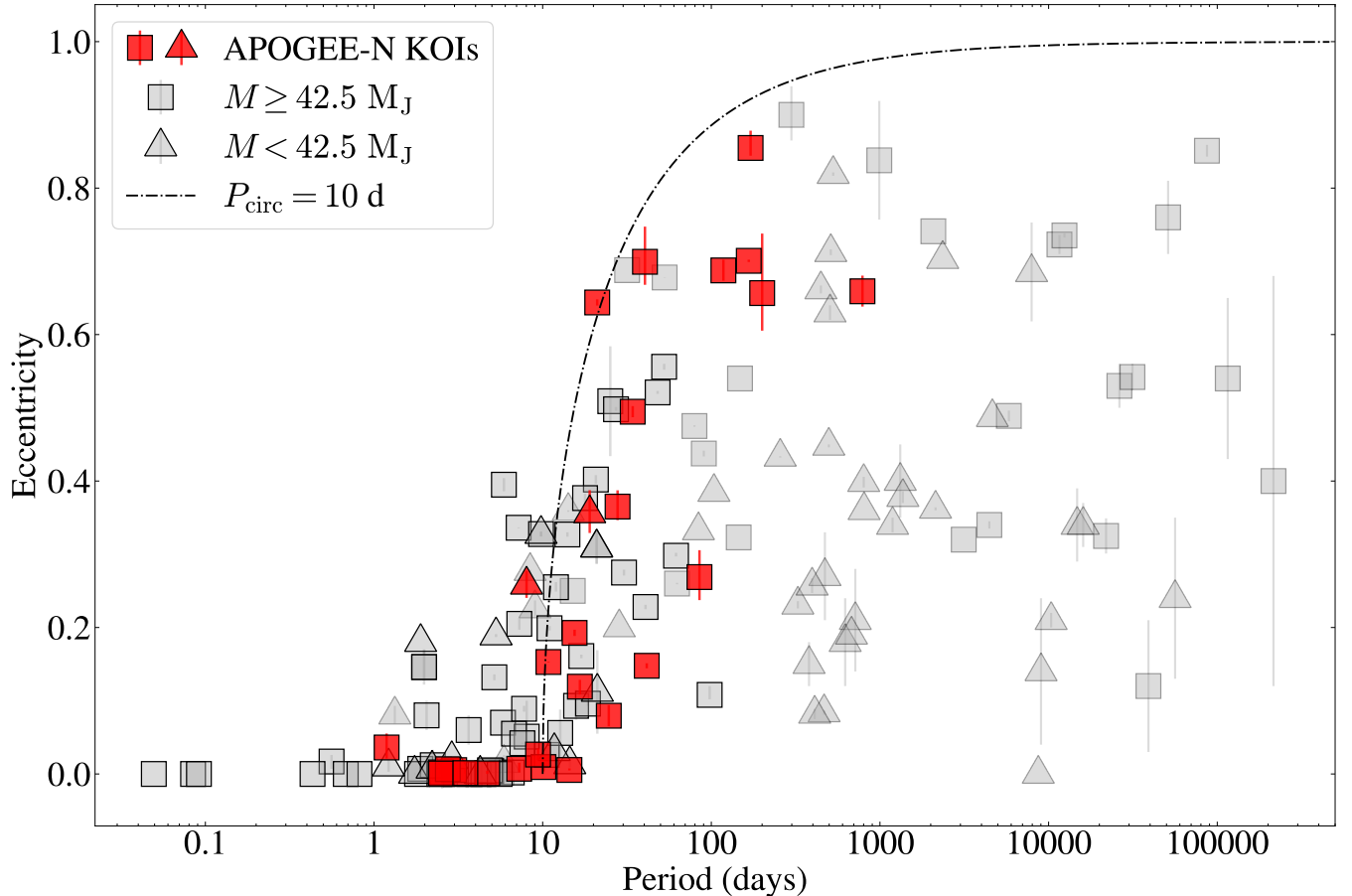


Figure 5. The eccentricity as a function of the period for published brown dwarf-hosting systems. Grey triangles denote the brown dwarfs with $M_2 \sin i < 42.5 M_J$ while grey squares are larger than this mass. The dashed line indicates the maximum eccentricity for systems unaffected by tides when adopting a circularization period (see [Halbwachs et al. 2005](#)) of 10 days. The KOIs are denoted as red squares or triangles, depending on the mass.

the trend that short-period binary systems of comparable age are primarily in circular orbits.

An analysis of the brown dwarf population by ([Ma & Ge 2014](#)) showed different eccentricity distributions for low-mass and high-mass brown dwarfs and postulated the different eccentricity distributions may be a result of different formation mechanisms for two populations. The low-mass regime of brown dwarfs $M < 42.5 M_J$ may form similar to planets and follow the eccentricity distribution of gas giant planets (circularization periods < 5 days; [Halbwachs et al. 2005](#); [Pont et al. 2011](#); [Bonomo et al. 2017](#)) while a high-mass regime of brown dwarfs with $M > 42.5 M_J$ may form like stellar binaries and

adhere to the eccentricity distribution of field binary stars. The short period and high eccentricity of KOI-219 may simply be an imprint of migration and scattering after formation (see [Whitworth et al. 2007](#); [Chabrier et al. 2014](#); [Whitworth 2018](#); [Forgan et al. 2018](#)).

6.3. Low-mass stellar companions masquerading as planets

As part of this survey, we prioritized known planets ([Fleming et al. 2015](#)) to complement other methods of statistical validation (e.g., [Torres et al. 2011](#); [Morton et al. 2016](#)). Seven of the KOI companions (see [Table 2](#)) were previously listed as genuine planet candidates. These systems were statistically validated as part of a

false-positive analysis of thousands of KOIs by Morton et al. (2016) using an algorithm Morton (2012) designed to assess the probability a KOI is a genuine planet by simulating and determining the likelihood of a range of astrophysical false-positive scenarios, including background eclipsing binaries (BEBs), eclipsing binaries (EBs), and hierarchical eclipsing binaries (HEBs). The analysis by Morton et al. (2016) was performed prior to a Gaia data release such that the stellar parameters may have systematically underestimated the radius which is particularly relevant for the *Kepler* field as it is known to contain a significant fraction of mildly evolved stars (Bastien et al. 2014, 2016).

Even with revised stellar parameters from Gaia (e.g., Berger et al. 2020), it is difficult to ascertain whether these systems are inflated Jupiters or genuine substellar and stellar companions. APOGEE-N data serves to eliminate the EB and HEB false positive scenarios while also placing limits on the presence of additional stellar companions. Data from the APOGEE-KOI program has already been used to vet a planetary system and confirm a unique example of a hot Jupiter with an interior super-Earth (e.g., Cañas et al. 2019a) while in this work it serves to confirm the false positive nature of eight systems classified as confirmed planets.

6.4. Gaia metrics of the APOGEE-N KOIs

The re-normalized unit weight error (RUWE) statistic from Gaia EDR3 has been shown to correlate with the existence of an unresolved stellar companion in recent studies of bright ($G < 12$) stellar binaries (e.g., Belokurov et al. 2020; Penoyre et al. 2020; Stassun & Torres 2021). The RUWE, or the square root of the reduced χ^2 statistic that has been corrected for calibration errors, may be sensitive to the photocentric motions of unresolved objects (see Lindgren et al. 2021). Stars with massive companions on orbital periods much shorter than the baseline of Gaia (34 months or 1035 days for

EDR3) may exhibit deviations from a single-star astrometric solution that appears as noise as the primary star orbits the center of mass (e.g., Kervella et al. 2019; Kiefer et al. 2019). A threshold of $\text{RUWE} \gtrsim 1.4$ has been suggested as an indicator of binarity (Stassun & Torres 2021; Kervella et al. 2022).

Most of the KOIs analyzed (24 systems) have a RUWE below the threshold of 1.4, suggesting these systems do not appear discrepant from a single-star astrometric solution. KOI-219, KOI-2513, KOI-1247, and KOI-1416 are the four KOI systems with $\text{RUWE} > 1.4$. These systems have no indication of secondary light in the APOGEE-N spectra and no detection of bright companions from Robo-AO, such that the origin of the large RUWE may either be a spurious measurement due to the faintness of the objects or a system with a close (separations $< 0.5''$), faint ($\Delta\text{mag} > 3$) on-sky stellar companion (see examples in Ziegler et al. 2020, 2021) that is beyond detection using existing data.

In addition to bound companions, an excess RUWE may be caused by deformities between the model point-spread function and the observed image as a result of an unbound, unresolved companion (e.g., Wood et al. 2021), scattered light due to the presence of a circumstellar disk (e.g., Fitton et al. 2022), or stars with significant photometric or color variability (e.g., RR Lyrae, long-period variable sources, young stars; Belokurov et al. 2020; Lindgren 2018). Both KOI-1416 and KOI-1247 have large radii and RUWE excess while also showing significant photometric variability in the *Kepler* photometry. If the RUWE were due to an unresolved stellar companion, the transits would be diluted and the radius anomaly would not be as large when compared to the other KOI systems (e.g., Ciardi et al. 2015; Bouma et al. 2018). It may be that for systems with significant photometric variability, a RUWE excess does not necessitate an unresolved companion.

All of our targets are faint ($12 < G < 16$) and are located at a median distance of 1060 pc such that the astrometric amplitudes caused by the transiting companions are too small to be detected with the precision afforded by EDR3. Predictions for the detection of low-mass companions from the full and extended Gaia mission by [Holl et al. \(2022\)](#) suggest that Gaia will eventually have the precision to detect the presence of substellar companions down to $G \sim 17$. The RVs from the APOGEE-KOI program will be useful to determine the orbit of long-period stellar companions that appear as trends in our program.

6.5. *The synergy of APOGEE with other missions*

A subset of the 28 KOIs observed with APOGEE-N also have observations from other high-resolution spectrographs: six KOIs were observed with SOPHIE and one system with HPF. In either case, the joint fit with APOGEE-N demonstrates that, while APOGEE-N does not have the precision afforded by these instruments, the APOGEE-N RVs are reliable even for faint targets (median of $H = 13$ for the sample observed by SOPHIE) and enable the determination of accurate orbital elements. For KOI-415 and KOI-855, the two systems with the largest number of observations with a high-precision instrument, the orbital elements derived from APOGEE-N and SOPHIE separately are within their respective 1σ uncertainties. While the precision afforded by SOPHIE and HPF RVs can enable tighter constraints on the derived orbital elements, obtaining as many visits for thousands of KOIs with these or similar high-precision spectrographs is unfeasible. The precision, cadence, and baseline afforded by *Kepler* data and the multiplexing capabilities and high-efficiency of APOGEE-N present an opportunity to reliably analyze individual KOI systems and infer precise orbital elements solely from a joint fit with APOGEE-N RVs.

The objects presented in this work represent a small subset of the science enabled by the APOGEE-KOI program. We have shown that observations from the APOGEE-KOI program complement sparse observations of individual systems from high-precision spectroscopic surveys of the *Kepler* field (e.g., [Ehrenreich et al. 2011](#)). Work by [Wilson et al. \(2022\)](#) has analyzed the sample as a population to leverage the abundances derived with ASPCAP and place constraints on the trends evident in the observed *Kepler* planetary population. The APOGEE-KOI program also targeted a large fraction of KOIs designated as false positive in DR25, where the transit depth or the presence of ellipsoidal variations or a deep occultation reveal the stellar nature of the transiting companion. With the number of APOGEE-N RVs, it should be possible to study the population of single-lined and double-lined eclipsing binaries to revisit tidal evolution in the population of Sun-like stars, similar to the work by [Triaid et al. \(2017\)](#).

The subset of double-lined eclipsing binaries observed by APOGEE-N also enables model-independent mass and radii measurements for a large number of systems spanning all spectral types of MKGF dwarfs. In this work, we have ignored the effect of out-of-transit variability in the form of beaming, ellipsoidal variations, and reflection (BEER, [Faigler & Mazeh 2011](#); [Engel et al. 2020](#)) for short-period binaries, but a joint BEER analysis with RVs can facilitate very precise mass measurements of even non-transiting companions (e.g., [Tal-Or et al. 2015](#)).

Beyond the *Kepler* field, APOGEE-N has targeted various K2 ([Howell et al. 2014](#)) campaigns and the Transiting Exoplanet Survey Satellite (TESS; [Ricker et al. 2015](#)) continuous-viewing zones. For many transiting candidates from these missions there may exist a few observations of K2OIs or TOIs where serendipitous APOGEE-N observations can effectively vet a

candidate signal. In the context of TESS, the ongoing search for transits (e.g., Jenkins et al. 2016; Huang et al. 2020a,b) will benefit from the coverage of APOGEE. RVs from APOGEE-N have already been used in tandem with data from other spectrographs to confirm a transiting hot Jupiter (Cañas et al. 2019b) and a transiting substellar companion (Cañas et al. 2022). An extensive list of ancillary science projects beyond planets can be found in Beaton et al. (2021).

7. SUMMARY

In this manuscript we present an analysis of a subset of 28 KOIs observed by the APOGEE-KOI program and characterize these low-mass transiting companions using *Kepler* photometry and RVs from APOGEE-N. We leverage the precision afforded by *Kepler* and APOGEE-N RVs to derive masses and radii for these companions and compare this population to existing observations of brown dwarfs and M dwarfs. We find our sample is slightly inflated (9.1%) relative to the radius predicted from stellar evolutionary models evaluated at the age determined from an SED fit, and this inflation does not correlate with period or stellar age. This inflation is consistent with previous extensive studies of brown dwarfs and eclipsing M dwarf binaries and we hypothesize it may be a result of stellar activity (e.g., strong magnetic fields or dark star spots) in the very low-mass companion. The sample also adheres to the circularization trends seen in field eclipsing binaries. The systems observed in this work represent a small subset of the APOGEE-KOI program and we highlight the utility of APOGEE RVs to complement data from high-precision RV surveys, validation of systems in transiting surveys, and eventually any detections of substellar and low-mass companions from the full Gaia mission.

ACKNOWLEDGMENTS

We thank the anonymous referee for detailed and thoughtful feedback, which has improved the quality of this manuscript. CIC acknowledges support by NASA Headquarters under the NASA Earth and Space Science Fellowship Program through grant 80NSSC18K1114, the Alfred P. Sloan Foundation’s Minority Ph.D. Program through grant G-2016-20166039, the Pennsylvania State University’s Bunton-Waller program, and an appointment to the NASA Postdoctoral Program at the Goddard Space Flight Center, administered by USRA through a contract with NASA. The Center for Exoplanets and Habitable Worlds is supported by the Pennsylvania State University and the Eberly College of Science. The computations for this research were performed on the Pennsylvania State University’s Institute for Computational and Data Sciences’ Roar supercomputer, including the CyberLAMP cluster supported by NSF grant MRI-1626251. This content is solely the responsibility of the authors and does not necessarily represent the views of the Institute for Computational and Data Sciences.

The Pennsylvania State University campuses are located on the original homelands of the Erie, Haudenosaunee (Seneca, Cayuga, Onondaga, Oneida, Mohawk, and Tuscarora), Lenape (Delaware Nation, Delaware Tribe, Stockbridge-Munsee), Shawnee (Absentee, Eastern, and Oklahoma), Susquehannock, and Wahzhazhe (Osage) Nations. As a land grant institution, we acknowledge and honor the traditional caretakers of these lands and strive to understand and model their responsible stewardship. We also acknowledge the longer history of these lands and our place in that history.

We acknowledge support from NSF grants AST 1006676, AST 1126413, AST 1310875, AST 1310885, AST 2009554, AST 2009889, AST 2108512, AST 2108801 and the NASA Astrobiology Institute (NNA09DA76A) in our pursuit of precision RVs in the near-infrared.

We acknowledge support from the Heising-Simons Foundation via grant 2017-0494.

Some of these results are based on observations obtained with HPF on the HET. The HET is a joint project of the University of Texas at Austin, the Pennsylvania State University, Ludwig-Maximilians-Universität München, and Georg-August Universität Göttingen. The HET is named in honor of its principal benefactors, William P. Hobby and Robert E. Eberly. The HET collaboration acknowledges the support and resources from the Texas Advanced Computing Center. We are grateful to the HET Resident Astronomers and Telescope Operators for their valuable assistance in gathering our HPF data. We would like to acknowledge that the HET is built on Indigenous land. Moreover, we would like to acknowledge and pay our respects to the Carrizo & Comecrudo, Coahuiltecan, Caddo, Tonkawa, Comanche, Lipan Apache, Alabama-Coushatta, Kickapoo, Tigua Pueblo, and all the American Indian and Indigenous Peoples and communities who have been or have become a part of these lands and territories in Texas, here on Turtle Island.

Some of the data presented in this paper were obtained from MAST at STScI. The specific observations analyzed can be accessed via DOI: [10.17909/nrwp-q285](https://doi.org/10.17909/nrwp-q285). Support for MAST for non-HST data is provided by the NASA Office of Space Science via grant NNX09AF08G and by other grants and contracts. This work includes data collected by the *Kepler* mission, which are publicly available from MAST. Funding for the *Kepler* mission is provided by the NASA Science Mission directorate. This research made use of the (i) NASA Exoplanet Archive, which is operated by Caltech, under contract with NASA under the Exoplanet Exploration Program, (ii) SIMBAD database, operated at CDS, Strasbourg, France, (iii) NASA's Astrophysics Data System Bibliographic Services, (iv) data from 2MASS, a joint project

of the University of Massachusetts and IPAC at Caltech, funded by NASA and the NSF, and (v) AAVSO Photometric All-Sky Survey (APASS), funded by the Robert Martin Ayers Sciences Fund and NSF AST-1412587. This work used data retrieved from the SOPHIE archive at Observatoire de Haute-Provence, available at <http://atlas.obs-hp.fr/sophie>.

Funding for the SDSS-IV has been provided by the Alfred P. Sloan Foundation, the U.S. Department of Energy Office of Science, and the Participating Institutions. SDSS-IV acknowledges support and resources from the Center for High Performance Computing at the University of Utah. The SDSS website is www.sdss.org. SDSS-IV is managed by the Astrophysical Research Consortium for the Participating Institutions of the SDSS Collaboration including the Brazilian Participation Group, the Carnegie Institution for Science, Carnegie Mellon University, Center for Astrophysics — Harvard & Smithsonian, the Chilean Participation Group, the French Participation Group, Instituto de Astrofísica de Canarias, The Johns Hopkins University, Kavli Institute for the Physics and Mathematics of the Universe (IPMU) / University of Tokyo, the Korean Participation Group, Lawrence Berkeley National Laboratory, Leibniz Institut für Astrophysik Potsdam (AIP), Max-Planck-Institut für Astronomie (MPIA Heidelberg), Max-Planck-Institut für Astrophysik (MPA Garching), Max-Planck-Institut für Extraterrestrische Physik (MPE), National Astronomical Observatories of China, New Mexico State University, New York University, University of Notre Dame, Observatório Nacional / MCTI, The Ohio State University, Pennsylvania State University, Shanghai Astronomical Observatory, United Kingdom Participation Group, Universidad Nacional Autónoma de México, University of Arizona, University of Colorado Boulder, University of Oxford, University of Portsmouth, University

of Utah, University of Virginia, University of Washington, University of Wisconsin, Vanderbilt University, and Yale University.

The Pan-STARRS1 Surveys (PS1) and the PS1 public science archive have been made possible through contributions by the Institute for Astronomy, the University of Hawaii, the Pan-STARRS Project Office, the Max-Planck Society and its participating institutes, the Max Planck Institute for Astronomy, Heidelberg and the Max Planck Institute for Extraterrestrial Physics, Garching, The Johns Hopkins University, Durham University, the University of Edinburgh, the Queen’s University Belfast, the Harvard-Smithsonian Center for Astrophysics, the Las Cumbres Observatory Global Telescope Network Incorporated, the National Central University of Taiwan, the Space Telescope Science Institute, the National Aeronautics and Space Administration under Grant No. NNX08AR22G issued through the Planetary Science Division of the NASA Science Mission Directorate, the National Science Foundation Grant No. AST-1238877, the University of Maryland, Eotvos Lorand University (ELTE), the Los Alamos National Laboratory, and the Gordon and Betty Moore Foundation.

This work has made use of data from the European Space Agency (ESA) mission

Gaia (<https://www.cosmos.esa.int/gaia>), processed by the Gaia Data Processing and Analysis Consortium (DPAC, <https://www.cosmos.esa.int/web/gaia/dpac/consortium>). Funding for the DPAC has been provided by national institutions, in particular the institutions participating in the Gaia Multilateral Agreement.

Facilities: Exoplanet Archive, Gaia, HET (HPF), *Kepler*, KPNO:2.1m (Robo-AO), Sloan (APOGEE-N), MAST, OHP:1.93m (SOPHIE)

Software: `astroquery` (Ginsburg et al. 2019), `astropy` (Astropy Collaboration et al. 2018), `ARC2` (Aigrain et al. 2017), `barycorrpy` (Kanodia & Wright 2018), `dustmaps` (Green 2018), `dynesty` (Speagle 2020), `EXOFASTv2` (Eastman et al. 2019), `HxRGproc` (Ninan et al. 2018), `K2fov` (Mullally et al. 2016a), `juliet` (Espinoza et al. 2019), `matplotlib` (Hunter 2007), `numpy` (van der Walt et al. 2011), `pandas` (McKinney 2010), `scipy` (Virtanen et al. 2020), `terraspec` (Bender et al. 2012)

APPENDIX

A. PHOTOMETRIC DETRENDING

We detrended all *Kepler* photometry before fitting with EXOFASTv2 using a Gaussian process noise model with the approximate quasi-periodic kernel presented in Foreman-Mackey et al. (2017) of the form:

$$k(\tau) = \frac{B}{2+C} e^{-\tau/L} \left[\cos\left(\frac{2\pi\tau}{P_{\text{GP}}}\right) + (1+C) \right], \quad (\text{A1})$$

where τ is the time of observation while B , C , L , and P_{GP} are the hyperparameters of the covariance function. B and C represent the weight of the exponential term with a decay constant of L (in days). P_{GP} determines the periodicity of the quasi-periodic oscillations, which is interpreted as the stellar rotation period. This kernel is able to reproduce the behavior of a more traditional quasi-periodic covariance function and has allowed for computationally efficient inference of stellar rotation periods even for large datasets that are not uniformly sampled (e.g., Angus et al. 2018). For the purposes

Table 2. *Kepler* photometry used for the 28 KOIs.

APOGEE ID	KIC ID	KOI	Designation ^a	<i>Kepler</i> Short Cadence	<i>Kepler</i> Long Cadence
2M18523991+4524110	9071386	23	...	✓	...
2M19395458+3840421	3558981	52	✓
2M19480226+5022203	11974540	129	Kepler-470 b	✓	✓
2M19492647+4025473	5297298	130	...	✓	✓
2M19424111+4035566	5376836	182	...	✓	...
2M19485138+4139505	6305192	219	Kepler-494 b	...	✓
2M19223275+3842276	3642741	242	✓
2M19073111+3922421	4247092	403	✓
2M19331345+4136229	6289650	415	✓
2M19043647+4519572	9008220	466	✓
2M19214782+3951172	4742414	631	Kepler-628 b	✓	✓
2M19371604+5004488	11818800	777	✓
2M19473316+4123459	6061119	846	Kepler-699 b	...	✓
2M19270249+4156386	6522242	855	Kepler-706 b	...	✓
2M19001520+4410043	8218274	1064	✓
2M18535277+4503088	8801343	1247	...	✓	...
2M19160484+4807113	10790387	1288	Kepler-807 b	...	✓
2M19320489+4230318	7037540	1347	✓
2M19282877+4255540	7363829	1356	...	✓	✓
2M19460177+4927262	11517719	1416	Kepler-840 b	✓	...
2M19191325+4629301	9705459	1448	...	✓	...
2M19344052+4622453	9653622	2513	✓
2M19254244+4209507	6690171	3320	✓
2M19273337+3921423	4263529	3358	✓
2M19520793+3952594	4773392	4367	✓
2M19543478+4217089	6805414	5329	✓
2M19480000+4117241	5979863	6018	✓
2M19352118+4207199	6698670	6760	...	✓	...

^aThe *Kepler* designation for targets on the NASA Exoplanet Archive with a disposition of “confirmed planet” as of 2022 June 5.

of detrending, we make no distinction between activity induced variability (e.g., star spots) or phase modulations due to the binary nature of a system (e.g., Doppler boosting, stellar ellipsoidal distortion, reflection).

For each system, we use the parameters from *Kepler* DR25 candidate list (Thompson et al. 2018) to excise a window of ± 1.5 times the transit duration around each transit before fitting the Gaussian process model. We estimate the maximum *a posteriori* parameters for the GP model using the L-BFGS-B non-linear optimization routine implemented in `scipy` (Virtanen et al. 2020). Each quarter of *Kepler* data is processed separately. An example of detrending with a GP is shown in Figure 6.

Table 3. General information of the KOI host stars.

APOGEE ID	KIC ID	KOI	Gaia	RA	Dec
		(DR25)	(DR3)	(HH:MM:SS)	(DD:MM:SS)
2M18523991+4524110	9071386	23	2107001760170220032	18:52:39.91	45:24:10.96
2M19395458+3840421	3558981	52	2052143143639171072	19:39:54.58	38:40:41.87
2M19480226+5022203	11974540	129	2135313669189075968	19:48:02.26	50:22:20.21
2M19492647+4025473	5297298	130	2073737036615242240	19:49:26.46	40:25:47.09
2M19424111+4035566	5376836	182	2076405620054037120	19:42:41.11	40:35:56.81
2M19485138+4139505	6305192	219	2076942628402548608	19:48:51.36	41:39:50.42
2M19223275+3842276	3642741	242	2052853703021795456	19:22:32.75	38:42:27.52
2M19073111+3922421	4247092	403	2100400949491004800	19:07:31.11	39:22:41.98
2M19331345+4136229	6289650	415	2077596288060821120	19:33:13.45	41:36:22.69
2M19043647+4519572	9008220	466	2106436649851315712	19:04:36.47	45:19:57.25
2M19214782+3951172	4742414	631	2101084708287433984	19:21:47.83	39:51:17.28
2M19371604+5004488	11818800	777	2135105075517958144	19:37:16.03	50:04:48.65
2M19473316+4123459	6061119	846	2076838896353601152	19:47:33.15	41:23:45.92
2M19270249+4156386	6522242	855	2101740257736205696	19:27:02.46	41:56:38.68
2M19001520+4410043	8218274	1064	2105945644892917248	19:00:15.21	44:10:04.32
2M18535277+4503088	8801343	1247	2106981148624921344	18:53:52.78	45:03:08.89
2M19160484+4807113	10790387	1288	2130955518633883008	19:16:04.83	48:07:11.21
2M19320489+4230318	7037540	1347	2077796914573293568	19:32:04.88	42:30:31.89
2M19282877+4255540	7363829	1356	2125814958179612544	19:28:28.77	42:55:53.87
2M19460177+4927262	11517719	1416	2134884520357421824	19:46:01.76	49:27:26.02
2M19191325+4629301	9705459	1448	2127712474727909504	19:19:13.24	46:29:30.14
2M19344052+4622453	9653622	2513	2128167225867000576	19:34:40.53	46:22:45.23
2M19254244+4209507	6690171	3320	2101758056080602112	19:25:42.45	42:09:50.59
2M19273337+3921423	4263529	3358	2053170843410198656	19:27:33.41	39:21:42.24
2M19520793+3952594	4773392	4367	2073471985601809152	19:52:07.93	39:52:59.39
2M19543478+4217089	6805414	5329	2075448082868939136	19:54:34.78	42:17:08.89
2M19480000+4117241	5979863	6018	2076790449121125120	19:47:59.99	41:17:24.01
2M19352118+4207199	6698670	6760	2077714932236541440	19:35:21.18	42:07:19.74

Proper motion (RA)	Proper motion (Dec)	Distance ^a	RUWE	Max A_V^b	Robo-AO Detection ^c
(mas yr ⁻¹)	(mas yr ⁻¹)	(pc)	(DR3)	(Green)	
1.79 ± 0.01	4.26 ± 0.01	761 ⁺⁵ ₋₆	0.95	0.19	...
1.44 ± 0.01	-13.50 ± 0.02	474 ± 3	0.92	0.19	...
-1.91 ± 0.01	-9.88 ± 0.01	929 ± 7	1.03	0.25	5.87 mag at 2.1'', L14
-8.98 ± 0.01	-13.99 ± 0.01	940 ± 9	0.97	0.52	None, Z18
2.99 ± 0.02	6.68 ± 0.02	1050 ⁺²⁰ ₋₁₀	1.09	0.39	None, Z18
-3.8 ± 0.3	-6.4 ± 0.4	1800 ⁺¹⁰⁰⁰ ₋₅₀₀	20.74	0.58	None, L14
-3.54 ± 0.02	-3.36 ± 0.02	1550 ⁺⁴⁰ ₋₃₀	0.95	0.38	None, Z17
-2.91 ± 0.02	-11.06 ± 0.02	1070 ± 10	0.94	0.66	None, L14
6.89 ± 0.01	-16.77 ± 0.01	920 ⁺⁹ ₋₁₀	0.98	0.30	None, L14
-5.72 ± 0.02	-3.24 ± 0.02	1640 ⁺⁵⁰ ₋₄₀	0.93	0.19	None, Z17
6.68 ± 0.01	1.33 ± 0.01	870 ⁺⁹ ₋₈	0.92	0.19	None, Z18
-4.47 ± 0.03	-9.07 ± 0.03	2140 ⁺⁹⁰ ₋₈₀	0.94	0.25	None, Z17
-1.27 ± 0.03	-2.59 ± 0.03	1900 ⁺⁹⁰ ₋₈₀	0.99	0.55	None, B16
-16.93 ± 0.03	-0.45 ± 0.03	840 ⁺²⁰ ₋₁₀	1.11	0.22	None, Z17
7.65 ± 0.01	-3.85 ± 0.01	1012 ⁺⁹ ₋₈	1.02	0.20	None, Z18
7.06 ± 0.03	5.44 ± 0.03	624 ⁺⁷ ₋₈	1.71	0.16	None, Z18
-1.89 ± 0.02	-5.65 ± 0.03	1480 ± 50	1.02	0.22	None, L14
-6.30 ± 0.02	5.56 ± 0.02	950 ± 10	1.04	0.22	...
1.80 ± 0.02	-6.08 ± 0.03	1890 ⁺¹⁰⁰ ₋₇₀	0.94	0.27	None, Z17
0.31 ± 0.06	-13.27 ± 0.07	1200 ± 100	4.13	0.36	None, Z18
-0.80 ± 0.03	-0.44 ± 0.03	1210 ⁺⁴⁰ ₋₃₀	1.08	0.25	None, Z18
2.5 ± 0.2	-6.1 ± 0.2	2100 ⁺¹⁰⁰⁰ ₋₅₀₀	9.97	0.44	None, Z17
2.08 ± 0.03	-7.27 ± 0.03	1030 ± 30	0.93	0.27	None, Z17
19.83 ± 0.01	-10.31 ± 0.02	508 ± 3	0.95	0.16	None, Z17
-2.31 ± 0.01	-1.45 ± 0.01	1120 ± 20	0.97	0.36	None, B16
-2.81 ± 0.02	-5.80 ± 0.03	2130 ⁺¹⁰⁰ ₋₉₀	1.03	0.63	None, Z17
-5.45 ± 0.03	-4.89 ± 0.03	1090 ⁺³⁰ ₋₂₀	0.92	0.52	...
2.22 ± 0.02	-11.26 ± 0.02	532 ± 4	1.09	0.22	...

References—B16 (Baranec et al. 2016), DR25 (Thompson et al. 2018), DR3 (Gaia Collaboration et al. 2022), Green (Green et al. 2019), L14 (Law et al. 2014), Z17 (Ziegler et al. 2017), Z18 (Ziegler et al. 2018).

^a The geometric distance from Bailer-Jones et al. (2021).

^b Maximum visual extinction determined from Green et al. (2019).

^c Empty rows are objects not observed as part of the Robo-AO *Kepler* survey. KOI-1356 was observed in a Sloan *i'* filter, all other observations were performed in the LP600 filter.

Table 7. Stellar parameters for the KOI host stars.

APOGEE ID	KIC ID	KOI	T_e^a (K)	[Fe/H] ^a (dex)	log g_* (dex)	M_* (M_\odot)	R_* (R_\odot)	ρ_* (g cm^{-3})	Age (Gyr)	A_V
2M18523991+4524110	9071386	23	6240 ± 80	0.14 ± 0.01	3.99 ^{+0.03} _{-0.04}	1.46 ^{+0.07} _{-0.09}	2.01 ± 0.05	0.25 ± 0.02	2.6 ^{+0.9} _{-0.5}	0.10 ^{+0.05} _{-0.06}
2M19395458+3840421	3558981	52	5090 ± 90	0.08 ± 0.01	4.41 ± 0.02	0.89 ^{+0.03} _{-0.02}	0.97 ± 0.03	1.4 ± 0.1	12 ⁺¹ ₋₂	0.08 ^{+0.07} _{-0.06}
2M19480226+5022203	11974540	129	6300 ± 100	-0.15 ± 0.02	4.08 ^{+0.04} _{-0.05}	1.25 ^{+0.07} _{-0.12}	1.69 ± 0.05	0.36 ± 0.04	3.7 ^{+2.1} _{-0.9}	0.20 ^{+0.04} _{-0.06}
2M19492647+4025473	5297298	130	6100 ± 100	-0.17 ± 0.02	3.99 ^{+0.05} _{-0.04}	1.18 ^{+0.13} _{-0.08}	1.82 ^{+0.06} _{-0.05}	0.28 ^{+0.04} _{-0.03}	5 ± 2	0.33 ^{+0.09} _{-0.1}
2M19424111+4035566	5376836	182	5800 ± 100	0.05 ± 0.01	4.09 ± 0.04	1.06 ^{+0.07} _{-0.06}	1.55 ± 0.05	0.41 ^{+0.05} _{-0.04}	8 ± 2	0.29 ± 0.05
2M19485138+4139505	6305192	219	6000 ± 100	0.16 ± 0.02	4.2 ± 0.2	1.1 ^{+0.2} _{-0.1}	1.4 ^{+0.5} _{-0.3}	0.5 ^{+0.4} _{-0.3}	5 ⁺³ ₋₂	0.50 ^{+0.05} _{-0.06}
2M19223275+3842276	3642741	242	5800 ± 100	0.26 ± 0.01	4.01 ^{+0.05} _{-0.04}	1.17 ^{+0.13} _{-0.06}	1.78 ^{+0.06} _{-0.07}	0.30 ^{+0.04} _{-0.03}	7 ⁺¹ ₋₂	0.36 ^{+0.02} _{-0.03}
2M19073111+3922421	4247092	403	6100 ± 100	-0.01 ± 0.02	4.13 ± 0.04	1.09 ^{+0.09} _{-0.07}	1.50 ^{+0.05} _{-0.04}	0.46 ± 0.05	7 ± 2	0.4 ± 0.1
2M19331345+4136229	6289650	415	5700 ± 100	-0.24 ± 0.02	4.15 ^{+0.04} _{-0.03}	0.93 ^{+0.05} _{-0.03}	1.34 ^{+0.05} _{-0.04}	0.54 ^{+0.07} _{-0.06}	11 ± 2	0.14 ± 0.09
2M19043647+4519572	9008220	466	5800 ± 100	-0.01 ± 0.02	4.02 ^{+0.05} _{-0.04}	1.08 ^{+0.07} _{-0.06}	1.69 ± 0.07	0.32 ^{+0.05} _{-0.04}	8 ± 2	0.12 ^{+0.05} _{-0.06}
2M19214782+3951172	4742414	631	5800 ± 100	-0.02 ± 0.01	3.93 ± 0.03	1.12 ^{+0.06} _{-0.05}	1.91 ± 0.06	0.23 ± 0.02	7 ± 1	0.07 ^{+0.07} _{-0.05}
2M19371604+5004488	11818800	777	5000 ± 90	-0.55 ± 0.02	3.67 ± 0.04	0.87 ^{+0.04} _{-0.02}	2.3 ± 0.1	0.11 ± 0.02	12 ⁺¹ ₋₂	0.14 ^{+0.07} _{-0.08}
2M19473316+4123459	6061119	846	6000 ± 100	0.15 ± 0.02	4.16 ± 0.05	1.15 ^{+0.09} _{-0.08}	1.48 ± 0.08	0.50 ^{+0.09} _{-0.07}	6 ⁺³ ₋₂	0.50 ^{+0.03} _{-0.06}
2M19270249+4156386	6522242	855	5010 ± 90	-0.57 ± 0.02	4.42 ± 0.03	0.78 ± 0.02	0.90 ± 0.03	1.5 ^{+0.2} _{-0.1}	12.4 ^{+0.9} _{-1.7}	0.10 ^{+0.07} _{-0.06}
2M19001520+4410043	8218274	1064	6000 ± 300	-1.5 ± 0.1	4.14 ± 0.04	1.38 ± 0.07	1.65 ± 0.06	0.44 ^{+0.06} _{-0.05}	2.2 ^{+0.9} _{-0.7}	0.08 ^{+0.07} _{-0.05}
2M18535277+4503088	8801343	1247	6040 ± 90	-0.12 ± 0.01	3.85 ^{+0.05} _{-0.03}	1.29 ^{+0.14} _{-0.06}	2.24 ^{+0.07} _{-0.06}	0.16 ± 0.02	3.8 ^{+0.7} _{-1.2}	0.06 ^{+0.06} _{-0.04}
2M19160484+4807113	10790387	1288	6100 ± 100	0.04 ± 0.02	4.31 ± 0.04	1.05 ± 0.06	1.19 ± 0.05	0.9 ± 0.1	6 ⁺³ ₋₂	0.13 ^{+0.06} _{-0.07}
2M19320489+4230318	7037540	1347	5800 ± 100	-0.34 ± 0.02	4.27 ± 0.04	0.89 ^{+0.04} _{-0.03}	1.15 ^{+0.04} _{-0.05}	0.8 ± 0.1	11 ⁺² ₋₃	0.13 ^{+0.06} _{-0.07}
2M19282877+4255540	7363829	1356	5600 ± 100	0.17 ± 0.01	4.03 ^{+0.06} _{-0.05}	1.08 ^{+0.07} _{-0.06}	1.7 ± 0.1	0.33 ^{+0.07} _{-0.05}	9 ± 2	0.18 ^{+0.06} _{-0.07}
2M19460177+4927262	11517719	1416	5500 ± 100	-0.38 ± 0.02	3.88 ^{+0.07} _{-0.06}	0.94 ^{+0.06} _{-0.05}	1.9 ^{+0.2} _{-0.1}	0.21 ^{+0.05} _{-0.04}	10 ± 2	0.13 ^{+0.09} _{-0.08}
2M19191325+4629301	9705459	1448	5300 ± 90	0.09 ± 0.01	4.37 ± 0.03	0.92 ^{+0.04} _{-0.03}	1.04 ± 0.04	1.2 ± 0.1	11 ⁺² ₋₃	0.11 ^{+0.08} _{-0.06}
2M19344052+4622453	9653622	2513	5900 ± 100	-0.37 ± 0.02	4.3 ± 0.2	0.91 ^{+0.10} _{-0.06}	1.2 ^{+0.4} _{-0.2}	0.8 ^{+0.7} _{-0.5}	8 ± 3	0.13 ^{+0.09} _{-0.08}
2M19254244+4209507	6690171	3320	5030 ± 90	0.29 ± 0.01	4.52 ± 0.03	0.86 ± 0.03	0.85 ± 0.03	2.0 ± 0.2	10 ⁺³ ₋₄	0.17 ^{+0.07} _{-0.09}
2M19273337+3921423	4263529	3358	5300 ± 100	-0.16 ± 0.01	4.48 ± 0.02	0.83 ^{+0.03} _{-0.02}	0.87 ± 0.02	1.8 ± 0.1	11 ⁺² ₋₃	0.08 ± 0.05
2M19520793+3952594	4773392	4367	6300 ± 100	-0.02 ± 0.02	4.18 ± 0.05	1.17 ± 0.08	1.45 ^{+0.06} _{-0.05}	0.54 ^{+0.08} _{-0.07}	4 ± 2	0.27 ^{+0.06} _{-0.09}
2M19543478+4217089	6805414	5329	6200 ± 100	0.26 ± 0.02	4.12 ± 0.05	1.34 ^{+0.07} _{-0.08}	1.67 ± 0.09	0.41 ^{+0.07} _{-0.06}	3.1 ^{+1.2} _{-0.9}	0.55 ^{+0.05} _{-0.08}
2M19480000+4117241	5979863	6018	5700 ± 100	0.04 ± 0.01	4.43 ± 0.04	0.93 ^{+0.05} _{-0.04}	0.97 ± 0.04	1.4 ± 0.2	8 ⁺⁴ ₋₃	0.3 ± 0.1
2M19352118+4207199	6698670	6760	5850 ± 80	-0.13 ± 0.01	4.26 ± 0.03	0.96 ^{+0.06} _{-0.05}	1.20 ± 0.03	0.78 ^{+0.08} _{-0.07}	9 ± 3	0.13 ^{+0.06} _{-0.07}

^aThese are the calibrated values from the ASPCAP pipeline. All other parameters (M_* , R_* , ρ_* , Age, and A_V) are parameters in the SED fit using EXOFASTv2 using MIST isochrones.

Table 8. Model parameters for the KOI systems.

APOGEE ID	KIC ID	KOI	P	T_0	e	ω_*	K
			(days)	(BJD _{TDB})		(deg)	(km s ⁻¹)
2M18523991+4524110	9071386	23	4.693295 ± 0.000004	2455077.80838 ± 0.00004	0.0009 ^{+0.0033} _{-0.0007}	-60 ⁺¹⁵¹ ₋₃₀	17.7 ± 0.2
2M19395458+3840421	3558981	52	2.9878624 ± 0.0000003	2455598.58385 ± 0.00005	0.005 ^{+0.010} _{-0.003}	-40 ⁺⁹⁷ ₋₄₀	26.2 ± 0.4
2M19480226+5022203	11974540	129	24.669193 ± 0.000003	2454965.8633 ± 0.0001	0.08 ± 0.01	160 ⁺²⁰ ₋₃₀₀	5.9 ± 0.1
2M19492647+4025473	5297298	130	34.193602 ± 0.000003	2455432.81176 ± 0.00006	0.495 ± 0.008	136 ⁺¹ ₋₂	11.0 ± 0.2
2M19424111+4035566	5376836	182	3.4794244 ± 0.0000002	2455512.58740 ± 0.00002	0.001 ^{+0.007} _{-0.001}	-40 ⁺¹³⁰ ₋₆₀	20.2 ± 0.4
2M19485138+4139505	6305192	219	8.025118 ± 0.000002	2454965.4689 ± 0.0003	0.26 ± 0.02	-63 ± 4	3.47 ^{+0.10} _{-0.09}
2M19223275+3842276	3642741	242	7.258448 ± 0.000002	2455951.2350 ± 0.0001	0.007 ^{+0.008} _{-0.005}	0 ⁺⁶⁸ ₋₁₀₀	7.01 ^{+0.08} _{-0.07}
2M19073111+3922421	4247092	403	21.05649 ± 0.00002	2456541.250 ± 0.002	0.644 ± 0.004	165 ± 1	16.8 ± 0.3
2M19331345+4136229	6289650	415	166.7879 ± 0.0001	2455078.1422 ± 0.0005	0.701 ± 0.002	44.9 ± 0.3	3.36 ± 0.01
2M19043647+4519572	9008260	466	9.391039 ± 0.000004	2455003.5390 ± 0.0003	0.027 ^{+0.008} _{-0.007}	110 ± 10	7.95 ± 0.08
2M19214782+3951172	4742414	631	15.458053 ± 0.000003	2455006.7820 ^{+0.0002} _{-0.0001}	0.193 ± 0.004	-37 ± 2	6.74 ± 0.04
2M19371604+5004488	11818800	777	40.41940 ^{+0.00005} _{-0.00004}	2455006.566 ± 0.001	0.70 ^{+0.05} _{-0.03}	107 ± 4	15.0 ^{+1.8} _{-0.9}
2M19473316+4123459	6061119	846	27.807565 ± 0.000004	2455659.2861 ± 0.0001	0.37 ± 0.02	147 ⁺⁵ ₋₆	9.1 ^{+0.4} _{-0.3}
2M19270249+4156386	6522242	855	41.408310 ± 0.000006	2455028.7868 ± 0.0001	0.148 ± 0.003	118 ± 1	6.06 ± 0.02
2M19001520+4410043	8218274	1064	1.18735246 ± 0.0000003	2455754.86785 ^{+0.00007} _{-0.00006}	0.04 ± 0.02	120 ⁺³⁰ ₋₂₀	23.7 ^{+0.4} _{-0.5}
2M18535277+4503088	8801343	1247	2.739877 ± 0.000001	2455808.69158 ± 0.00001	0.006 ^{+0.007} _{-0.005}	-83 ⁺⁶ ₋₄	25.6 ± 0.4
2M19160484+4807113	10790387	1288	117.93111 ± 0.00007	2455052.7037 ± 0.0005	0.69 ± 0.01	4 ± 2	4.1 ± 0.1
2M19320489+4230318	7037540	1347	14.405857 ± 0.000001	2455582.34229 ± 0.00004	0.0055 ^{+0.0022} _{-0.0006}	-110 ⁺³⁰⁰ ₋₅₀	12.4 ± 0.2
2M19282877+4255540	7363829	1356	787.432 ± 0.002	2455168.816 ± 0.002	0.66 ± 0.02	107 ⁺⁸ ₋₇	2.4 ± 0.1
2M19460177+4927262	11517719	1416	2.4957813 ± 0.0000005	2456073.96726 ± 0.00002	0.0007 ^{+0.0014} _{-0.0004}	-40 ⁺¹¹⁰ ₋₄₀	24.5 ± 0.4
2M19191325+4629301	9705459	1448	2.4865864 ± 0.0000004	2456212.88899 ± 0.00002	0.002 ^{+0.007} _{-0.002}	-70 ⁺¹³² ₋₁₀	23.3 ± 0.3
2M19344052+4622453	9653622	2513	19.00547 ± 0.00005	2454977.152 ± 0.003	0.36 ± 0.03	-154 ⁺⁷ ₋₈	2.0 ± 0.1
2M19254244+4209507	6690171	3320	85.06240 ± 0.00003	2455832.8434 ± 0.0001	0.27 ^{+0.04} _{-0.03}	116 ± 2	7.6 ^{+0.2} _{-0.1}
2M19273337+3921423	4263529	3358	10.104042 ± 0.000004	2455652.9675 ± 0.0002	0.009 ± 0.006	-70 ⁺³⁰ ₋₁₀	16.66 ^{+0.1} _{-0.09}
2M19520793+3952594	4773392	4367	170.996 ± 0.002	2454996.97 ± 0.01	0.85 ^{+0.02} _{-0.01}	-57 ± 2	11.5 ^{+0.9} _{-0.4}
2M19543478+4217089	6805414	5329	200.2348 ± 0.0005	2455138.446 ± 0.002	0.66 ^{+0.08} _{-0.05}	-59 ± 5	6 ± 1
2M19480000+4117241	5979863	6018	16.6218543 ± 0.0000009	2455697.91363 ± 0.00004	0.119 ^{+0.009} _{-0.011}	75 ⁺¹ ₋₂	14.4 ± 0.2
2M19352118+4207199	6698670	6760	10.81593 ± 0.00003	2455351.34940 ± 0.00003	0.1529 ^{+0.0006} _{-0.0005}	9 ± 1	16.67 ^{+0.06} _{-0.07}

γ_{APOGEE}	γ_{HPF}	γ_{SOPHIE}	i	a/R_*	R_2/R_*	A_T
(km s ⁻¹)	(km s ⁻¹)	(km s ⁻¹)	(deg)			(ppm)
-55.1 ± 0.1	86.51 ± 0.06	7.11 ^{+0.03} _{-0.02}	0.1131 ± 0.0001	273 ± 7
-46.8 ^{+0.3} _{-0.2}	85.7 ± 0.1	8.79 ^{+0.12} _{-0.09}	0.2018 ± 0.0009	1950 ± 30
16.6 ± 0.1	...	15.6 ± 0.2	89.22 ± 0.07	27.2 ± 0.7	0.0796 ± 0.0002	...
20.92 ± 0.09	87.53 ± 0.08	27.6 ± 0.4	0.1141 ± 0.0002	...
-59.8 ± 0.4	84.40 ± 0.05	7.00 ± 0.03	0.1365 ± 0.0001	480 ± 10
-8.07 ± 0.07	...	-8.41 ± 0.06	87.4 ^{+0.5} _{-0.3}	11.8 ^{+1.0} _{-0.5}	0.0539 ^{+0.0005} _{-0.0011}	...
-44.56 ± 0.06	88.2 ^{+0.9} _{-0.6}	9.8 ± 0.3	0.0560 ± 0.0005	...
-22.6 ± 0.1	83.9 ± 0.6	23.9 ^{+0.7} _{-0.6}	0.3 ± 0.1	...
-1.26 ± 0.03	...	-1.481 ± 0.006	89.2 ± 0.3	98 ⁺⁶ ₋₇	0.064 ± 0.001	...
-56.50 ± 0.06	...	-56.75 ^{+0.09} _{-0.08}	85.4 ± 0.2	12.1 ± 0.4	0.073 ± 0.004	...
-56.43 ± 0.05	-56.45 ± 0.03	...	89.2 ± 0.2	15.5 ± 0.2	0.0599 ± 0.0002	...
-3.8 ^{+0.3} _{-0.2}	83 ± 1	24 ⁺² ₋₁	0.088 ^{+0.005} _{-0.002}	...
-16.8 ^{+0.3} _{-0.2}	88.1 ^{+0.1} _{-0.2}	33 ± 1	0.1619 ± 0.0004	...
-94.87 ± 0.07	...	-94.89 ± 0.02	89.78 ^{+0.09} _{-0.07}	61.7 ^{+0.7} _{-0.8}	0.136 ± 0.001	...
4.4 ± 0.4	80.6 ± 0.4	3.19 ^{+0.05} _{-0.06}	0.1144 ^{+0.0002} _{-0.0003}	...
3.2 ± 0.2	81.93 ^{+0.11} _{-0.09}	4.86 ± 0.03	0.1371 ± 0.0001	668 ± 4
6.84 ± 0.08	...	6.5 ± 0.1	89.6 ± 0.2	109 ± 7	0.085 ^{+0.002} _{-0.001}	...
-32.4 ± 0.1	89.89 ^{+0.07} _{-0.1}	23.2 ± 0.1	0.1587 ± 0.0002	530 ± 10
13.83 ± 0.07	89.72 ^{+0.08} _{-0.09}	220 ± 10	0.0733 ^{+0.0010} _{-0.0009}	...
-43.5 ± 0.3	88.3 ± 0.2	5.24 ± 0.01	0.1459 ± 0.0001	914 ± 9
-54.6 ± 0.2	86.89 ^{+0.06} _{-0.05}	7.74 ^{+0.05} _{-0.03}	0.1886 ± 0.0003	890 ± 20
11.12 ^{+0.07} _{-0.06}	89.7 ^{+0.2} _{-2.4}	100 ⁺³⁰ ₋₈₀	0.022 ^{+0.204} _{-0.002}	...
12.27 ^{+0.09} _{-0.10}	89.34 ^{+0.04} _{-0.06}	97 ± 3	0.225 ^{+0.007} _{-0.005}	...
8.87 ± 0.06	86.9 ^{+0.3} _{-0.4}	23.1 ± 0.5	0.3 ± 0.1	...
-20.4 ^{+0.2} _{-0.3}	89.2 ± 0.1	102 ± 5	0.3 ± 0.1	...
-24.5 ^{+0.6} _{-0.7}	89.71 ^{+0.03} _{-0.04}	100 ⁺⁷ ₋₆	0.1012 ^{+0.0008} _{-0.0009}	...
10.0 ± 0.1	88.80 ± 0.03	31.1 ^{+0.4} _{-0.3}	0.2242 ± 0.0005	1290 ± 30
-38.48 ^{+0.05} _{-0.04}	89.28 ± 0.03	19.74 ± 0.08	0.1971 ± 0.0003	830 ± 20

Table 9. Derived physical parameters for the KOI systems.

APOGEE ID	KIC ID	KOI	R_2 (R_J)	M_2 (M_J)	q	a (au)	$\log g_2$ (dex)	ρ_2 (g cm^{-3})
2M18523991+4524110	9071386	23	2.22 ± 0.06	204^{+6}_{-8}	$0.13^{+0.007}_{-0.010}$	0.067 ± 0.002	5.036 ± 0.005	23 ± 2
2M19395458+3840421	3558981	52	$1.91^{+0.06}_{-0.05}$	195 ± 5	$0.211^{+0.008}_{-0.007}$	0.040 ± 0.001	5.09 ± 0.01	35 ± 3
2M19480226+5022203	11974540	129	1.31 ± 0.04	103^{+4}_{-7}	$0.078^{+0.006}_{-0.009}$	0.214 ± 0.008	5.30 ± 0.03	57^{+5}_{-6}
2M19492647+4025473	5297298	130	2.03 ± 0.06	187^{+10}_{-8}	$0.15^{+0.02}_{-0.01}$	0.235 ± 0.008	5.08 ± 0.01	28 ± 3
2M19424111+4035566	5376836	182	2.05 ± 0.06	174^{+8}_{-7}	0.16 ± 0.01	0.050 ± 0.002	5.05 ± 0.01	25^{+3}_{-2}
2M19485138+4139505	6305192	219	$0.8^{+0.3}_{-0.2}$	37^{+4}_{-2}	$0.031^{+0.006}_{-0.004}$	$0.08^{+0.03}_{-0.02}$	$5.16^{+0.08}_{-0.05}$	100^{+100}_{-60}
2M19223275+3842276	3642741	242	0.97 ± 0.04	77^{+5}_{-3}	$0.063^{+0.008}_{-0.004}$	0.081 ± 0.004	5.33 ± 0.04	110 ± 10
2M19073111+3922421	4247092	403	4 ± 2	208^{+10}_{-9}	$0.18^{+0.02}_{-0.01}$	0.166 ± 0.007	$4.5^{+0.4}_{-0.3}$	3 ± 4
2M19331345+4136229	6289650	415	$0.83^{+0.04}_{-0.03}$	65^{+2}_{-1}	$0.066^{+0.004}_{-0.003}$	$0.61^{+0.04}_{-0.05}$	$5.39^{+0.06}_{-0.09}$	140 ± 20
2M19043647+4519572	9008220	466	1.19 ± 0.08	92^{+4}_{-3}	$0.081^{+0.006}_{-0.005}$	0.095 ± 0.005	$5.23^{+0.06}_{-0.07}$	70 ± 10
2M19214782+3951172	4742414	631	1.11 ± 0.03	92 ± 3	$0.078^{+0.005}_{-0.004}$	0.137 ± 0.005	$5.32^{+0.01}_{-0.02}$	83 ± 8
2M19371604+5004488	11818800	777	$1.9^{+0.2}_{-0.1}$	190^{+30}_{-20}	$0.21^{+0.03}_{-0.02}$	0.25 ± 0.02	$5.17^{+0.07}_{-0.06}$	32^{+9}_{-6}
2M19473316+4123459	6061119	846	2.3 ± 0.1	150^{+10}_{-9}	0.12 ± 0.01	0.23 ± 0.02	4.98 ± 0.04	15^{+3}_{-2}
2M19270249+4156386	6522242	855	$1.20^{+0.05}_{-0.04}$	93^{+2}_{-1}	$0.114^{+0.004}_{-0.003}$	0.26 ± 0.01	5.34 ± 0.02	67 ± 8
2M19001520+4410043	8218274	1064	1.83 ± 0.06	167^{+6}_{-7}	$0.115^{+0.007}_{-0.008}$	0.0244 ± 0.0009	5.06 ± 0.02	34 ± 4
2M18535277+4503088	8801343	1247	2.98 ± 0.09	235^{+20}_{-8}	$0.17^{+0.02}_{-0.01}$	$0.050^{+0.002}_{-0.001}$	$4.935^{+0.009}_{-0.008}$	11 ± 1
2M19160484+4807113	10790387	1288	$0.98^{+0.05}_{-0.04}$	78 ± 4	0.071 ± 0.006	$0.60^{+0.05}_{-0.04}$	$5.49^{+0.07}_{-0.08}$	100^{+20}_{-10}
2M19320489+4230318	7037540	1347	1.77 ± 0.07	152^{+5}_{-4}	$0.162^{+0.010}_{-0.007}$	0.124 ± 0.005	$5.126^{+0.006}_{-0.007}$	34 ± 4
2M19282877+4255540	7363829	1356	1.19 ± 0.07	93^{+7}_{-6}	$0.082^{+0.008}_{-0.007}$	1.7 ± 0.1	$5.17^{+0.05}_{-0.06}$	70 ± 10
2M19460177+4927262	11517719	1416	2.6 ± 0.2	175^{+8}_{-7}	0.18 ± 0.01	0.045 ± 0.004	4.965 ± 0.008	12 ± 3
2M19191325+4629301	9705459	1448	$1.91^{+0.08}_{-0.07}$	163^{+5}_{-4}	$0.169^{+0.008}_{-0.006}$	$0.038^{+0.002}_{-0.001}$	$5.062^{+0.008}_{-0.007}$	29^{+4}_{-3}
2M19344052+4622453	9653622	2513	$0.25^{+2.00}_{-0.05}$	23 ± 2	$0.025^{+0.004}_{-0.003}$	$0.5^{+0.2}_{-0.4}$	$7^{+0.2}_{-0.3}$	2000^{+50000}_{-1000}
2M19254244+4209507	6690171	3320	$1.86^{+0.08}_{-0.07}$	160^{+7}_{-5}	$0.178^{+0.010}_{-0.008}$	0.38 ± 0.02	$5.06^{+0.03}_{-0.04}$	31 ± 4
2M19273337+3921423	4263529	3358	2 ± 1	177^{+4}_{-3}	$0.204^{+0.009}_{-0.007}$	0.093 ± 0.003	$4.9^{+0.5}_{-0.4}$	20 ± 20
2M19520793+3952594	4773392	4367	4 ± 2	200^{+30}_{-10}	0.16 ± 0.02	0.69 ± 0.04	$4.5^{+0.5}_{-0.3}$	4^{+6}_{-5}
2M19543478+4217089	6805414	5329	1.64 ± 0.09	170^{+40}_{-30}	$0.12^{+0.03}_{-0.02}$	$0.77^{+0.07}_{-0.06}$	5.2 ± 0.1	50 ± 10
2M19480000+4117241	5979863	6018	2.13 ± 0.08	194^{+7}_{-6}	0.20 ± 0.01	$0.141^{+0.006}_{-0.005}$	5.08 ± 0.01	25 ± 3
2M19352118+4207199	6698670	6760	2.31 ± 0.06	197^{+8}_{-6}	0.20 ± 0.01	0.111 ± 0.003	5.046 ± 0.004	20 ± 2

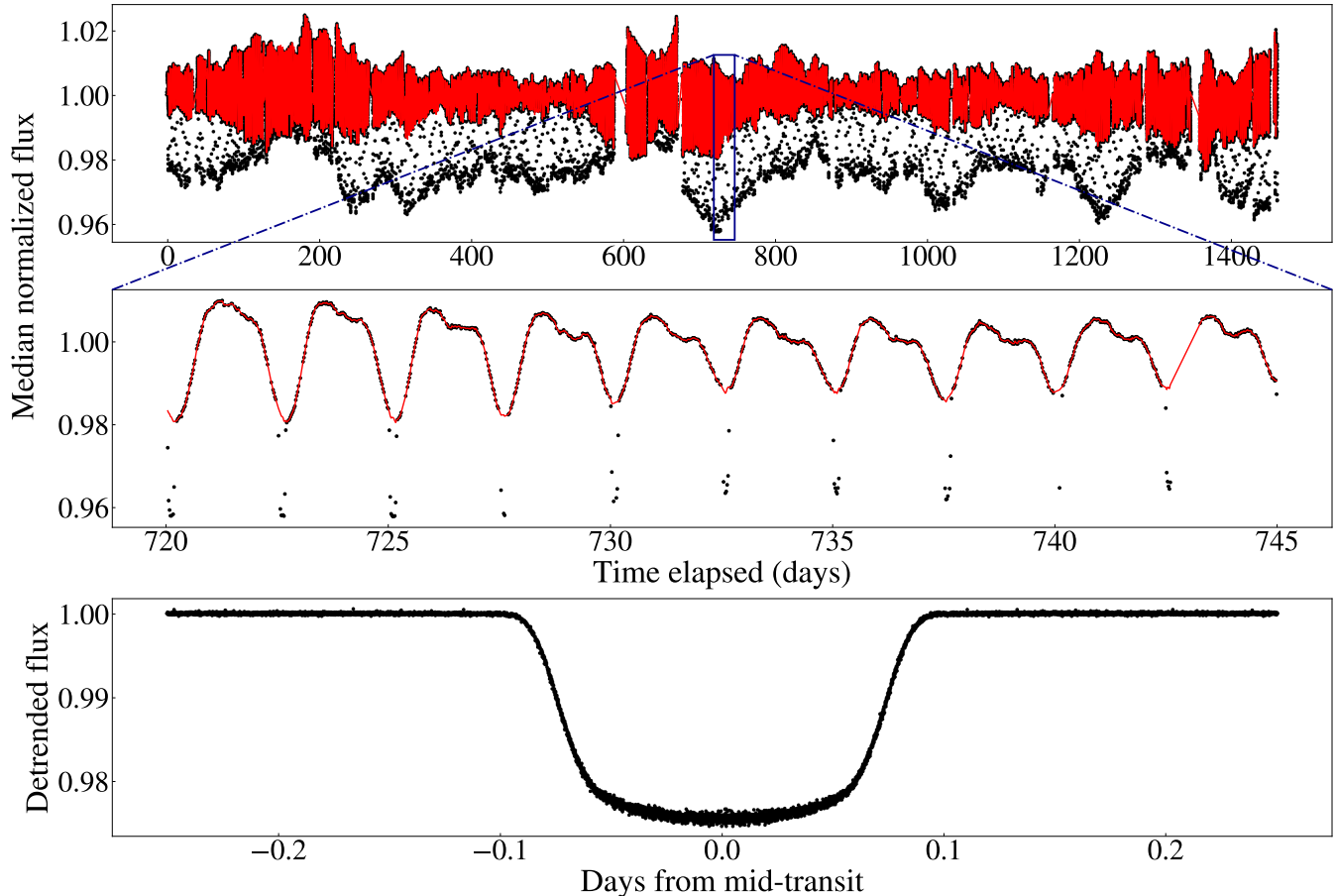


Figure 6. Gaussian process detrending. The example above shows the detrending result for one quarter of long-cadence data for KOI-1416. The out-of-transit photometric variability in the *Kepler* light curve can be modeled using a quasi-periodic kernel. The top panel shows the flux (black points) normalized to the median value while the middle panel is a magnification to the region highlighted by the rectangle. The red line is the maximum *a posteriori* model. The bottom panel shows the phase-folded photometry, once the baseline found by the Gaussian process is removed. No additional processing (e.g., sigma clipping) is performed.

B. PHOTOMETRIC ROTATION PERIOD

We use the available *Kepler* photometry to derive the stellar rotation period. The *Kepler* team notes (see Section 5.15 in Van Cleve et al. 2016) that long period signals may be attenuated in the PDCSAP flux and suggest searching for long-period signals in the SAP flux after detrending with the co-trending basis vectors (CBVs; Aigrain et al. 2017; Cui et al. 2019). We employ the ARC2¹¹ pipeline (Aigrain et al. 2017) to correct for systematics in the *Kepler* SAP light curve. The ARC2 pipeline detects and removes isolated discontinuities and the instrument systematic trends from the photometry by using the CBVs (see Kinemuchi et al. 2012). All light curves derived from ARC2 used seven CBVs for detrending.

To derive the rotation period and an estimate of its uncertainty, we modeled the *Kepler* photometry using the *juliet* analysis package (Espinoza et al. 2019). We adopt the photometric model from

¹¹ <https://github.com/OxES/OxKeplerSC>

Equation A1 and perform the parameter estimation using the dynamic nested-sampling algorithm *dynesty* (Speagle 2020). We placed a broad uniform prior on the rotation period of 1 – 1500 days. Table 10 lists the rotation periods for the KOIs. We do not report a rotation period for systems where the period of the Gaussian process coincides with the orbital period (KOI-23, KOI-855, KOI-1064, KOI-1247). A few systems (KOI-130, KOI-415, KOI-1288, KOI-1347, KOI-1356, KOI-2513) had no significantly detected rotation period ($P_{GP}/\sigma_{P_{GP}} < 5$) but are included in Table 10 for reference. Figure 7a is an example of a system where the observed photometric modulation is due to ellipsoidal variations. Figure 7b displays a system where the measured period of the Gaussian process model differs from the orbital period and we interpret the period of the Gaussian process to reflect the rotation period of such stars.

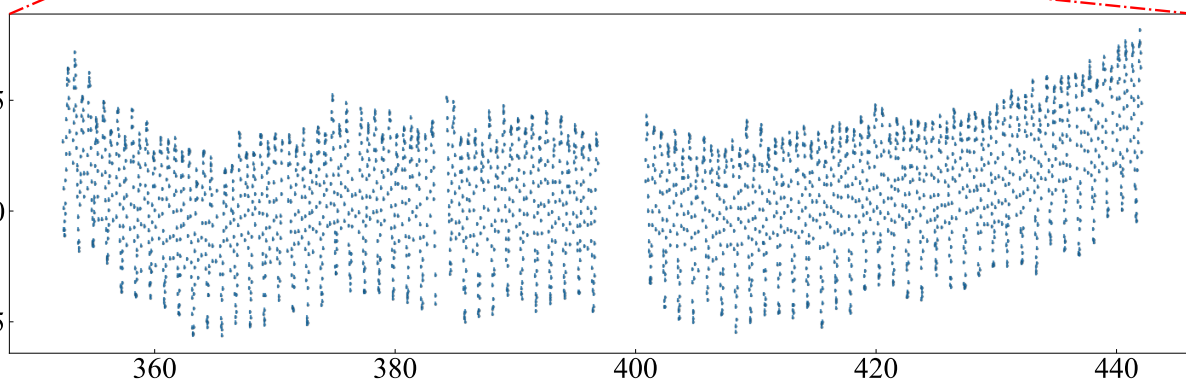
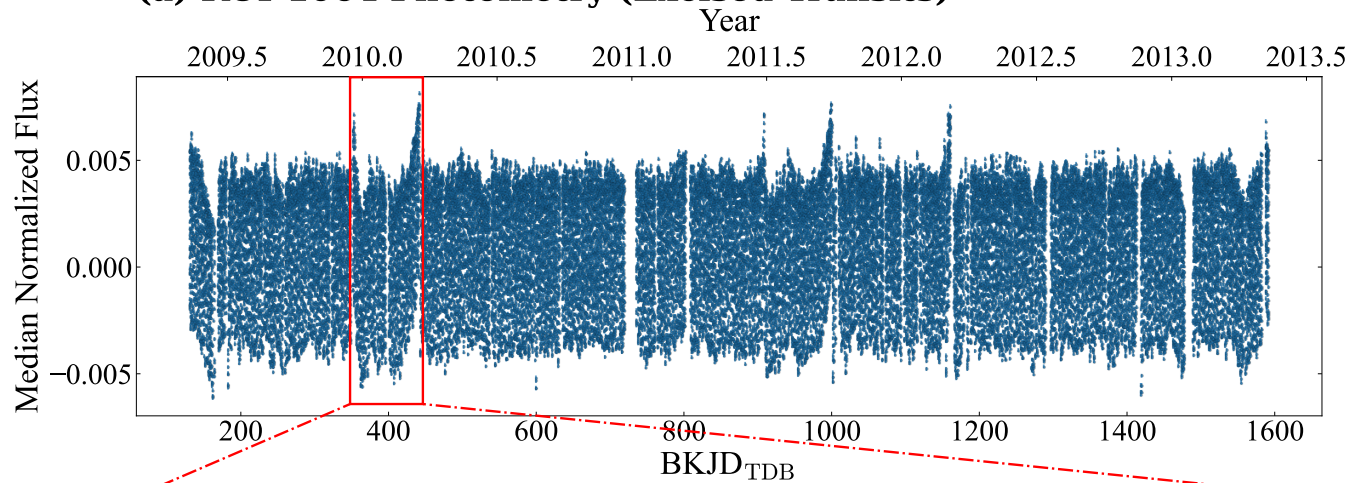
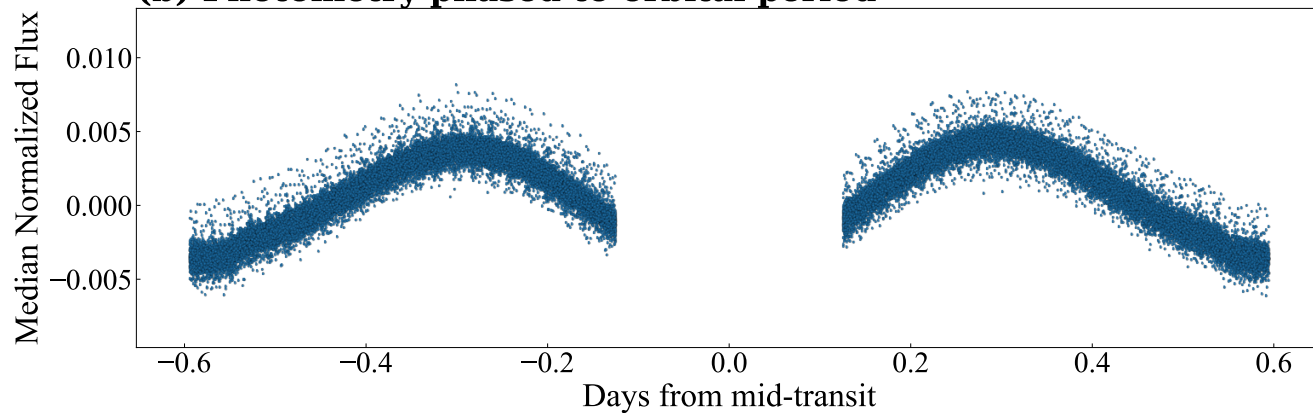
(a) KOI-1064 Photometry (Excised Transits)**(b) Photometry phased to orbital period**

Figure 7a. (a) The ARC2 corrected light curve for KOI-1064, after excising the transits, with an inset displaying the quarter 2 data. (b) The out-of-transit photometric variability after phasing to the orbital ephemeris. This is an example system where the variability is consistent with ellipsoidal variations. The complete figure set for the KOIs (28 images) is available in the online journal.

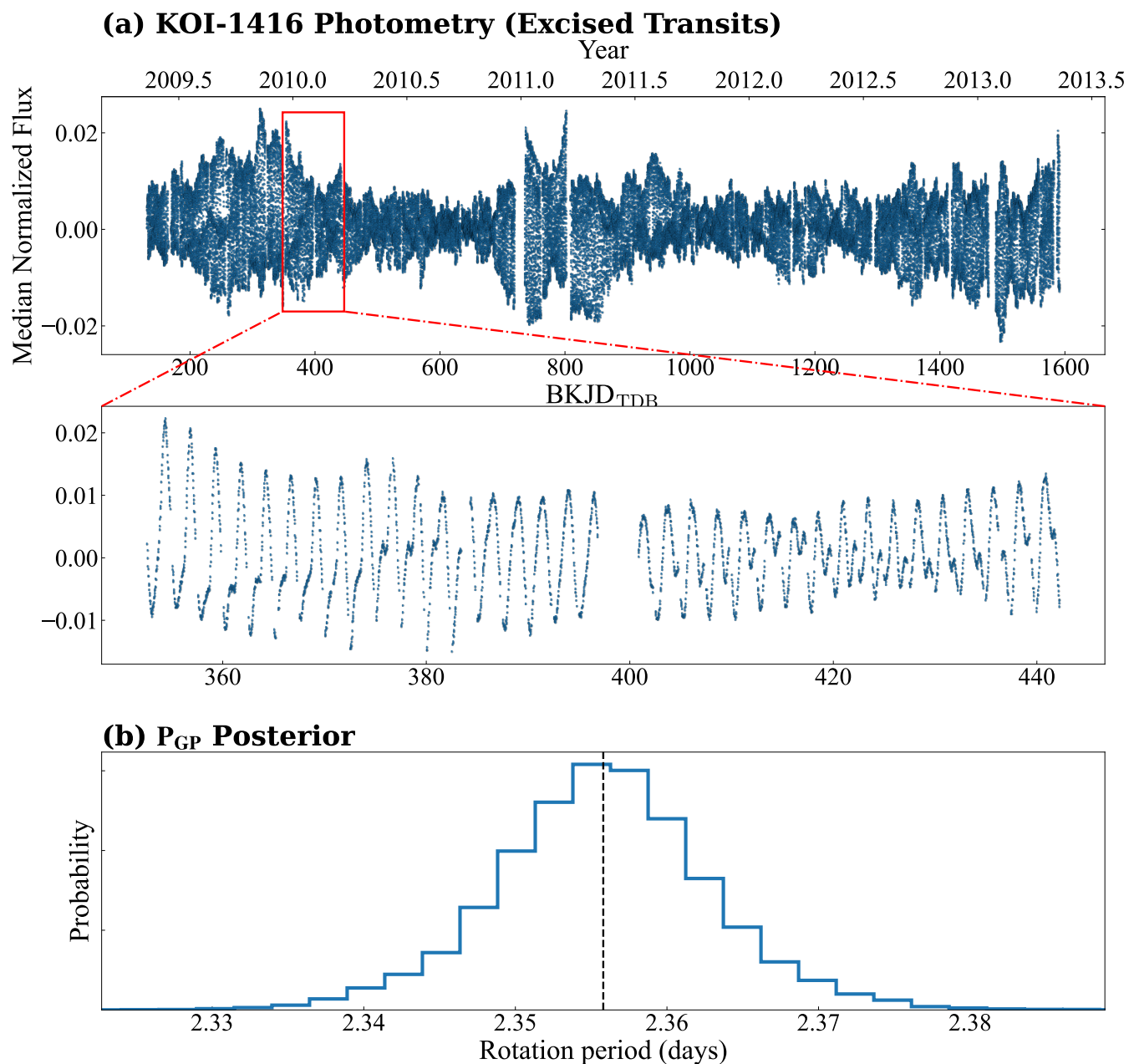


Figure 7b. Figure 7 (cont.). (a) The ARC2 corrected light curve for KOI-1416, after excising the transits, with an inset displaying a subset of the *Kepler* data. (b) The posterior distribution for the Gaussian process period, which we interpret as a measurement of the stellar rotation period. This is an example system where the variability is different from the measured orbital period.

Table 10. Stellar rotation period of the KOI systems.

APOGEE ID	KIC ID	KOI ID	Rotation Period ^a (d)	Orbital Period ^b (d)
2M18523991+4524110	9071386	23	...	4.693
2M19395458+3840421	3558981	52	3.345 ± 0.009	2.988
2M19480226+5022203	11974540	129	1.553 ± 0.005	24.669
2M19492647+4025473	5297298	130	3.37 ± 0.04	34.194
2M19424111+4035566	5376836	182	3.475 ± 0.009	3.479
2M19485138+4139505	6305192	219	$7.3^{+0.2}_{-0.1}$	8.025
2M19223275+3842276	3642741	242	8.4 ± 0.2	7.258
2M19073111+3922421	4247092	403	2.6323 ± 0.0004	21.056
2M19331345+4136229	6289650	415	$16.8^{+40}_{-0.2}$	166.788
2M19043647+4519572	9008220	466	12.5 ± 0.2	9.391
2M19214782+3951172	4742414	631	8.09 ± 0.08	15.458
2M19371604+5004488	11818800	777	11.01 ± 0.07	40.420
2M19473316+4123459	6061119	846	2.61 ± 0.01	27.808
2M19270249+4156386	6522242	855	...	41.408
2M19001520+4410043	8218274	1064	...	1.187
2M18535277+4503088	8801343	1247	...	2.740
2M19160484+4807113	10790387	1288	$6.79^{+0.1}_{-0.04}$	117.931
2M19320489+4230318	7037540	1347	10^{+50}_{-10}	14.406
2M19282877+4255540	7363829	1356	50^{+30}_{-50}	384.026
2M19460177+4927262	11517719	1416	2.356 ± 0.007	2.496
2M19191325+4629301	9705459	1448	2.744 ± 0.006	2.487
2M19344052+4622453	9653622	2513	$15.01^{+0.5}_{-0.03}$	19.005
2M19254244+4209507	6690171	3320	$14.9^{+0.2}_{-0.3}$	85.062
2M19273337+3921423	4263529	3358	$15.25^{+0.08}_{-0.07}$	10.104
2M19520793+3952594	4773392	4367	3.01 ± 0.01	170.996
2M19543478+4217089	6805414	5329	2.68 ± 0.01	200.235
2M19480000+4117241	5979863	6018	10.3 ± 0.4	16.622
2M19352118+4207199	6698670	6760	$7.0^{+0.2}_{-2.0}$	10.816

^aEmpty rows indicate the photometric variability occurs at the orbital period.

^bThe period of the orbit as listed in the DR25 KOI supplemental table.

Fig. Set2. Photometry and RVs for the sample of 28 KOIs The Kepler photometry and RVs for all systems analyzed in this work.

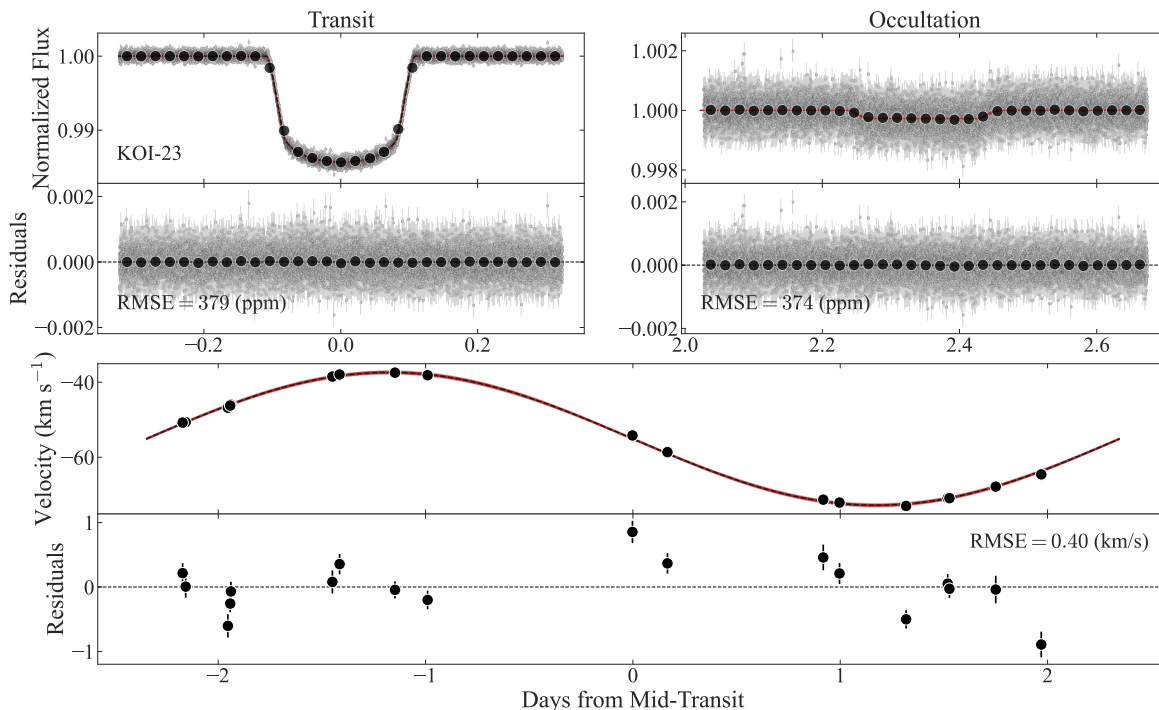


Fig. Set 2.1 – KOI-23. Top. The Kepler photometry center on the transit (left) and occultation (right) for KOI-23 after phase-folding to the derived ephemeris. The large circles represent 30 min bins of the raw data. **Bottom.** The RVs after phase-folding the data to the derived ephemeris. In each panel, the 1σ (darkest), 2σ , and 3σ (brightest) extent of the models are shown for reference.

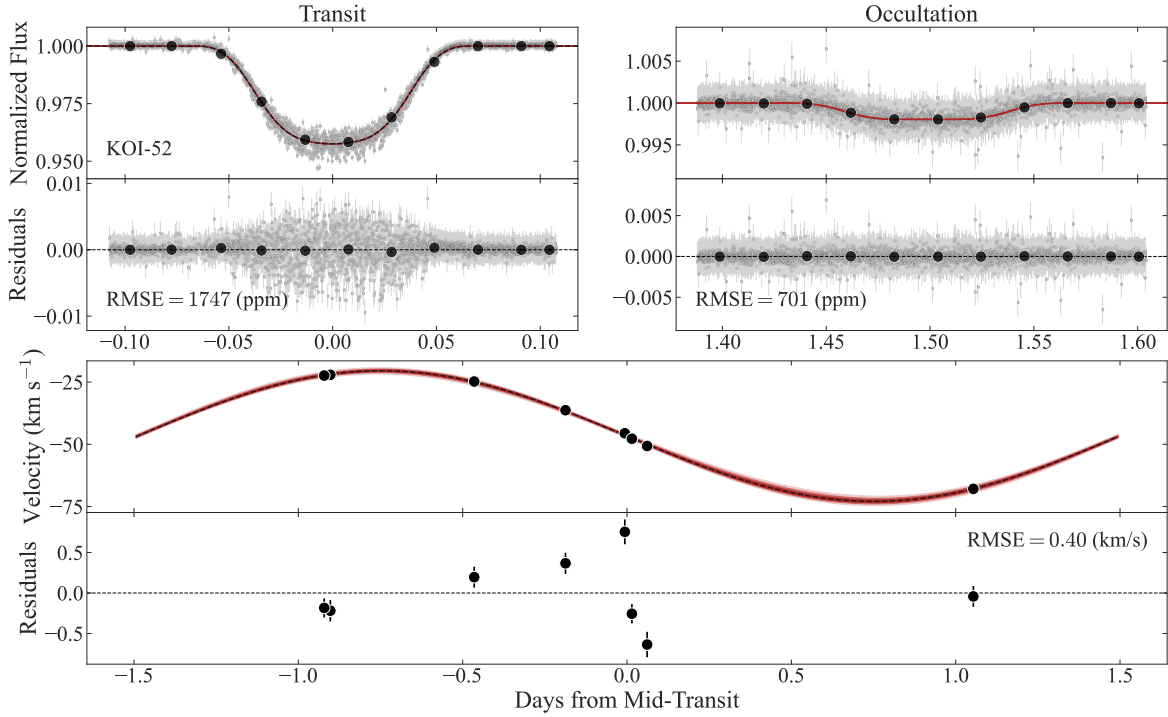


Fig. Set 2.2 – KOI-52. **Top.** The Kepler photometry center on the transit (left) and occultation (right) for KOI-52 after phase-folding to the derived ephemeris. The large circles represent 30 min bins of the raw data. **Bottom.** The RVs after phase-folding the data to the derived ephemeris. In each panel, the 1σ (darkest), 2σ , and 3σ (brightest) extent of the models are shown for reference.

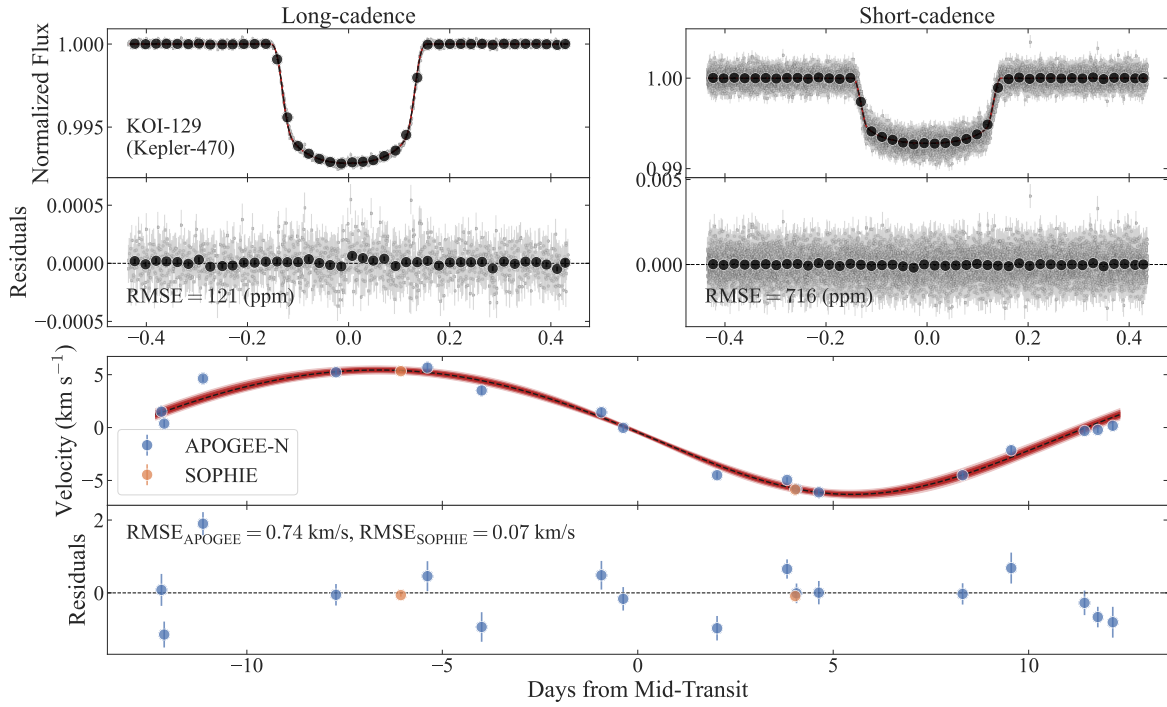


Fig. Set 2.3 – KOI-129. Top. The long-cadence (left) and short-cadence (right) Kepler photometry for KOI-129 after phase-folding to the derived ephemeris. The large circles represent 30 min bins of the raw data. **Bottom.** The RVs after removing instrumental offsets and phase-folding the data to the derived ephemeris. In each panel, the 1σ (darkest), 2σ , and 3σ (brightest) extent of the models are shown for reference.

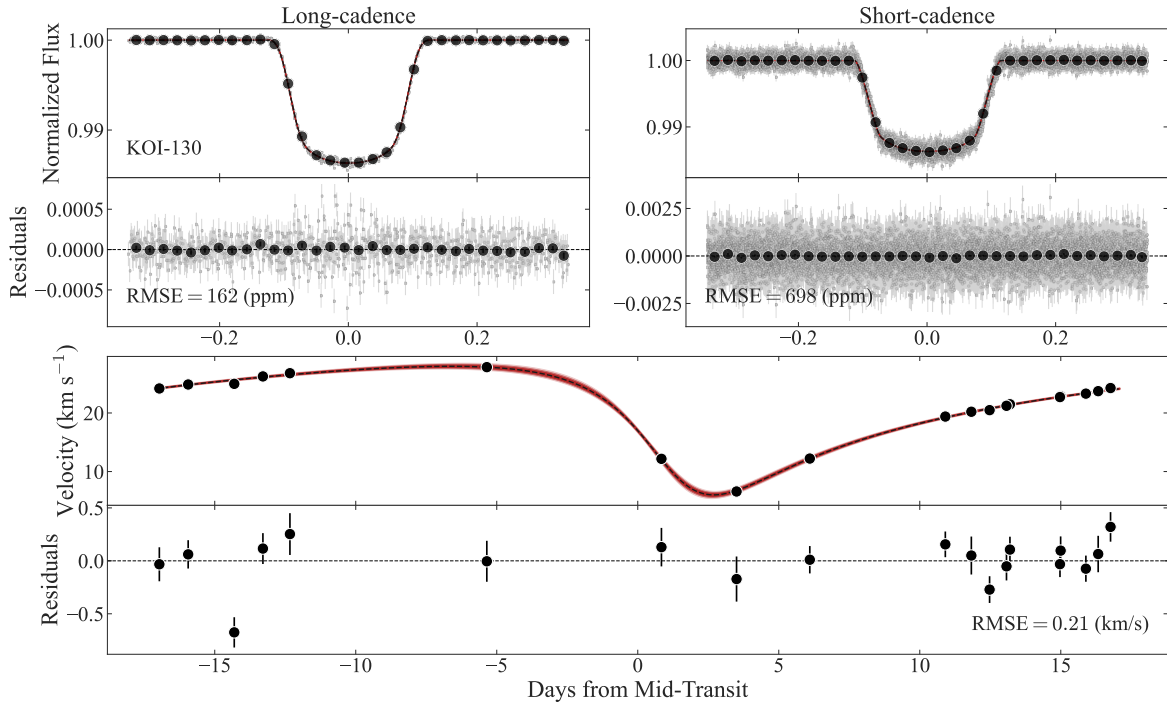


Fig. Set 2.4 – KOI-130. Top. The long-cadence (left) and short-cadence (right) Kepler photometry for KOI-130 after phase-folding to the derived ephemeris. The large circles represent 30 min bins of the raw data. **Bottom.** The RVs after phase-folding the data to the derived ephemeris. In each panel, the 1σ (darkest), 2σ , and 3σ (brightest) extent of the models are shown for reference.

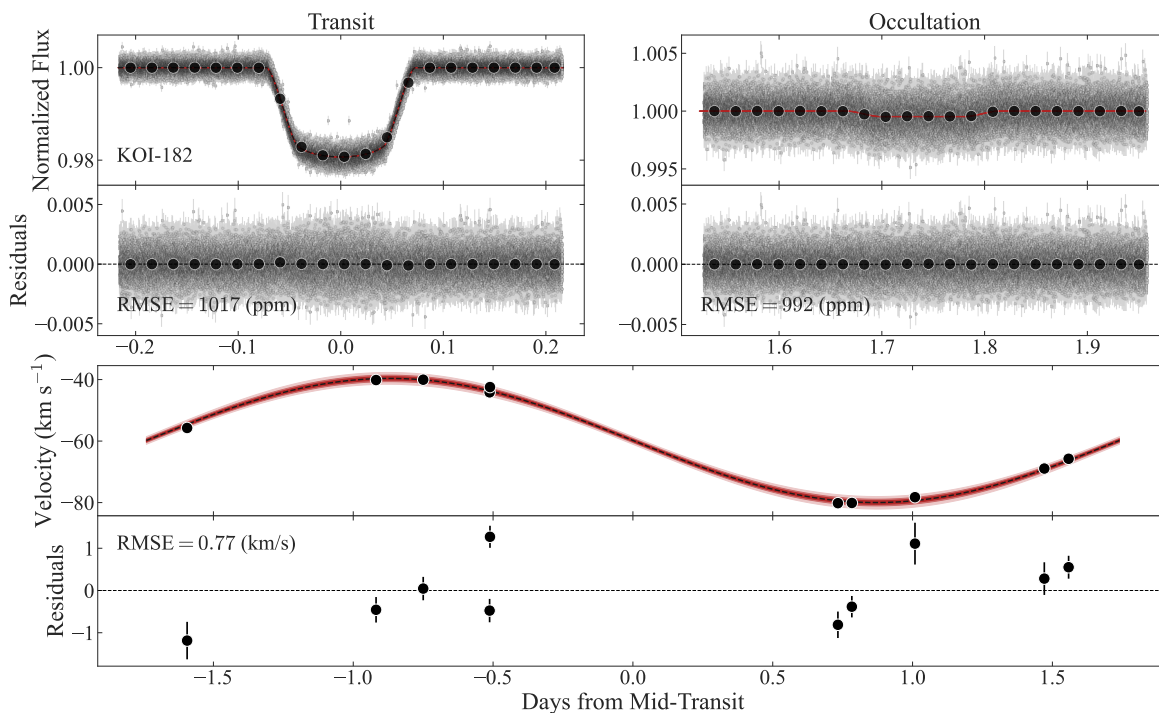


Fig. Set 2.5 – KOI-182. Top. The Kepler photometry center on the transit (left) and occultation (right) for KOI-182 after phase-folding to the derived ephemeris. The large circles represent 30 min bins of the raw data. **Bottom.** The RVs after phase-folding the data to the derived ephemeris. In each panel, the 1σ (darkest), 2σ , and 3σ (brightest) extent of the models are shown for reference.

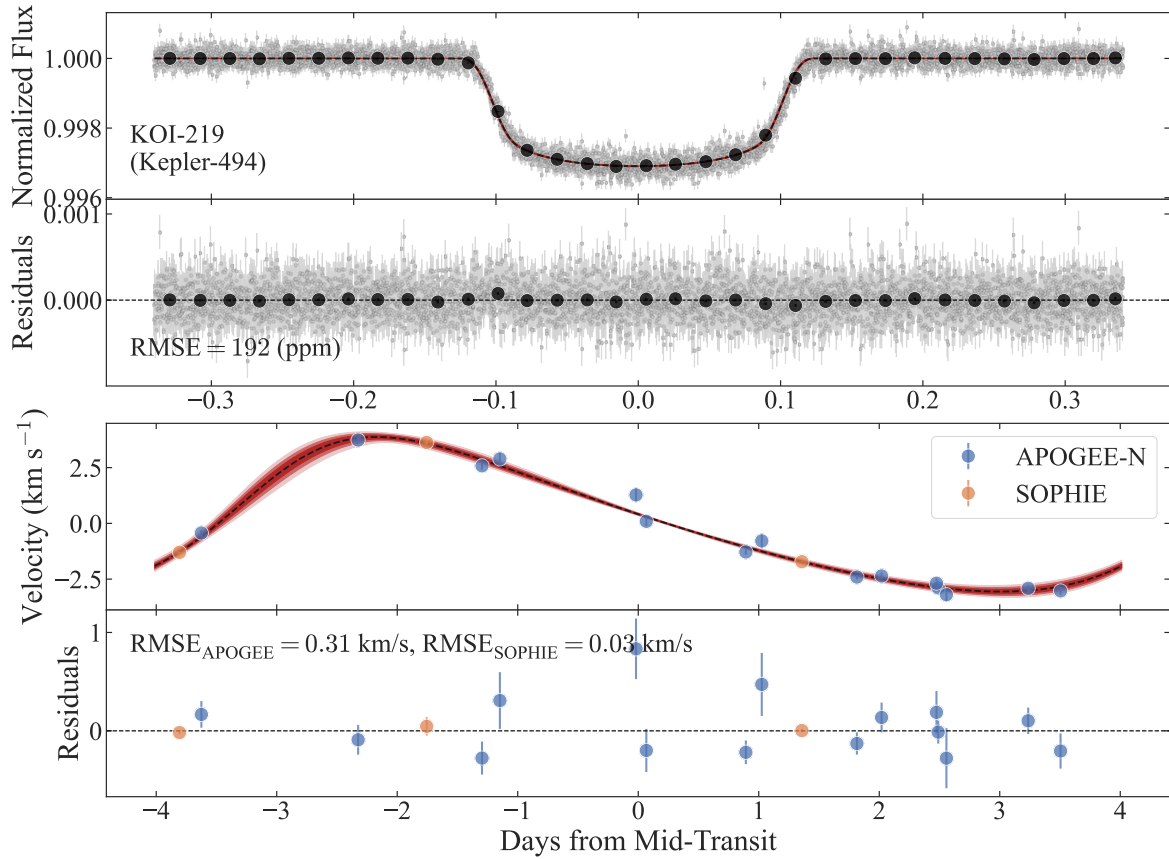


Fig. Set 2.6 – KOI-219. Top. The Kepler photometry for KOI-219 after phase-folding to the derived ephemeris. The large circles represent 30 min bins of the raw data. **Bottom.** The RVs after removing instrumental offsets and phase-folding the data to the derived ephemeris. In each panel, the 1σ (darkest), 2σ , and 3σ (brightest) extent of the models are shown for reference.

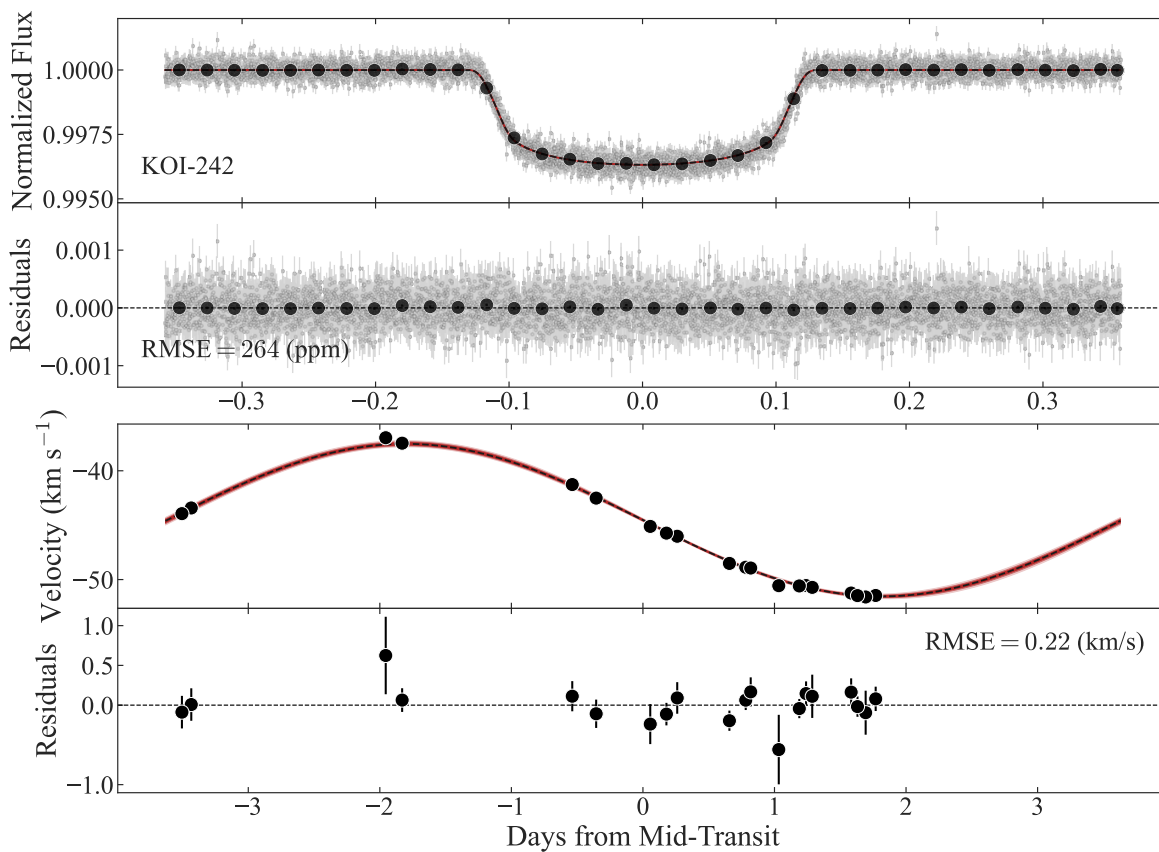


Fig. Set 2.7 – KOI-242. **Top.** The Kepler photometry for KOI-242 after phase-folding to the derived ephemeris. The large circles represent 30 min bins of the raw data. **Bottom.** The RVs after phase-folding the data to the derived ephemeris. In each panel, the 1σ (darkest), 2σ , and 3σ (brightest) extent of the models are shown for reference.

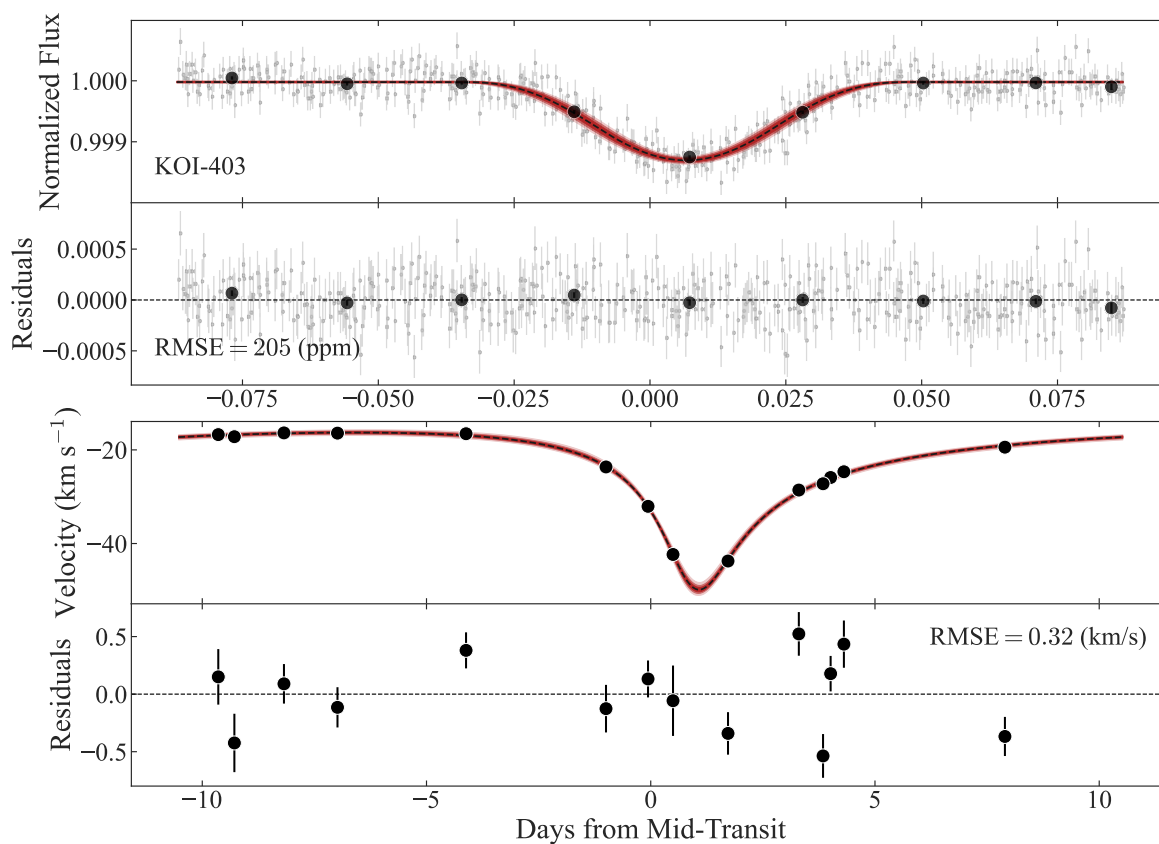


Fig. Set 2.8 – KOI-403. Top. The Kepler photometry for KOI-403 after phase-folding to the derived ephemeris. The large circles represent 30 min bins of the raw data. **Bottom.** The RVs after phase-folding the data to the derived ephemeris. In each panel, the 1σ (darkest), 2σ , and 3σ (brightest) extent of the models are shown for reference.

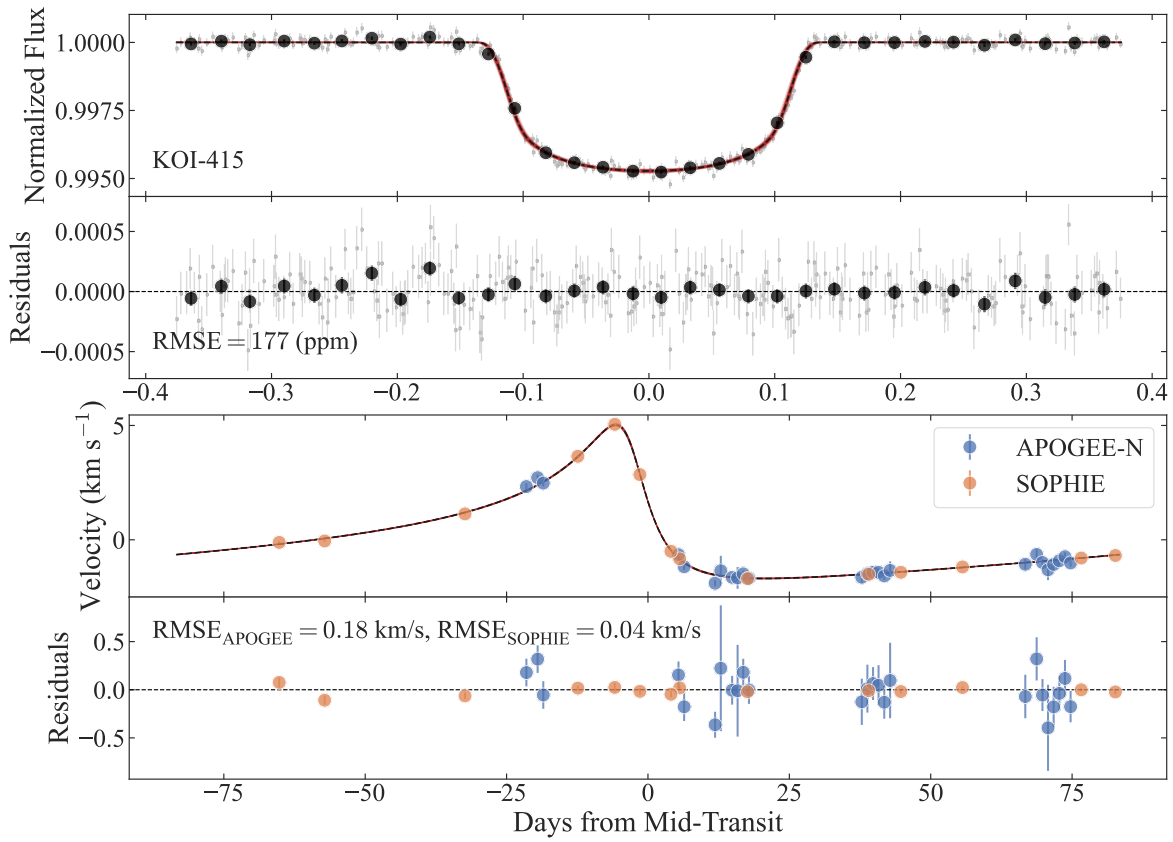


Fig. Set 2.9 – KOI-415. Top. The Kepler photometry for KOI-415 after phase-folding to the derived ephemeris. The large circles represent 30 min bins of the raw data. **Bottom.** The RVs after removing instrumental offsets and phase-folding the data to the derived ephemeris. In each panel, the 1σ (darkest), 2σ , and 3σ (brightest) extent of the models are shown for reference.

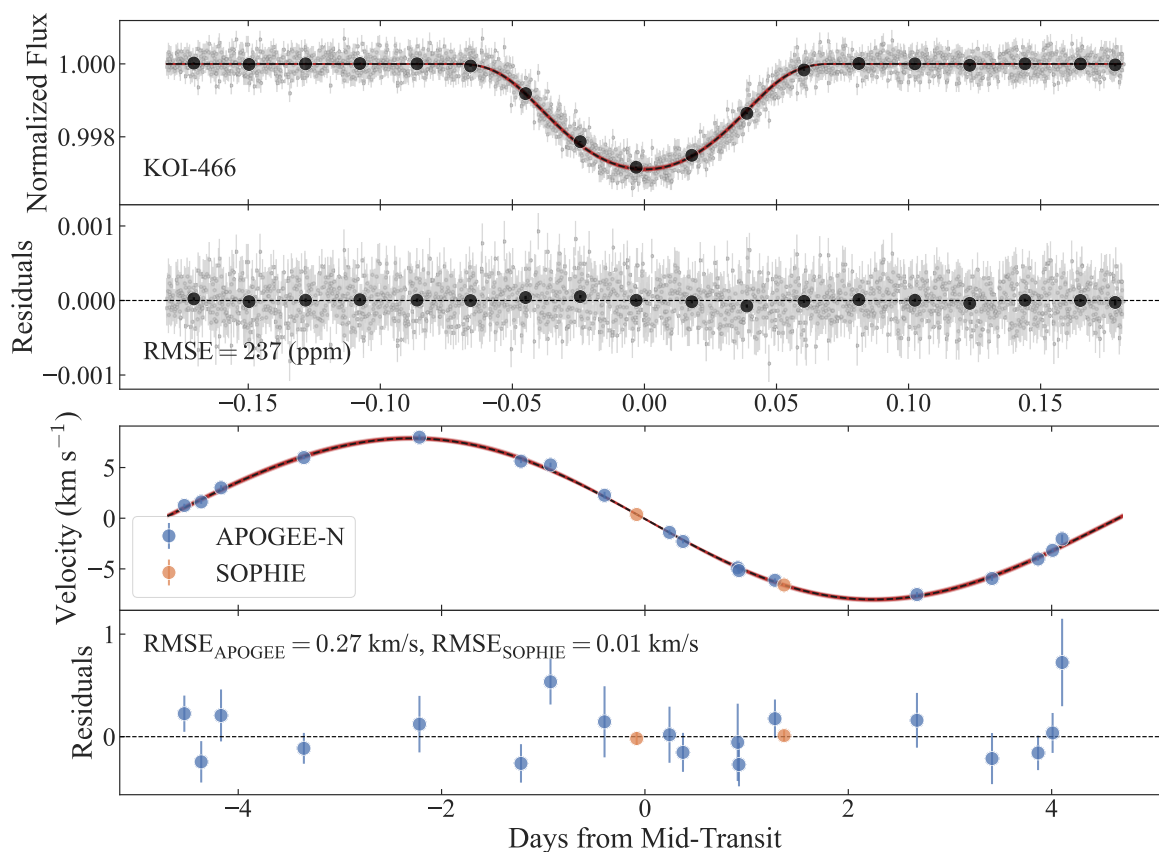


Fig. Set 2.10 – KOI-466. Top. The Kepler photometry for KOI-466 after phase-folding to the derived ephemeris. The large circles represent 30 min bins of the raw data. **Bottom.** The RVs after removing instrumental offsets and phase-folding the data to the derived ephemeris. In each panel, the 1σ (darkest), 2σ , and 3σ (brightest) extent of the models are shown for reference.

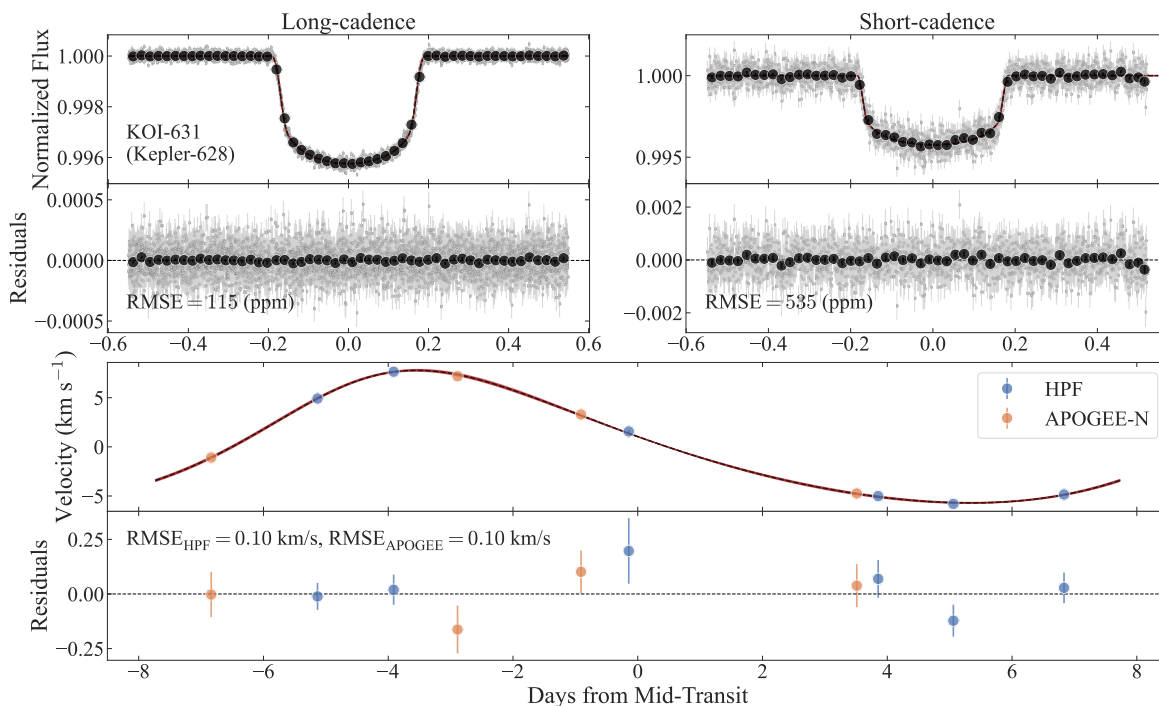


Fig. Set 2.11 – KOI-631. Top. The long-cadence (left) and short-cadence (right) Kepler photometry for KOI-631 after phase-folding to the derived ephemeris. The large circles represent 30 min bins of the raw data. **Bottom.** The RVs after removing instrumental offsets and phase-folding the data to the derived ephemeris. In each panel, the 1σ (darkest), 2σ , and 3σ (brightest) extent of the models are shown for reference.

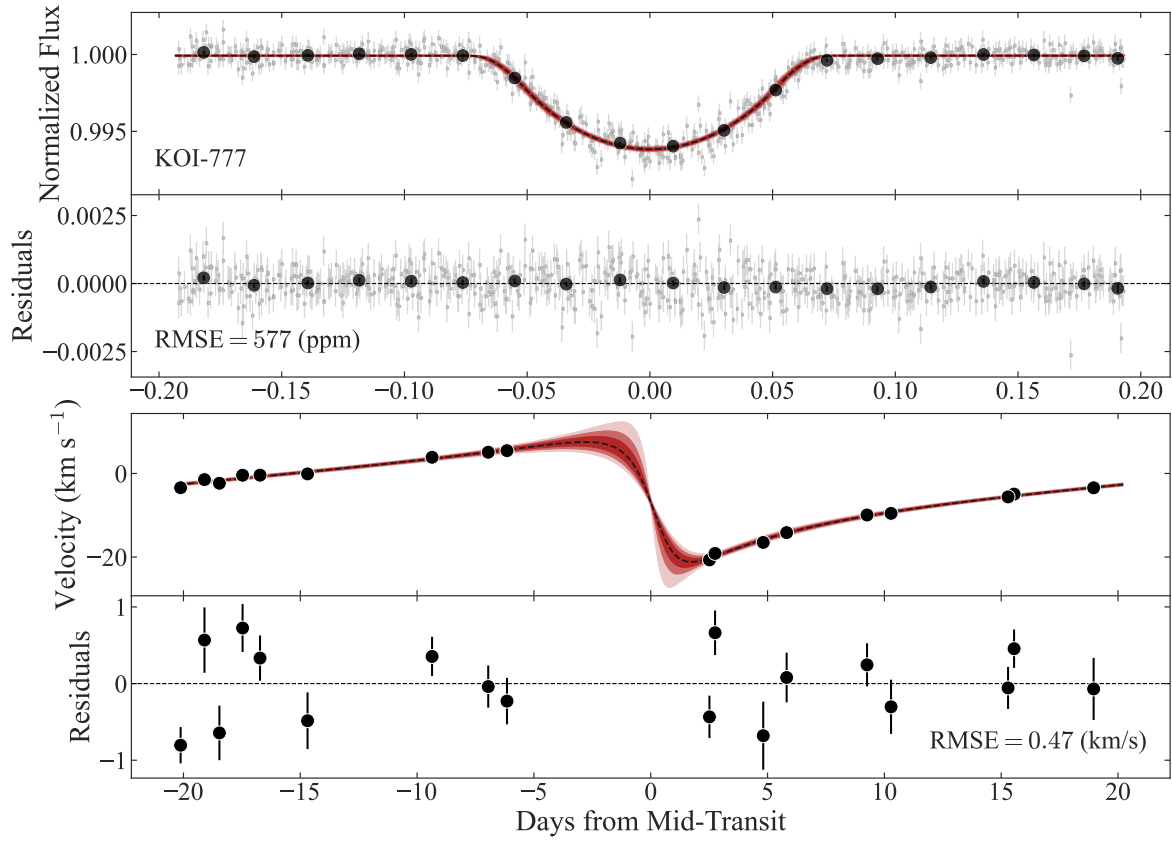


Fig. Set 2.12 – KOI-777. Top. The Kepler photometry for KOI-777 after phase-folding to the derived ephemeris. The large circles represent 30 min bins of the raw data. **Bottom.** The RVs after phase-folding the data to the derived ephemeris. In each panel, the 1σ (darkest), 2σ , and 3σ (brightest) extent of the models are shown for reference.

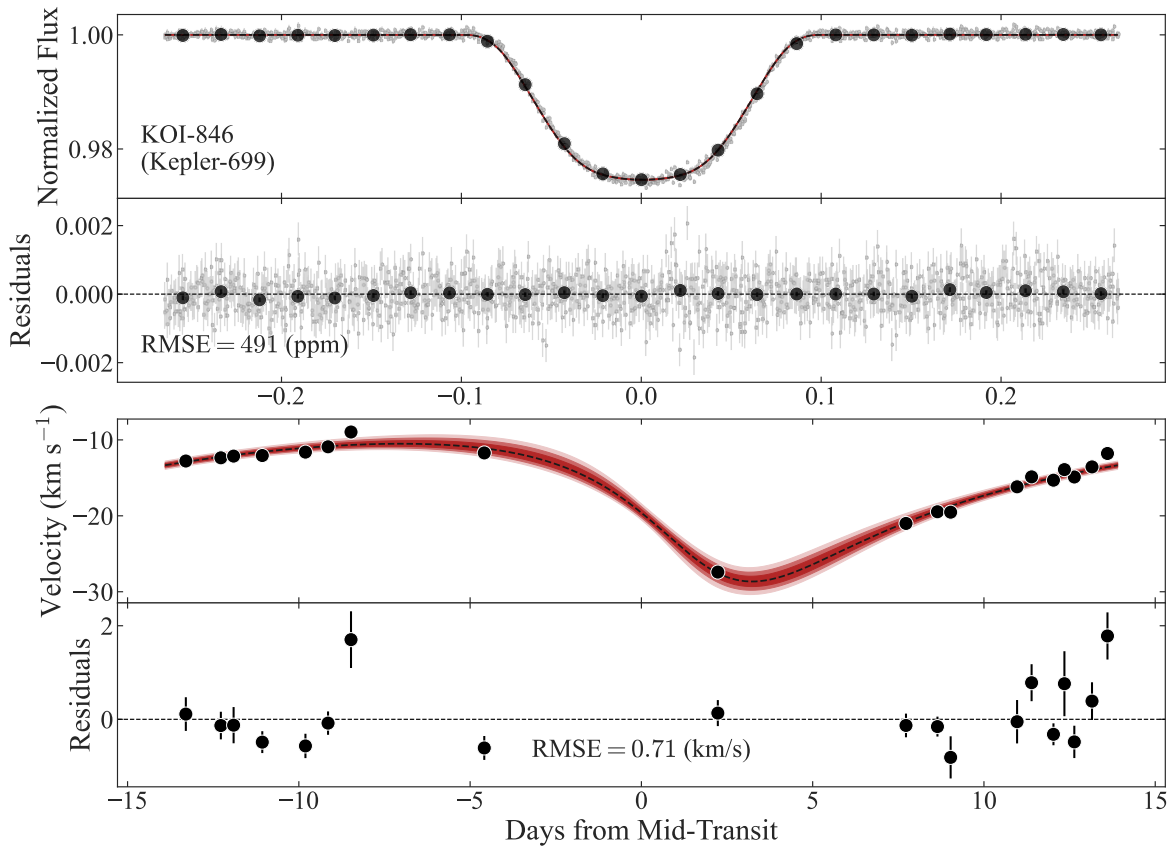


Fig. Set 2.13 – KOI-846. Top. The Kepler photometry for KOI-846 after phase-folding to the derived ephemeris. The large circles represent 30 min bins of the raw data. **Bottom.** The RVs after phase-folding the data to the derived ephemeris. In each panel, the 1σ (darkest), 2σ , and 3σ (brightest) extent of the models are shown for reference.

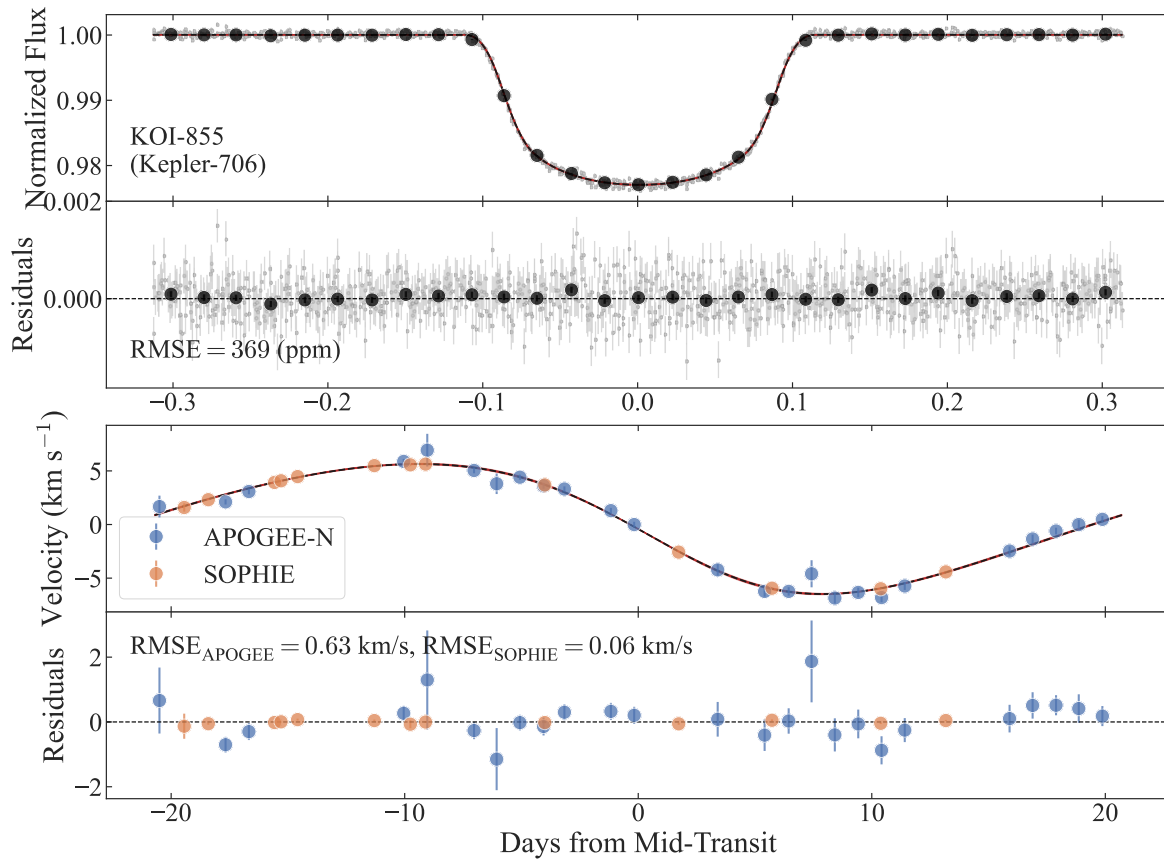


Fig. Set 2.14 – KOI-855. Top. The Kepler photometry for KOI-855 after phase-folding to the derived ephemeris. The large circles represent 30 min bins of the raw data. **Bottom.** The RVs after removing instrumental offsets and phase-folding the data to the derived ephemeris. In each panel, the 1σ (darkest), 2σ , and 3σ (brightest) extent of the models are shown for reference.

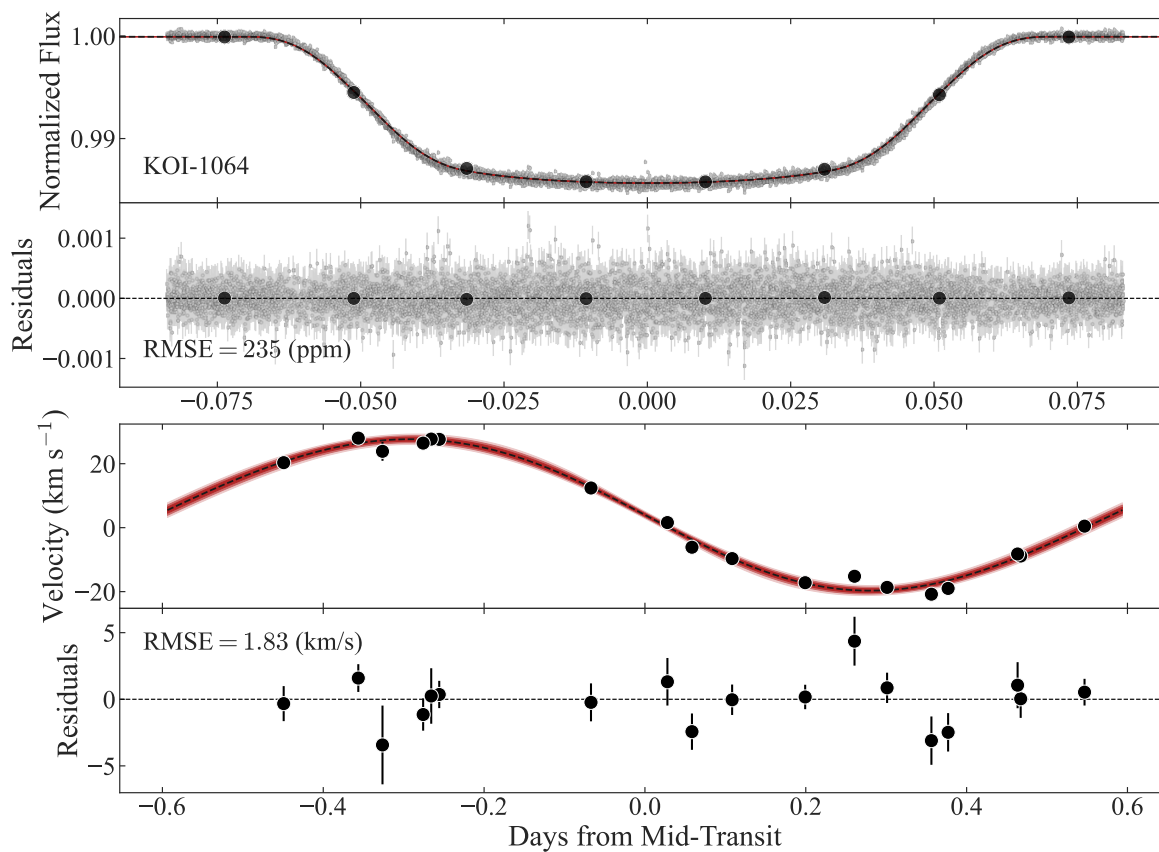


Fig. Set 2.15 – KOI-1064. Top. The Kepler photometry for KOI-1064 after phase-folding to the derived ephemeris. The large circles represent 30 min bins of the raw data. **Bottom.** The RVs after phase-folding the data to the derived ephemeris. In each panel, the 1σ (darkest), 2σ , and 3σ (brightest) extent of the models are shown for reference.

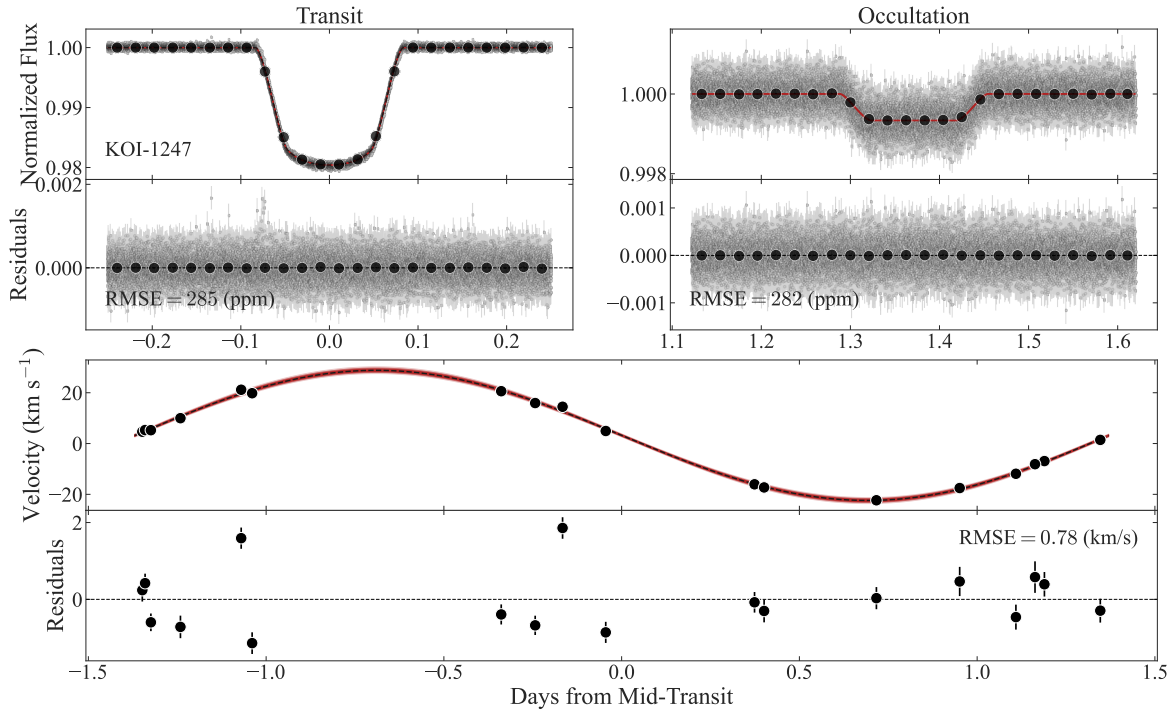


Fig. Set 2.16 – KOI-1247. **Top.** The Kepler photometry center on the transit (left) and occultation (right) for KOI-1247 after phase-folding to the derived ephemeris. The large circles represent 30 min bins of the raw data. **Bottom.** The RVs after phase-folding the data to the derived ephemeris. In each panel, the 1σ (darkest), 2σ , and 3σ (brightest) extent of the models are shown for reference.

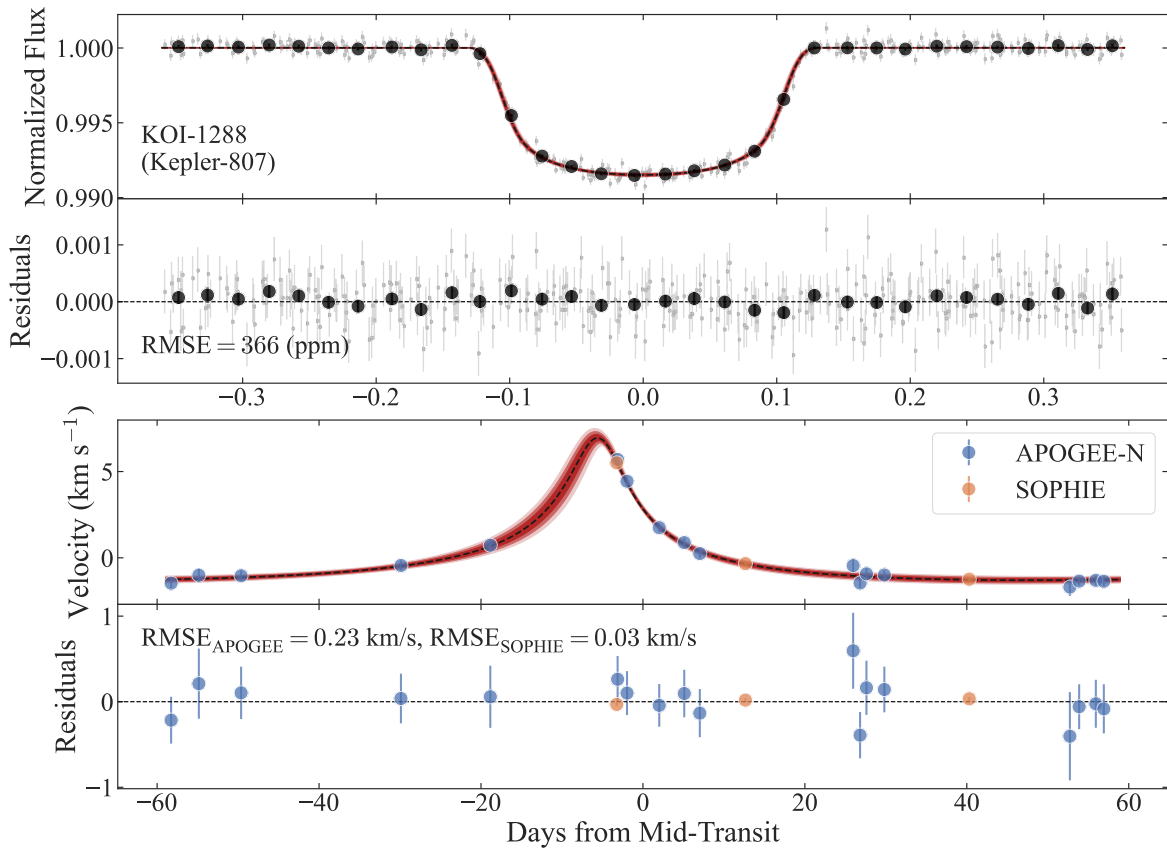


Fig. Set 2.17 – KOI-1288. **Top.** The Kepler photometry for KOI-1288 after phase-folding to the derived ephemeris. The large circles represent 30 min bins of the raw data. **Bottom.** The RVs after removing instrumental offsets and phase-folding the data to the derived ephemeris. In each panel, the 1σ (darkest), 2σ , and 3σ (brightest) extent of the models are shown for reference.

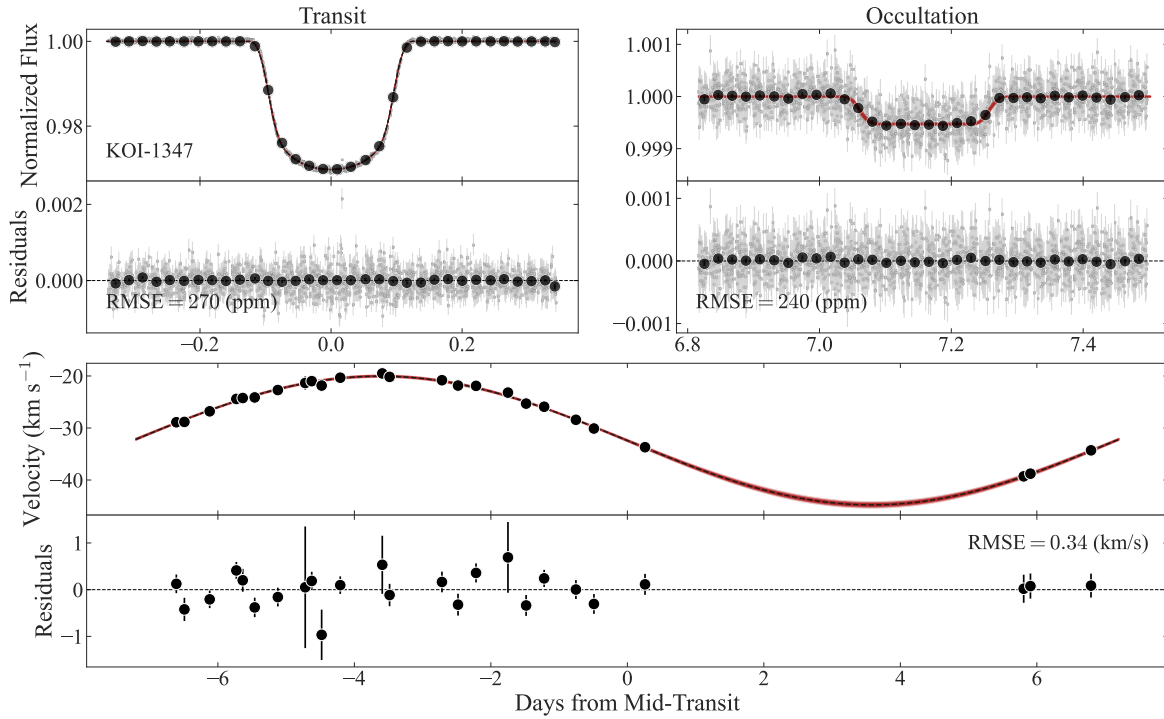


Fig. Set 2.18 – KOI-1347. **Top.** The Kepler photometry center on the transit (left) and occultation (right) for KOI-1347 after phase-folding to the derived ephemeris. The large circles represent 30 min bins of the raw data. **Bottom.** The RVs after phase-folding the data to the derived ephemeris. In each panel, the 1σ (darkest), 2σ , and 3σ (brightest) extent of the models are shown for reference.

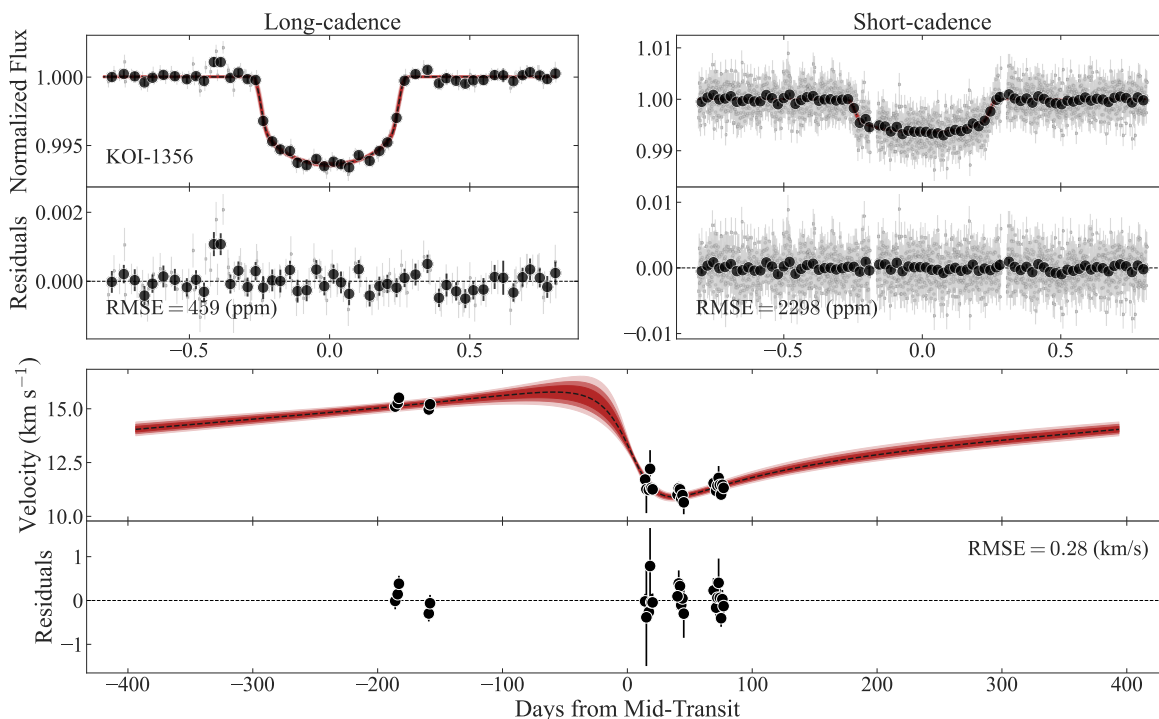


Fig. Set 2.19 – KOI-1356. Top. The long-cadence (left) and short-cadence (right) Kepler photometry for KOI-1356 after phase-folding to the derived ephemeris. The large circles represent 30 min bins of the raw data. **Bottom.** The RVs after phase-folding the data to the derived ephemeris. In each panel, the 1σ (darkest), 2σ , and 3σ (brightest) extent of the models are shown for reference.

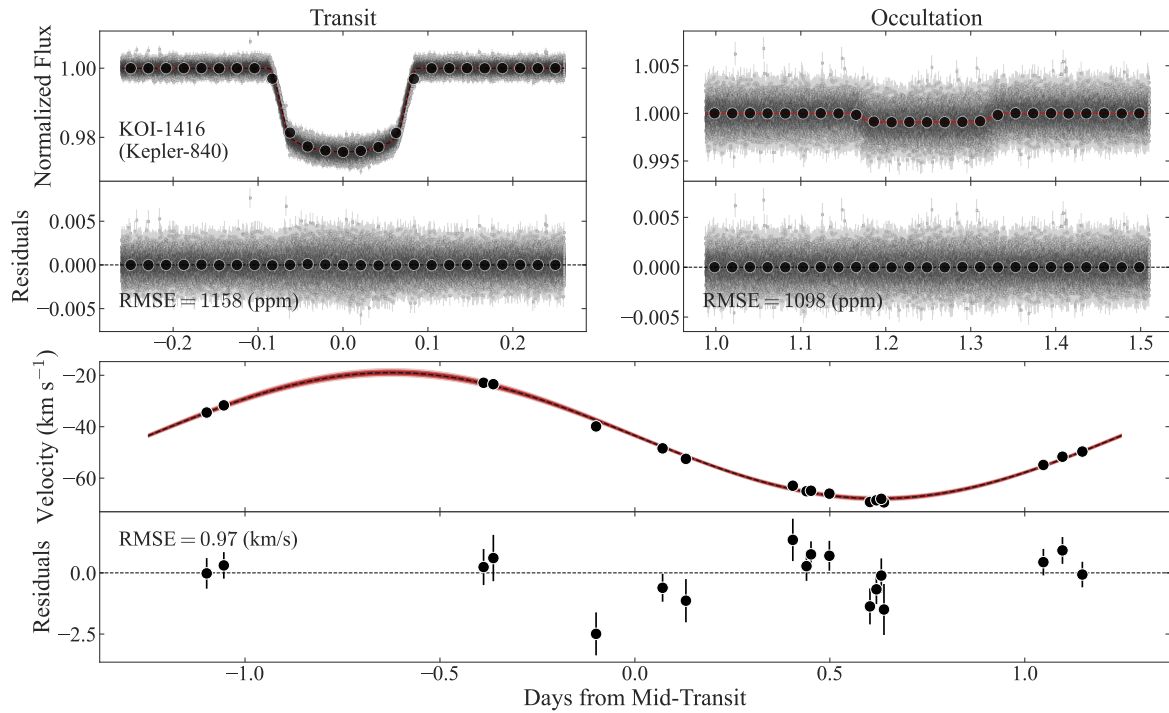


Fig. Set 2.20 – KOI-1416. **Top.** The Kepler photometry center on the transit (left) and occultation (right) for KOI-1416 after phase-folding to the derived ephemeris. The large circles represent 30 min bins of the raw data. **Bottom.** The RVs after phase-folding the data to the derived ephemeris. In each panel, the 1σ (darkest), 2σ , and 3σ (brightest) extent of the models are shown for reference.

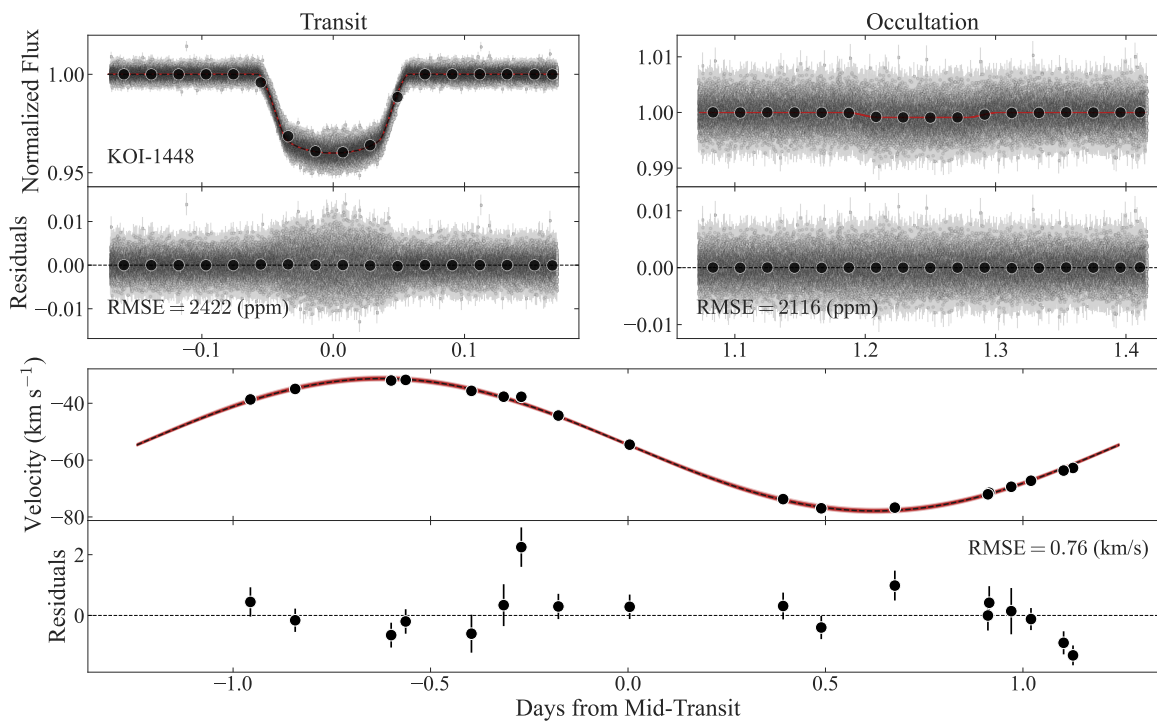


Fig. Set 2.21 – KOI-1448. **Top.** The Kepler photometry center on the transit (left) and occultation (right) for KOI-1448 after phase-folding to the derived ephemeris. The large circles represent 30 min bins of the raw data. **Bottom.** The RVs after phase-folding the data to the derived ephemeris. In each panel, the 1σ (darkest), 2σ , and 3σ (brightest) extent of the models are shown for reference.

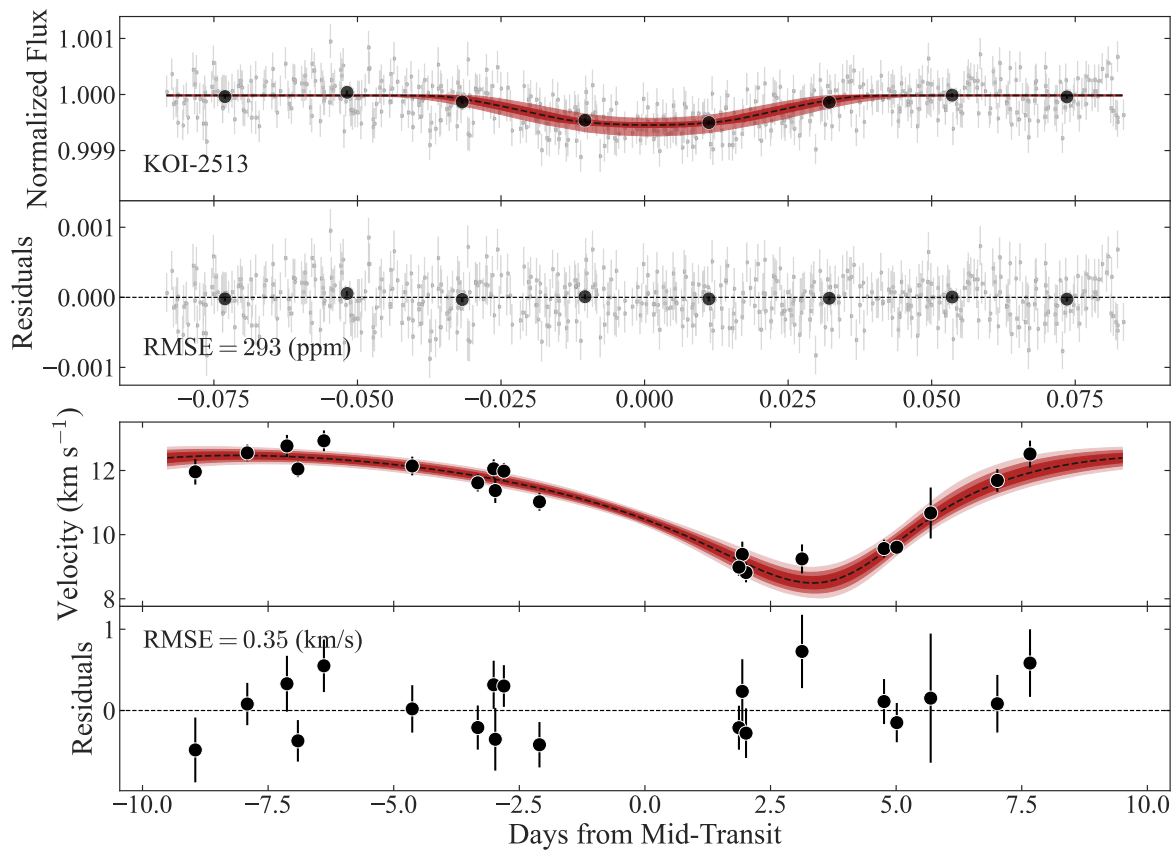


Fig. Set 2.22 – KOI-2513. Top. The Kepler photometry for KOI-2513 after phase-folding to the derived ephemeris. The large circles represent 30 min bins of the raw data. **Bottom.** The RVs after phase-folding the data to the derived ephemeris. In each panel, the 1σ (darkest), 2σ , and 3σ (brightest) extent of the models are shown for reference.

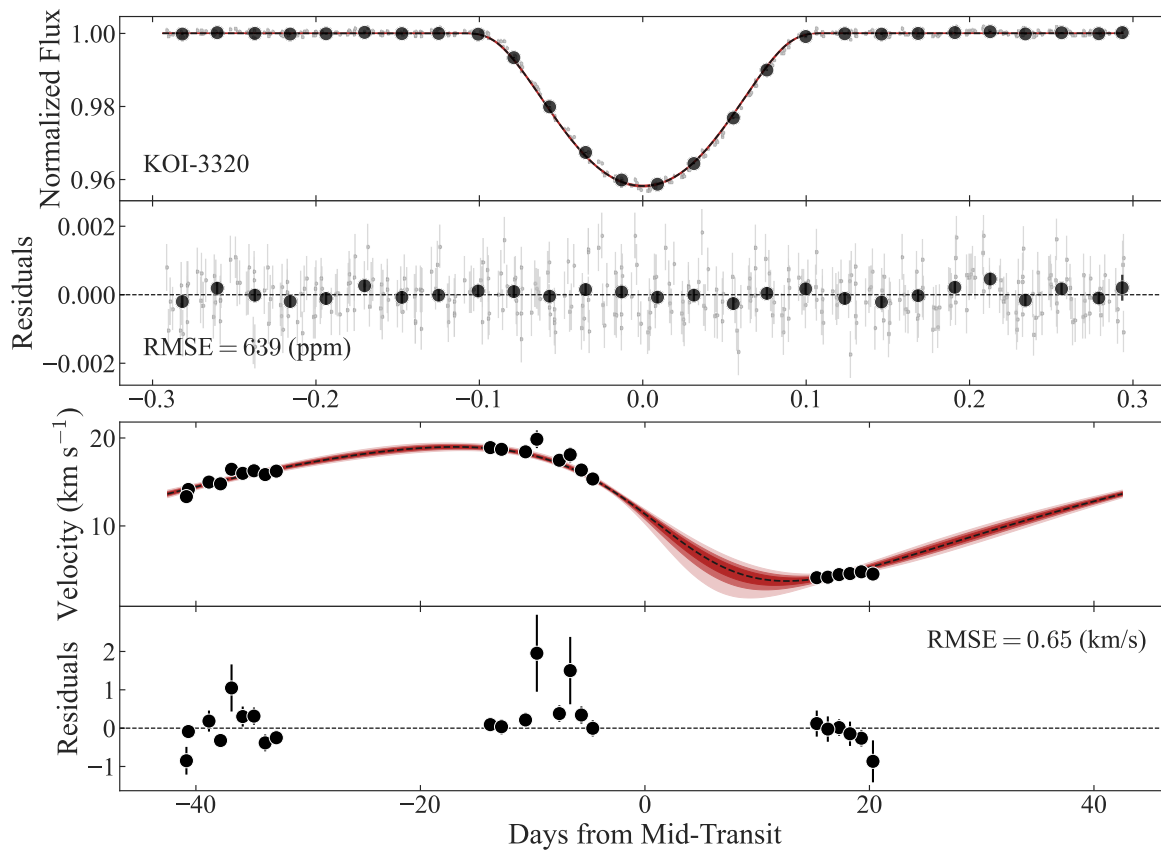


Fig. Set 2.23 – KOI-3320. Top. The Kepler photometry for KOI-3320 after phase-folding to the derived ephemeris. The large circles represent 30 min bins of the raw data. **Bottom.** The RVs after phase-folding the data to the derived ephemeris. In each panel, the 1σ (darkest), 2σ , and 3σ (brightest) extent of the models are shown for reference.

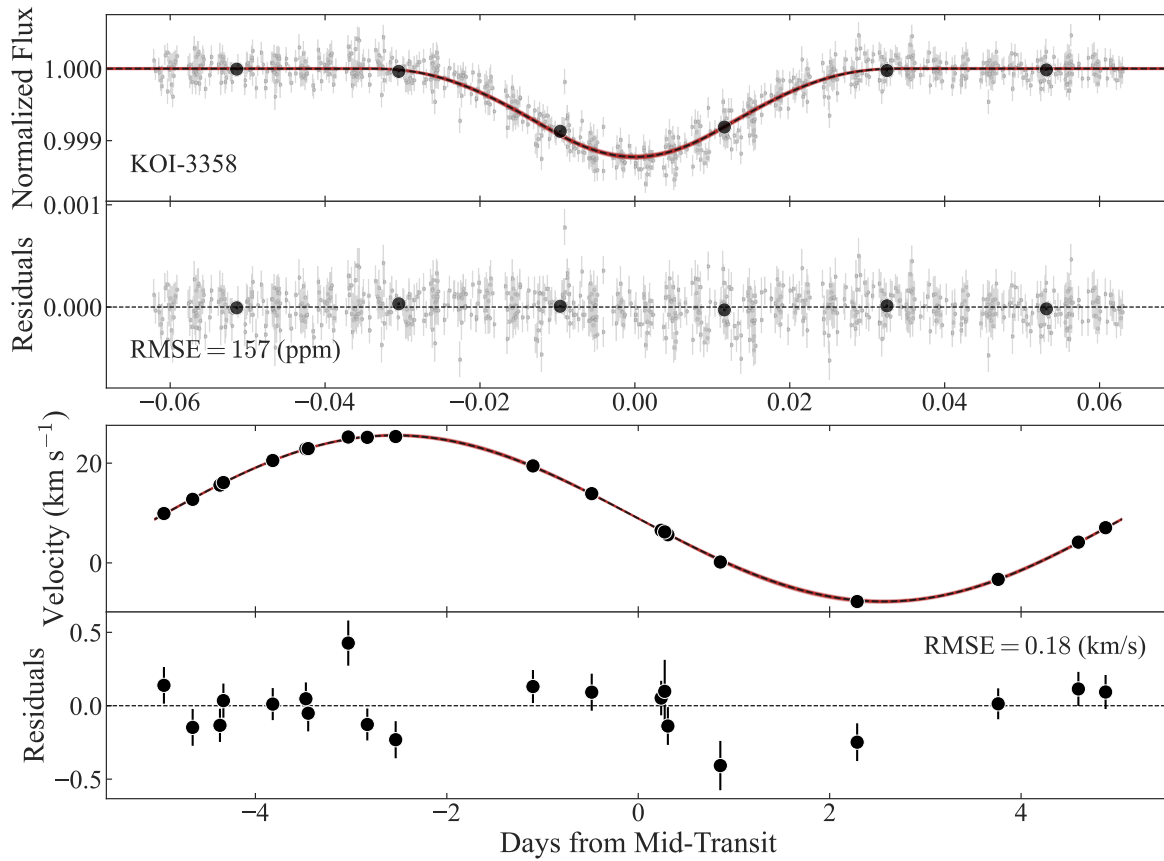


Fig. Set 2.24 – KOI-3358. Top. The Kepler photometry for KOI-3358 after phase-folding to the derived ephemeris. The large circles represent 30 min bins of the raw data. **Bottom.** The RVs after phase-folding the data to the derived ephemeris. In each panel, the 1σ (darkest), 2σ , and 3σ (brightest) extent of the models are shown for reference.

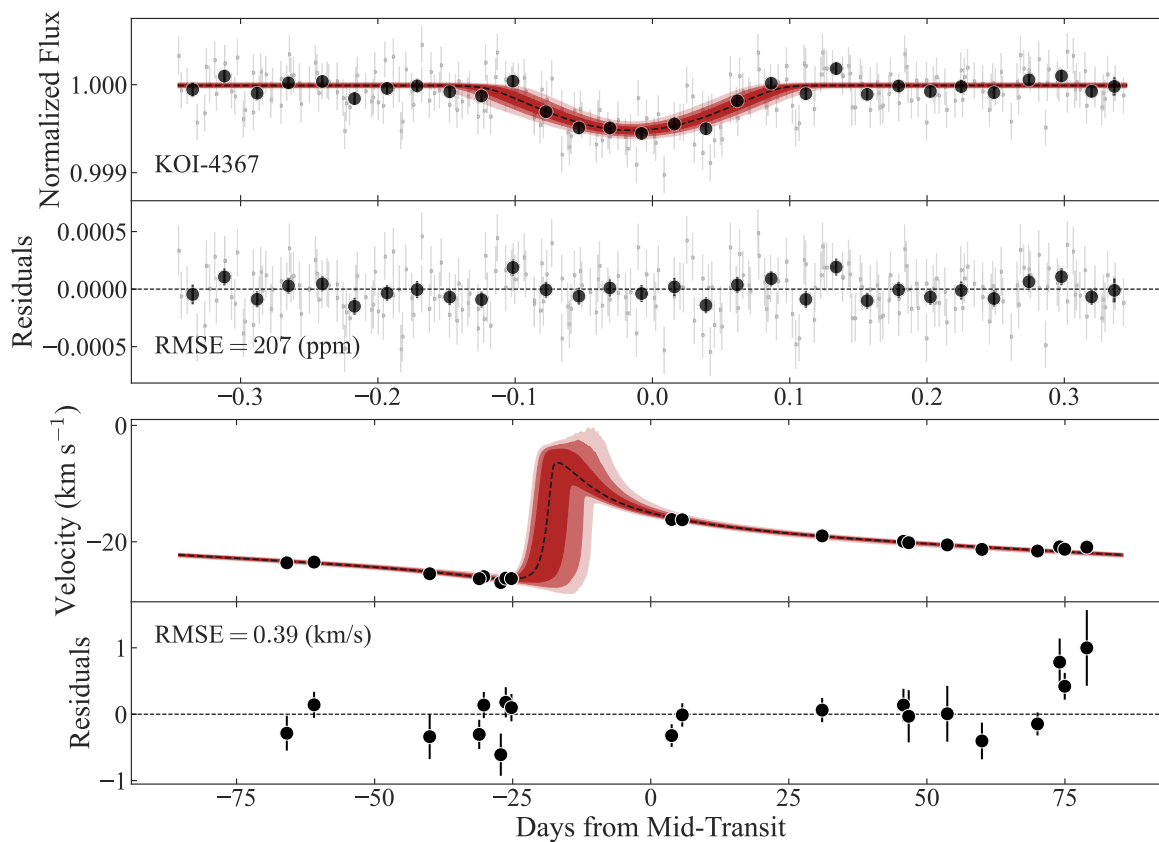


Fig. Set 2.25 – KOI-4367. Top. The Kepler photometry for KOI-4367 after phase-folding to the derived ephemeris. The large circles represent 30 min bins of the raw data. **Bottom.** The RVs after phase-folding the data to the derived ephemeris. In each panel, the 1σ (darkest), 2σ , and 3σ (brightest) extent of the models are shown for reference.

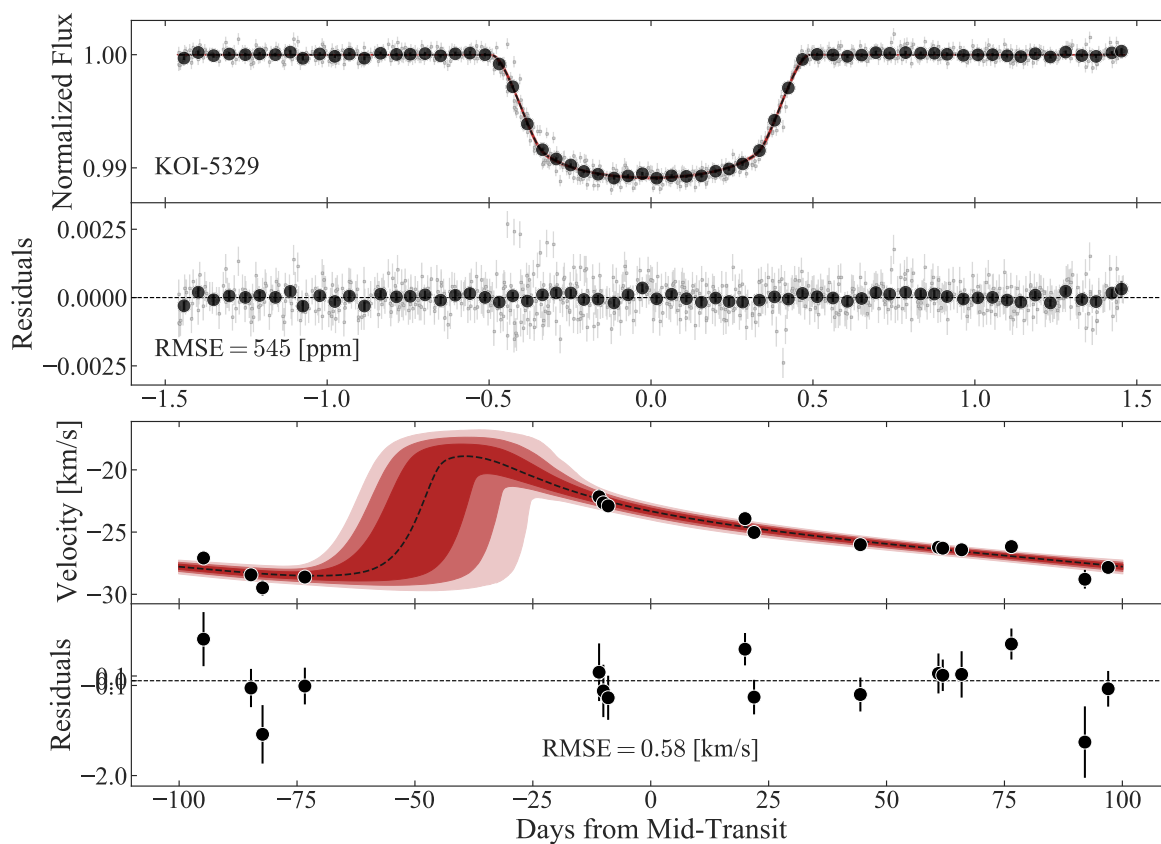


Fig. Set 2.26 – KOI-5329. Top. The Kepler photometry for KOI-5329 after phase-folding to the derived ephemeris. The large circles represent 30 min bins of the raw data. **Bottom.** The RVs after phase-folding the data to the derived ephemeris. In each panel, the 1σ (darkest), 2σ , and 3σ (brightest) extent of the models are shown for reference.

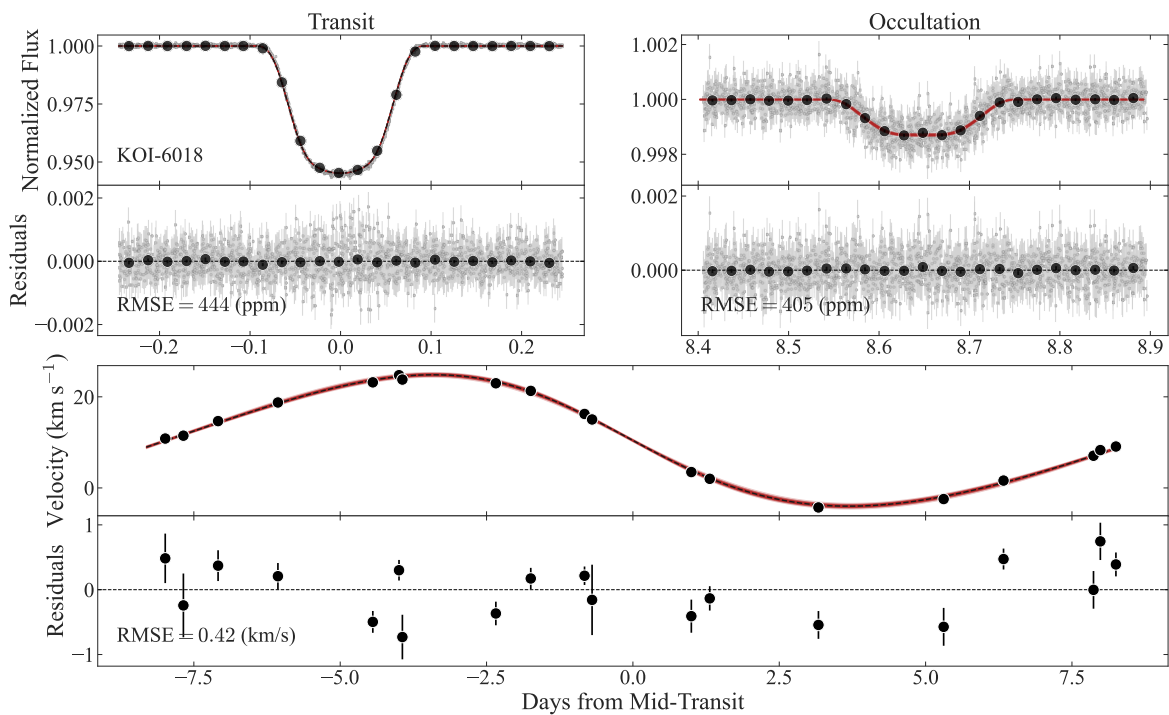


Fig. Set 2.27 – KOI-6018. **Top.** The Kepler photometry center on the transit (left) and occultation (right) for KOI-6018 after phase-folding to the derived ephemeris. The large circles represent 30 min bins of the raw data. **Bottom.** The RVs after phase-folding the data to the derived ephemeris. In each panel, the 1σ (darkest), 2σ , and 3σ (brightest) extent of the models are shown for reference.

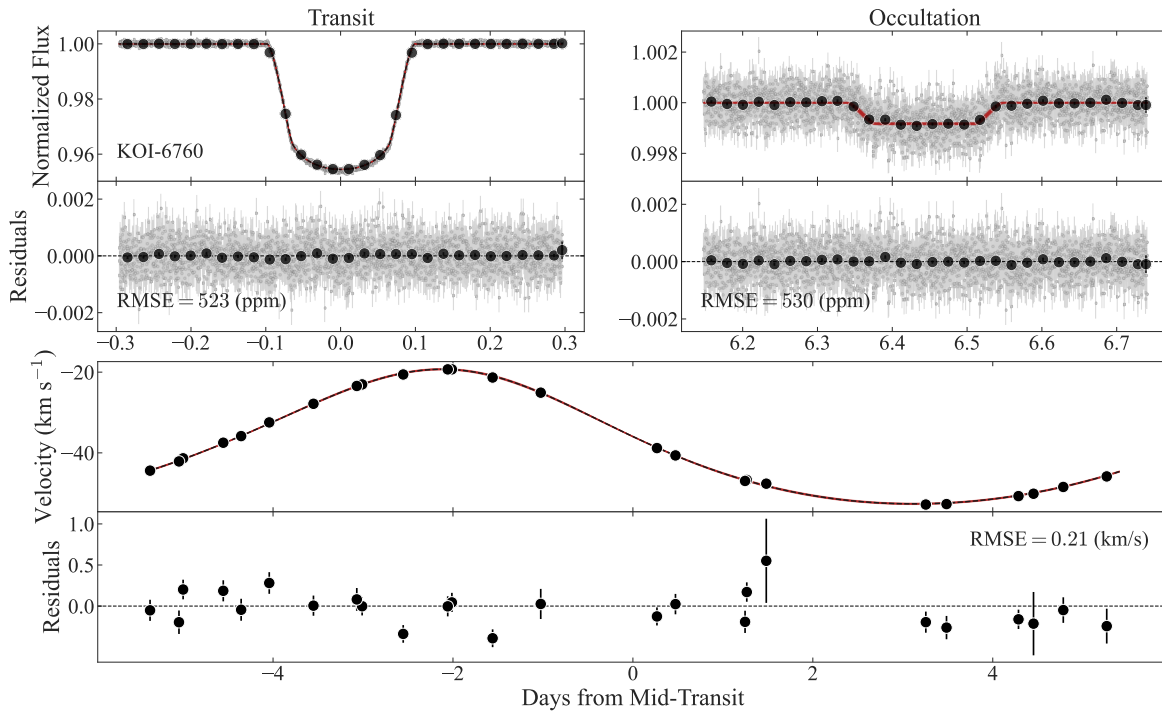


Fig. Set 2.28 – KOI-6760. **Top.** The Kepler photometry center on the transit (left) and occultation (right) for KOI-6760 after phase-folding to the derived ephemeris. The large circles represent 30 min bins of the raw data. **Bottom.** The RVs after phase-folding the data to the derived ephemeris. In each panel, the 1σ (darkest), 2σ , and 3σ (brightest) extent of the models are shown for reference.

Fig. Set7. Photometric variability for the sample of 28 KOIs The ARC2 corrected light curve for the systems analyzed in this work.

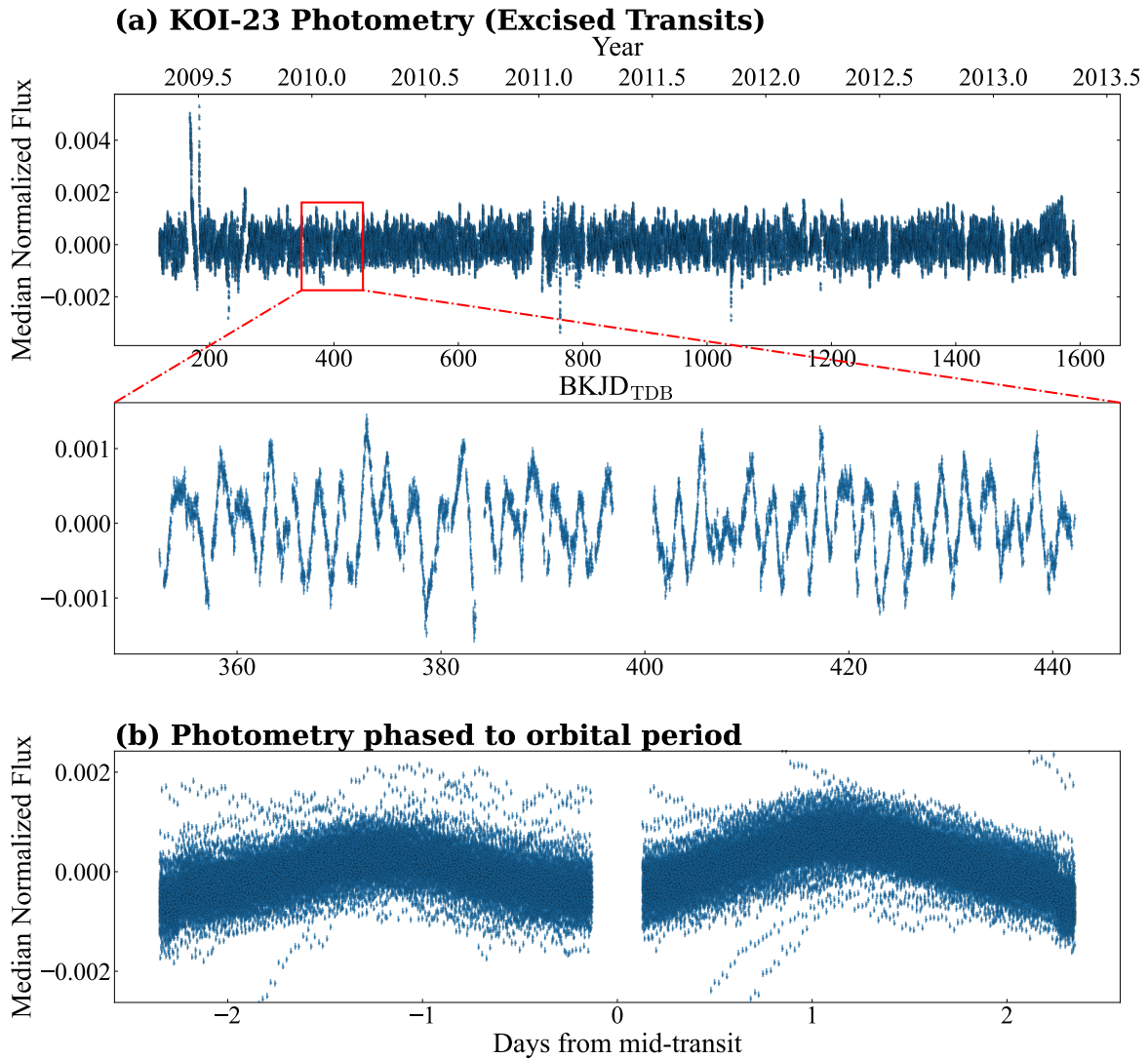


Fig. Set 7.1 – KOI–23. (a) The ARC2 corrected light curve for KOI-23, after excising the transits, with an inset displaying the quarter 2 data. (b) The out-of-transit photometric variability after phasing to the orbital ephemeris. The derived rotation period is identical (within the 1σ uncertainty) to the orbital period.

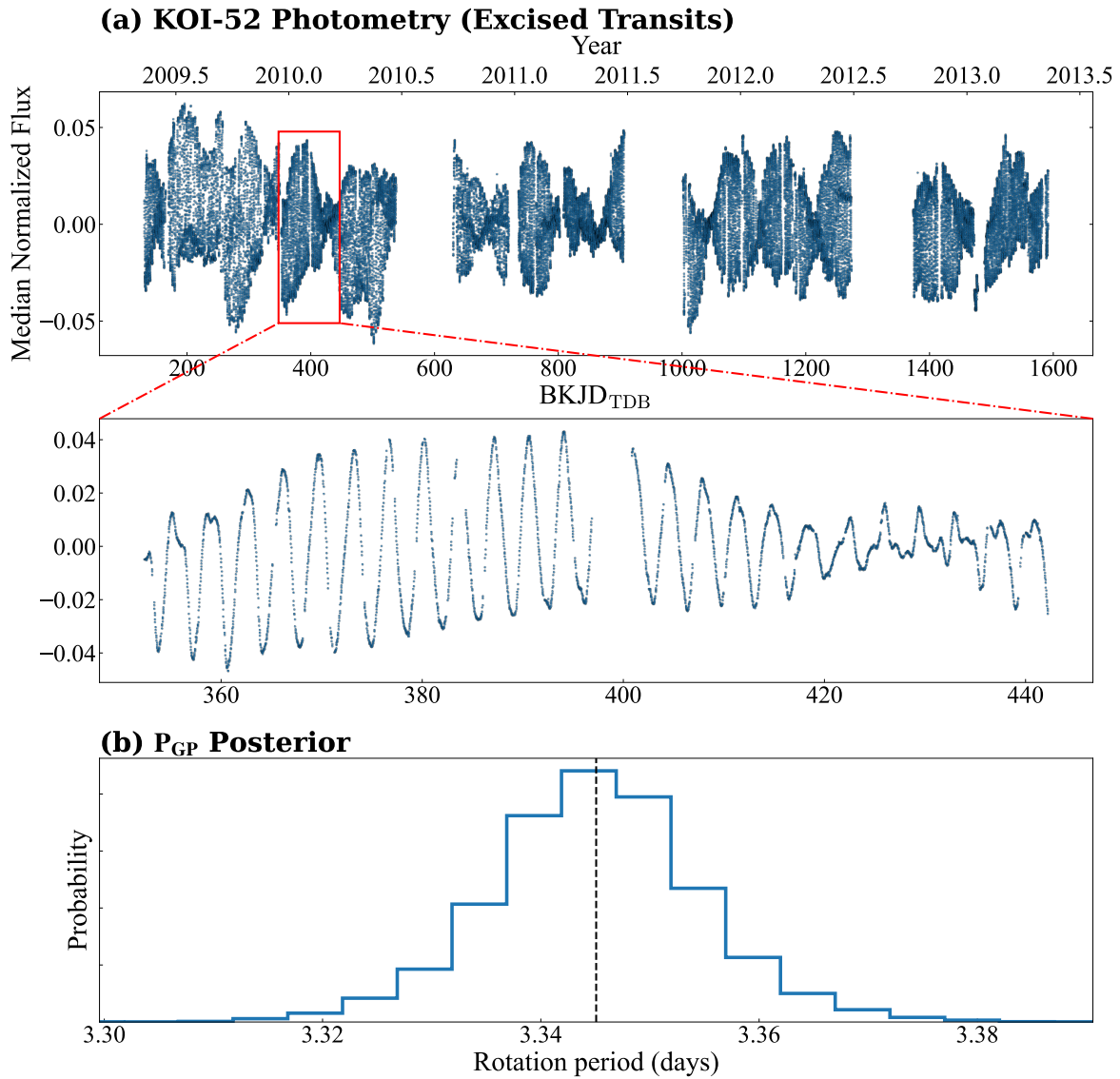


Fig. Set 7.2 – KOI-52. (a) The ARC2 corrected light curve for KOI-52, after excising the transits, with an inset displaying a subset of the Kepler data. (b) The posterior distribution for the Gaussian process period, which we interpret as a measurement of the stellar rotation period.

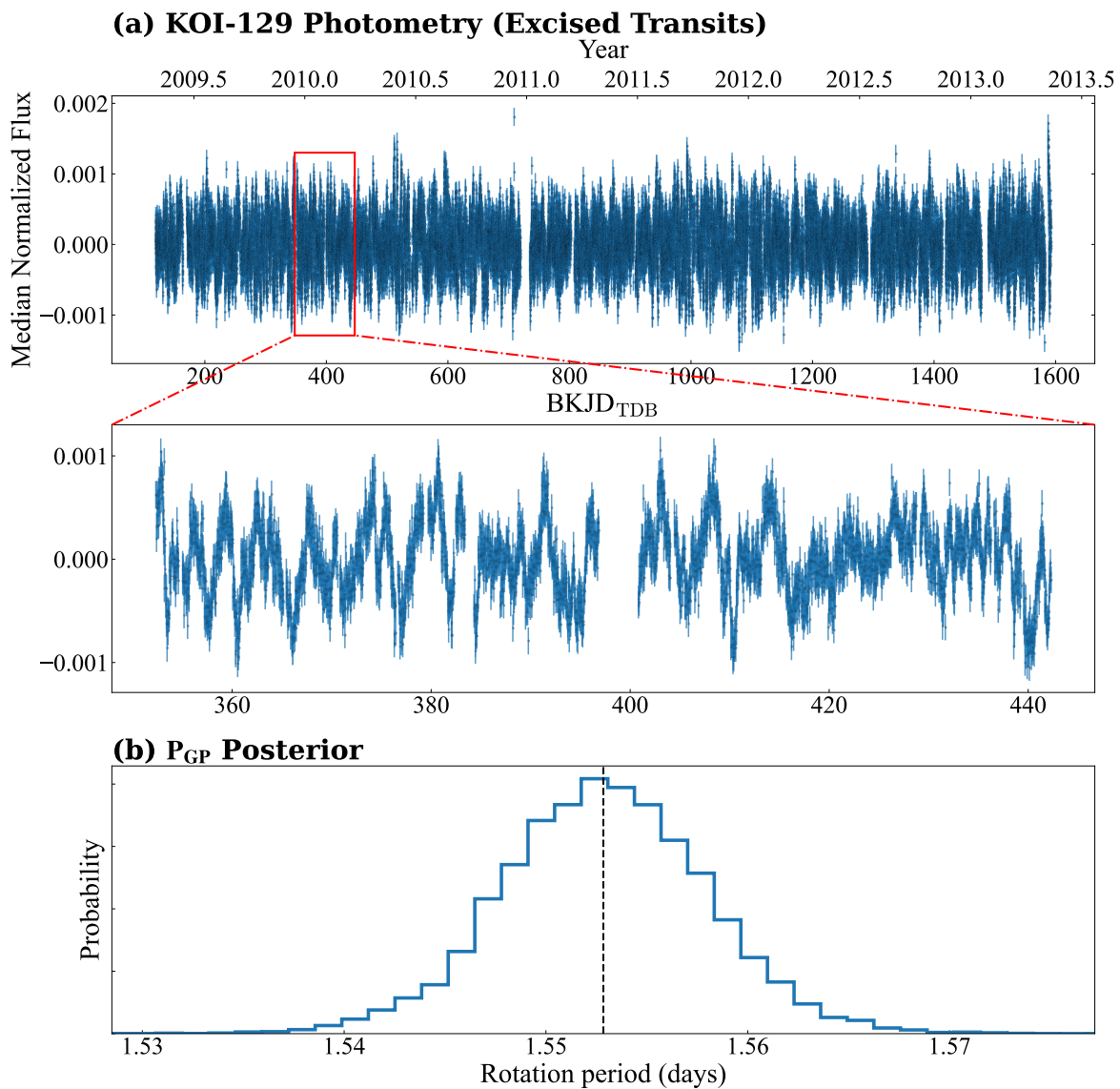


Fig. Set 7.3 – KOI-129. (a) The ARC2 corrected light curve for KOI-129, after excising the transits, with an inset displaying a subset of the Kepler data. (b) The posterior distribution for the Gaussian process period, which we interpret as a measurement of the stellar rotation period.

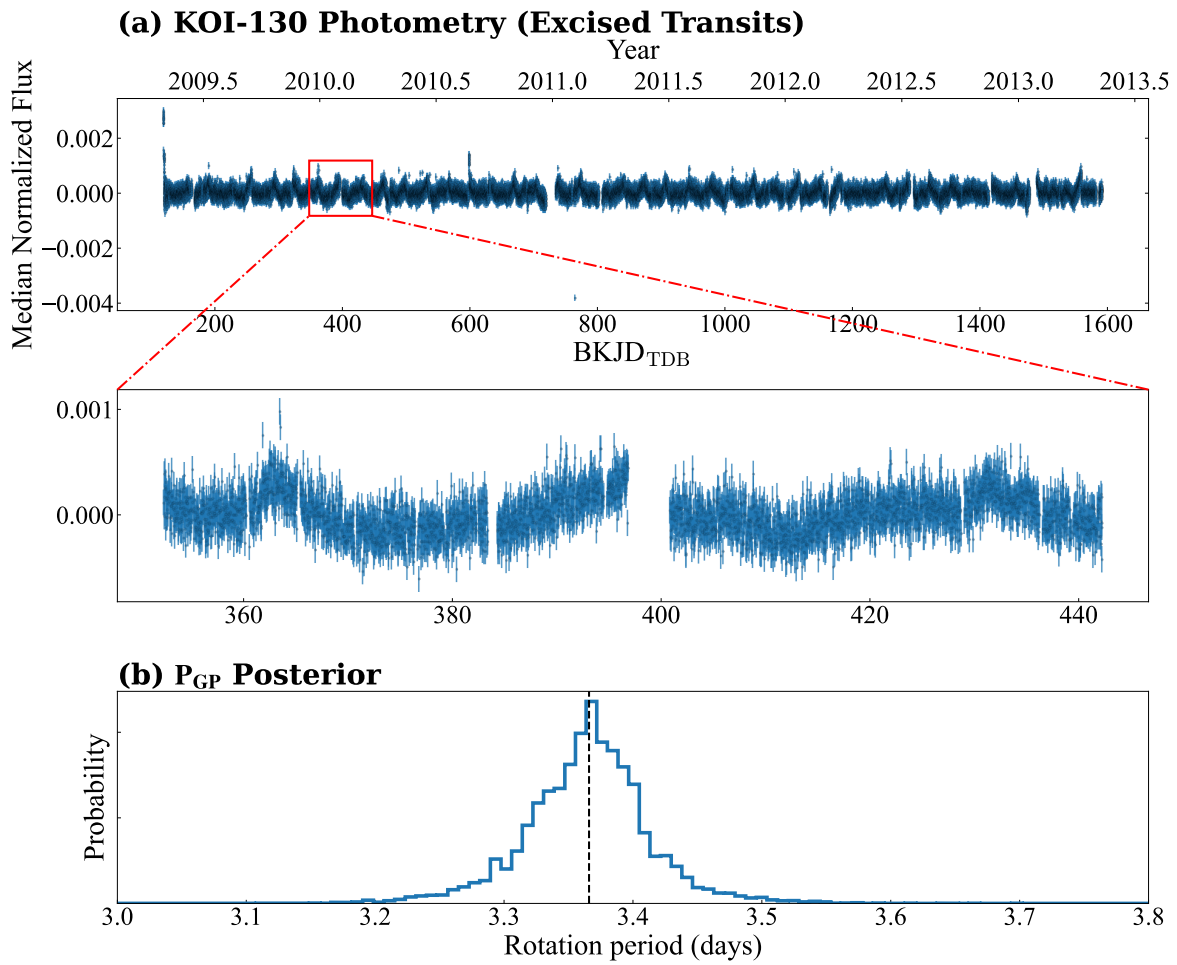


Fig. Set 7.4 – KOI-130. (a) The ARC2 corrected light curve for KOI-130, after excising the transits, with an inset displaying a subset of the Kepler data. (b) The posterior distribution for the Gaussian process period, which we interpret as a measurement of the stellar rotation period.

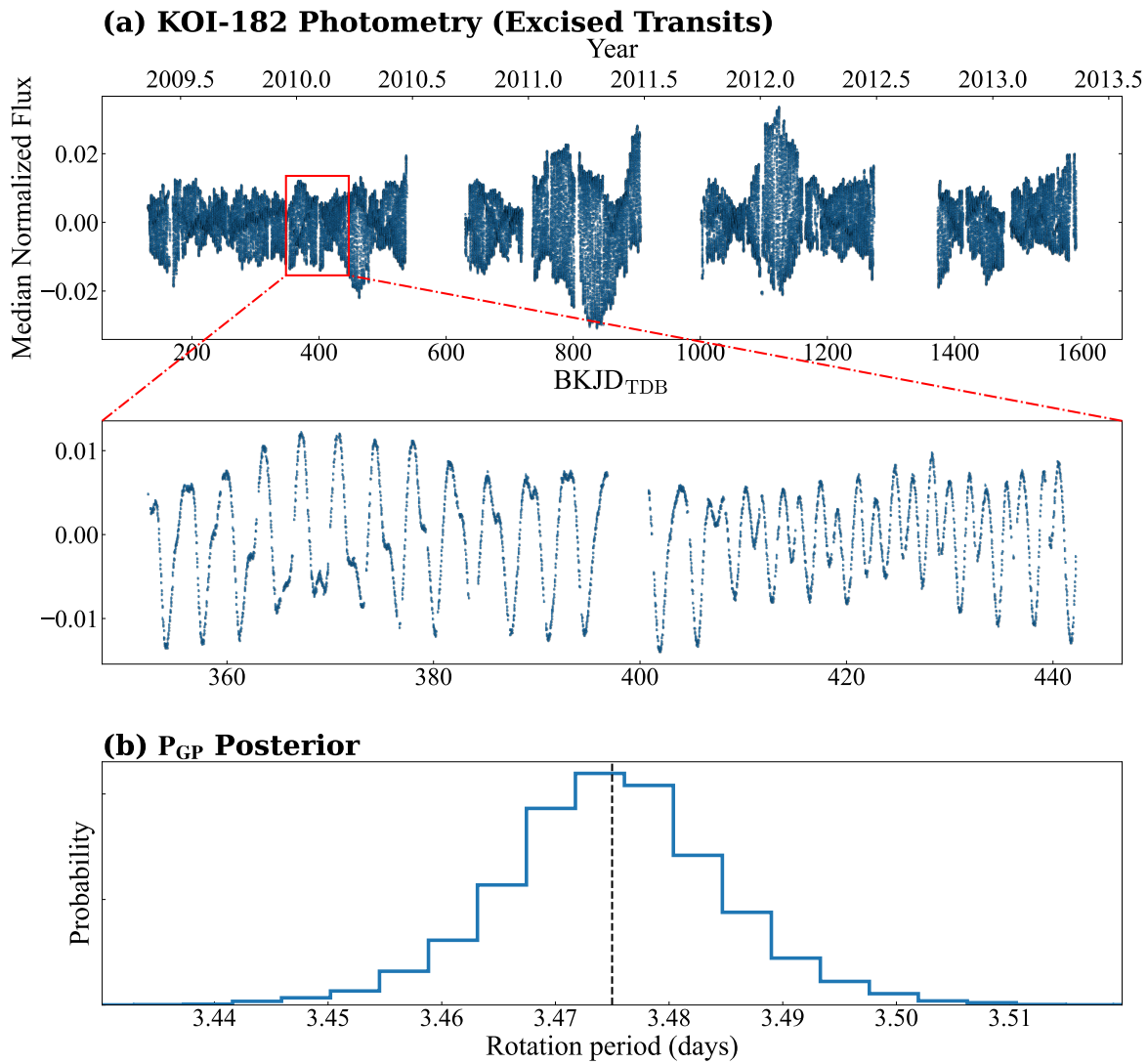


Fig. Set 7.5 – KOI-182. (a) The ARC2 corrected light curve for KOI-182, after excising the transits, with an inset displaying a subset of the Kepler data. (b) The posterior distribution for the Gaussian process period, which we interpret as a measurement of the stellar rotation period.

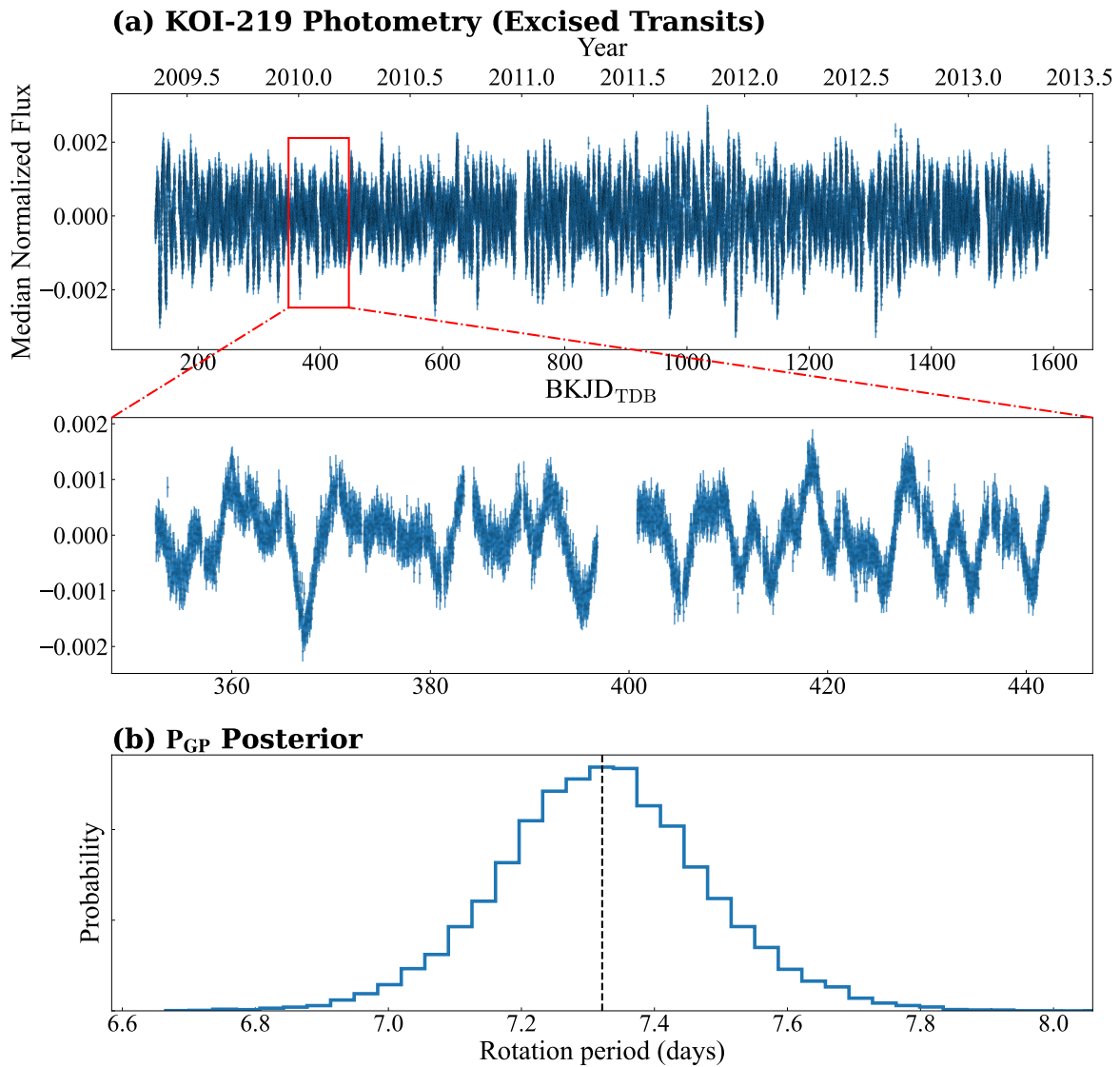


Fig. Set 7.6 – KOI-219. (a) The ARC2 corrected light curve for KOI-219, after excising the transits, with an inset displaying a subset of the Kepler data. (b) The posterior distribution for the Gaussian process period, which we interpret as a measurement of the stellar rotation period.

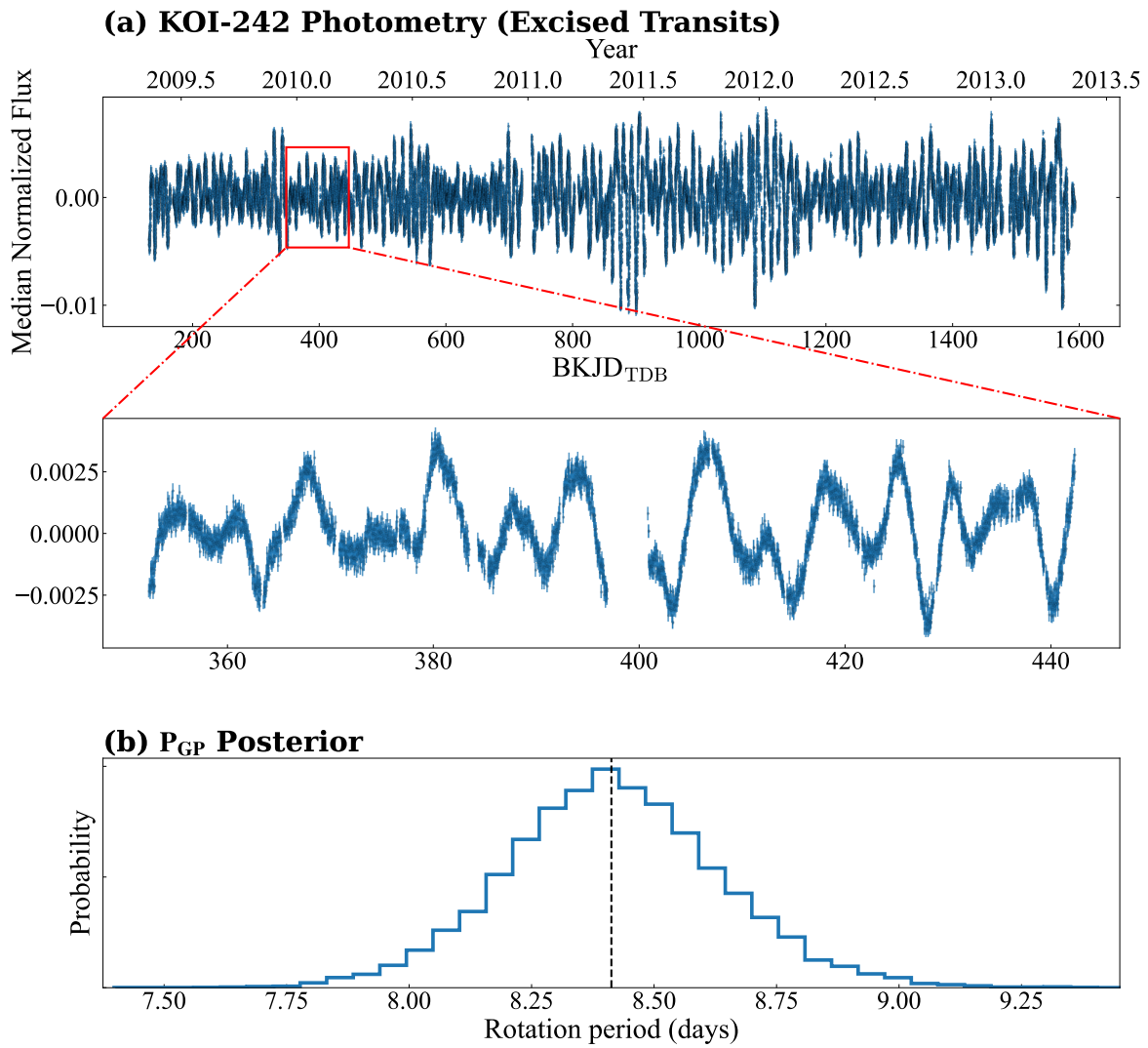


Fig. Set 7.7 – KOI-242. (a) The ARC2 corrected light curve for KOI-242, after excising the transits, with an inset displaying a subset of the Kepler data. (b) The posterior distribution for the Gaussian process period, which we interpret as a measurement of the stellar rotation period.

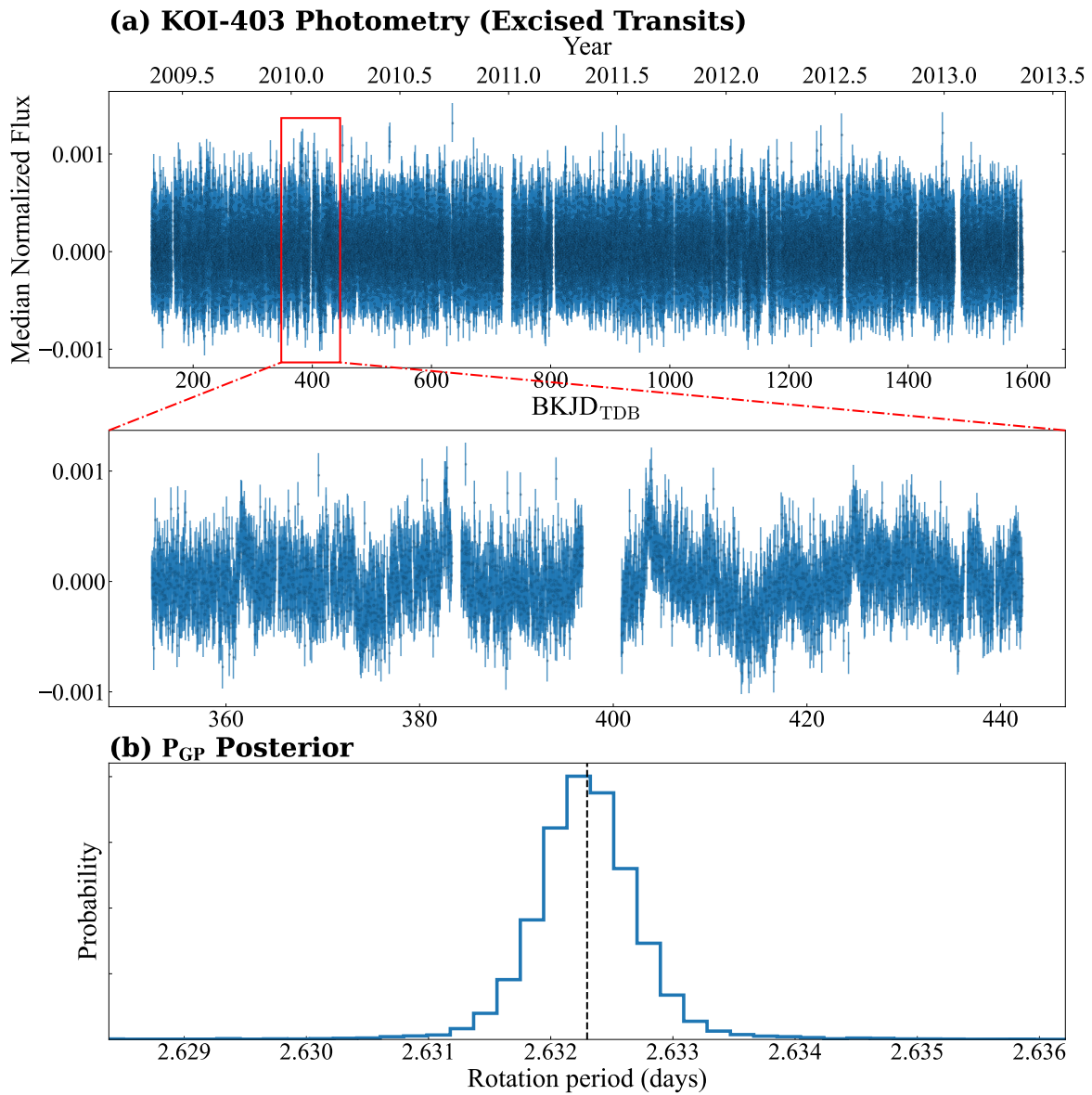


Fig. Set 7.8 – KOI-403. (a) The ARC2 corrected light curve for KOI-403, after excising the transits, with an inset displaying a subset of the Kepler data. (b) The posterior distribution for the Gaussian process period, which we interpret as a measurement of the stellar rotation period.

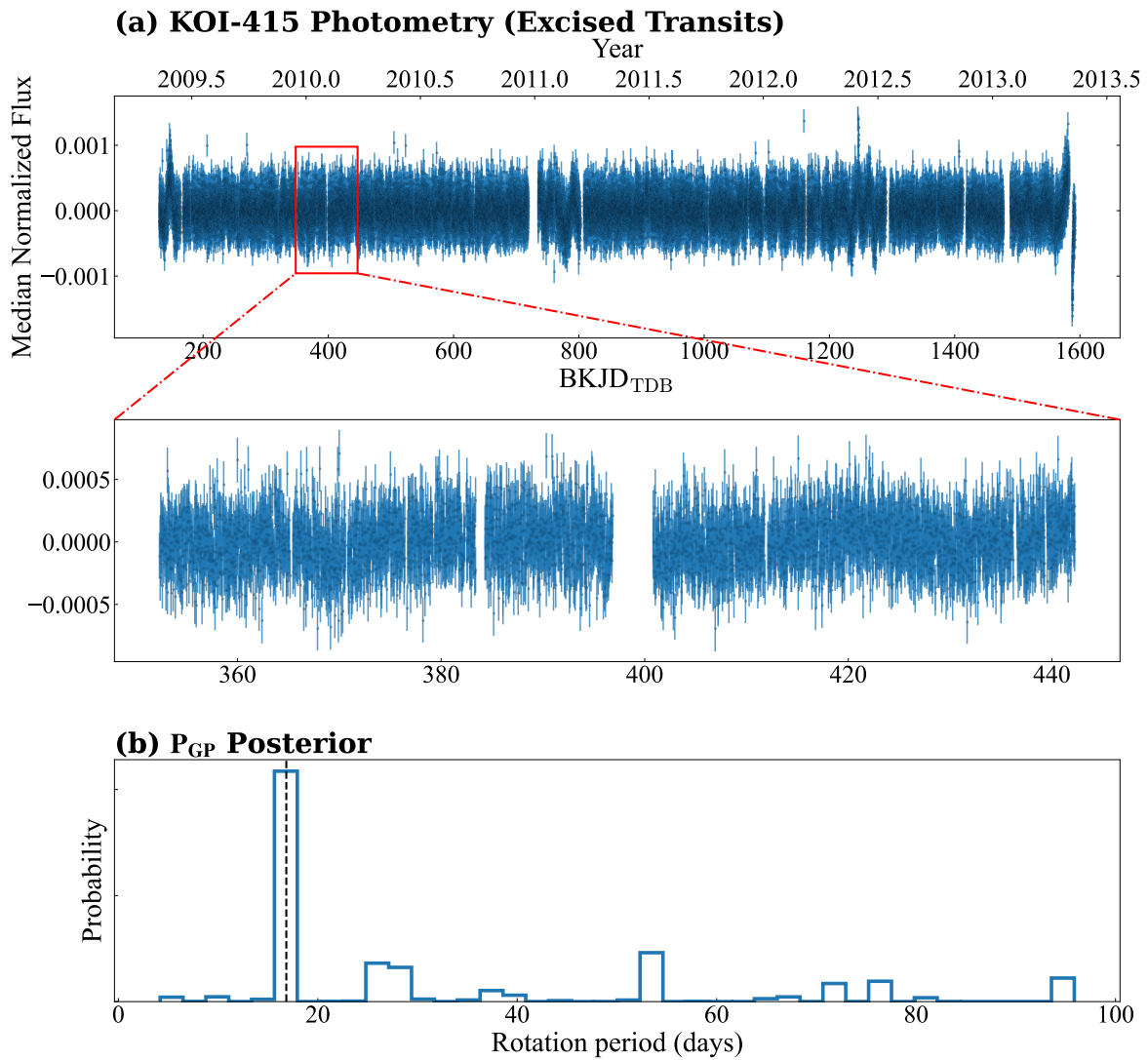


Fig. Set 7.9 – KOI-415. (a) The ARC2 corrected light curve for KOI-415, after excising the transits, with an inset displaying a subset of the Kepler data. (b) The posterior distribution for the Gaussian process period, which we interpret as a measurement of the stellar rotation period.

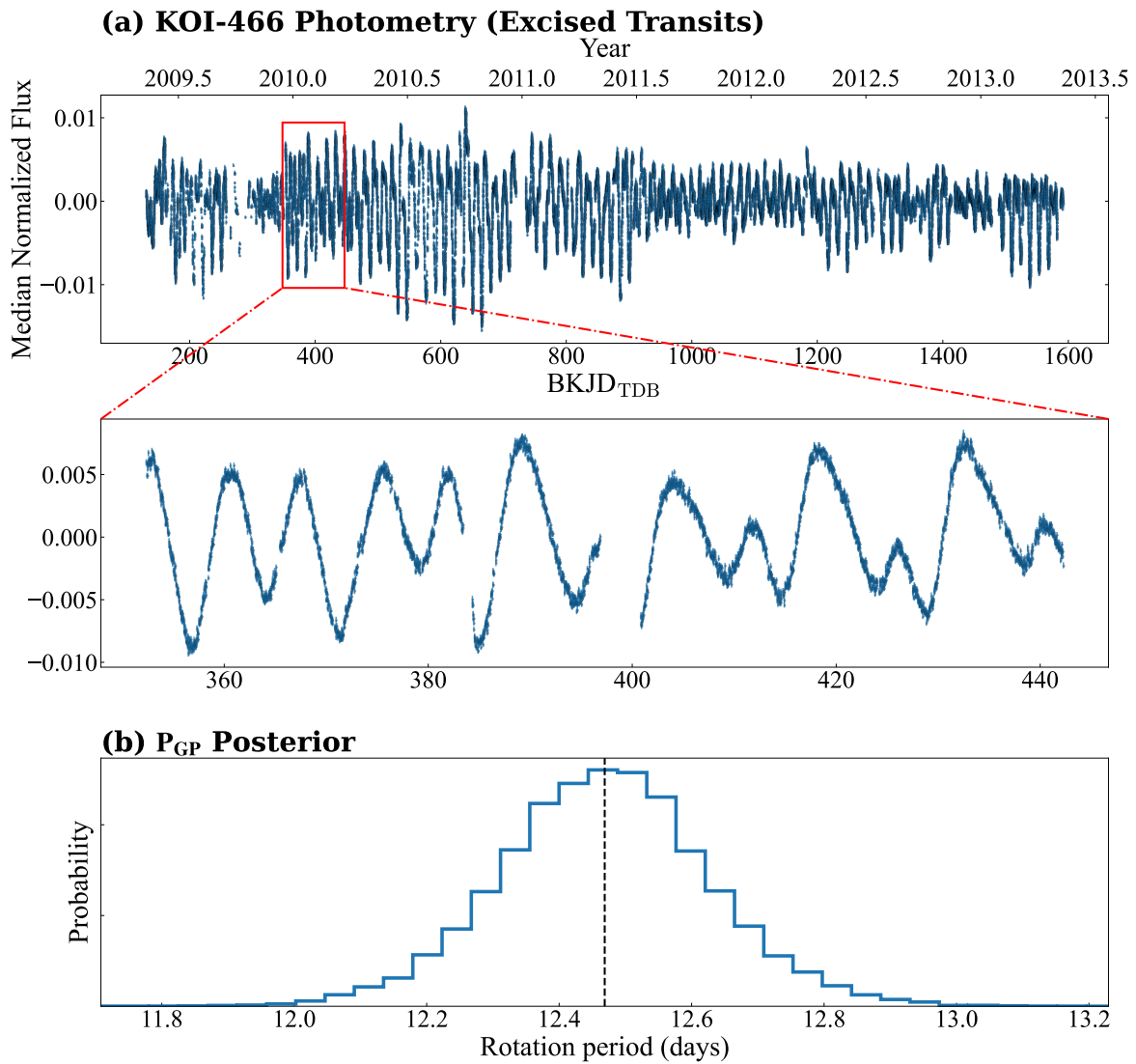


Fig. Set 7.10 – KOI-466. (a) The ARC2 corrected light curve for KOI-466, after excising the transits, with an inset displaying a subset of the Kepler data. (b) The posterior distribution for the Gaussian process period, which we interpret as a measurement of the stellar rotation period.

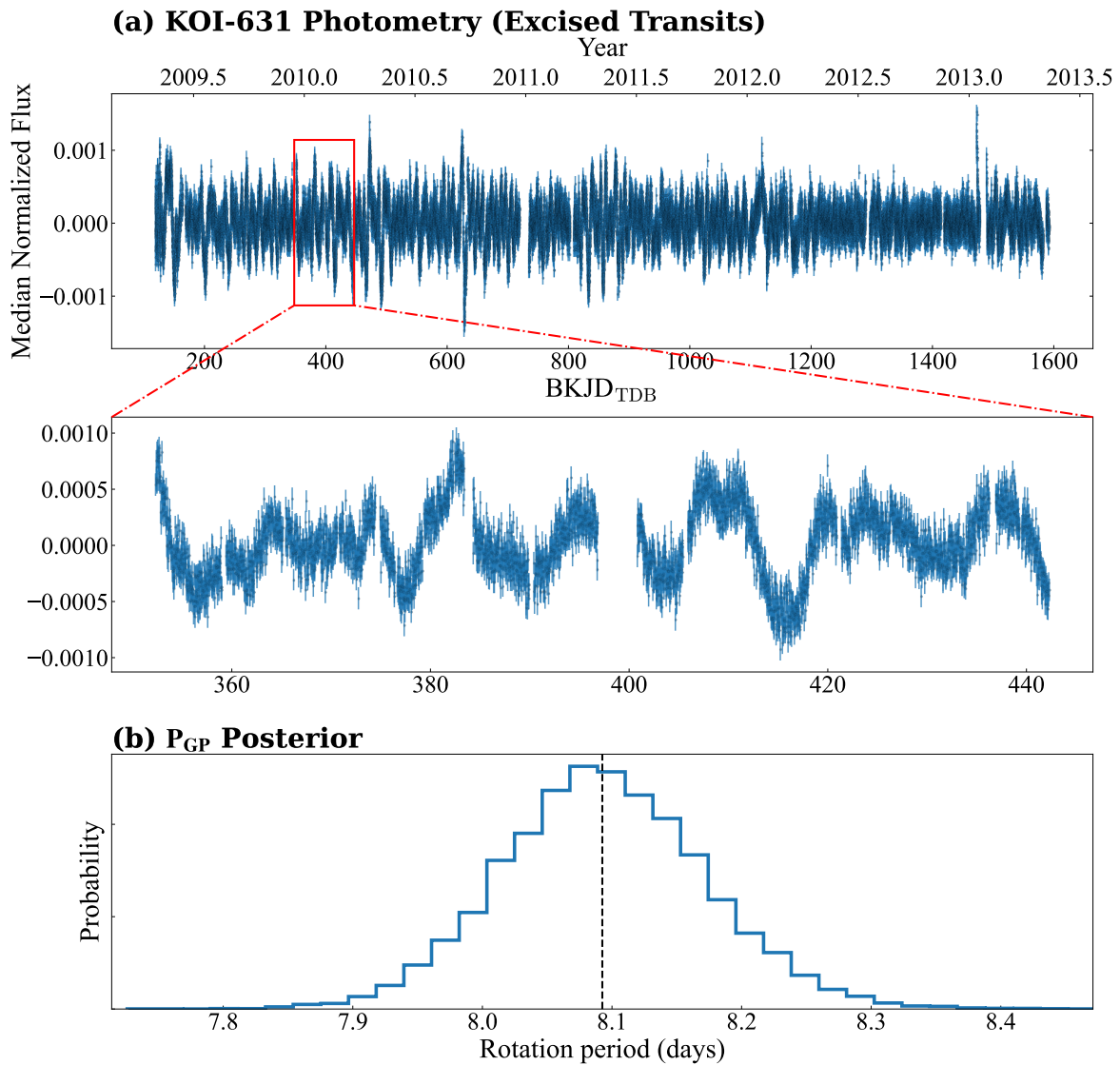


Fig. Set 7.11 – KOI-631. (a) The ARC2 corrected light curve for KOI-631, after excising the transits, with an inset displaying a subset of the Kepler data. (b) The posterior distribution for the Gaussian process period, which we interpret as a measurement of the stellar rotation period.

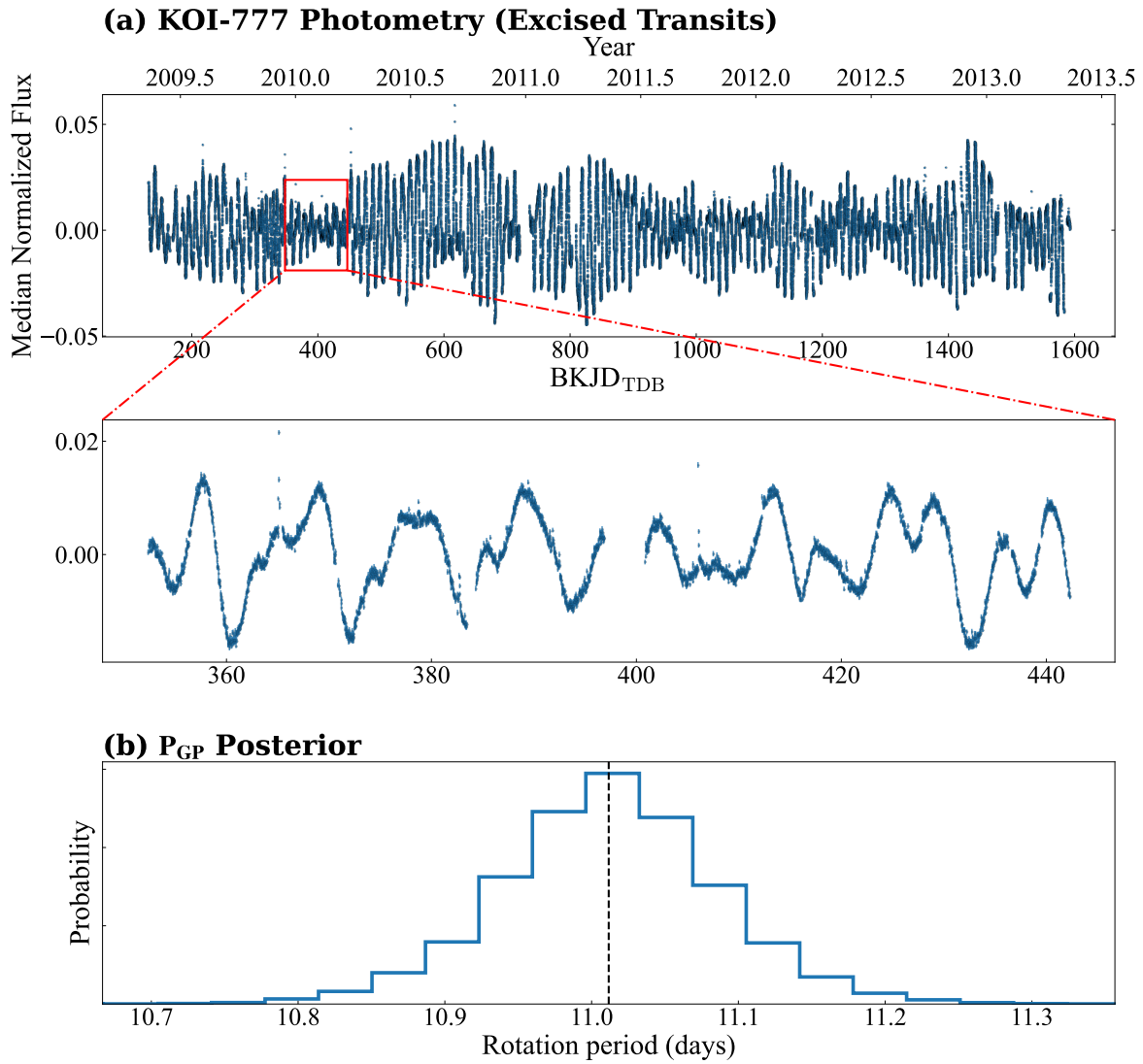


Fig. Set 7.12 – KOI-777. (a) The ARC2 corrected light curve for KOI-777, after excising the transits, with an inset displaying a subset of the Kepler data. (b) The posterior distribution for the Gaussian process period, which we interpret as a measurement of the stellar rotation period.

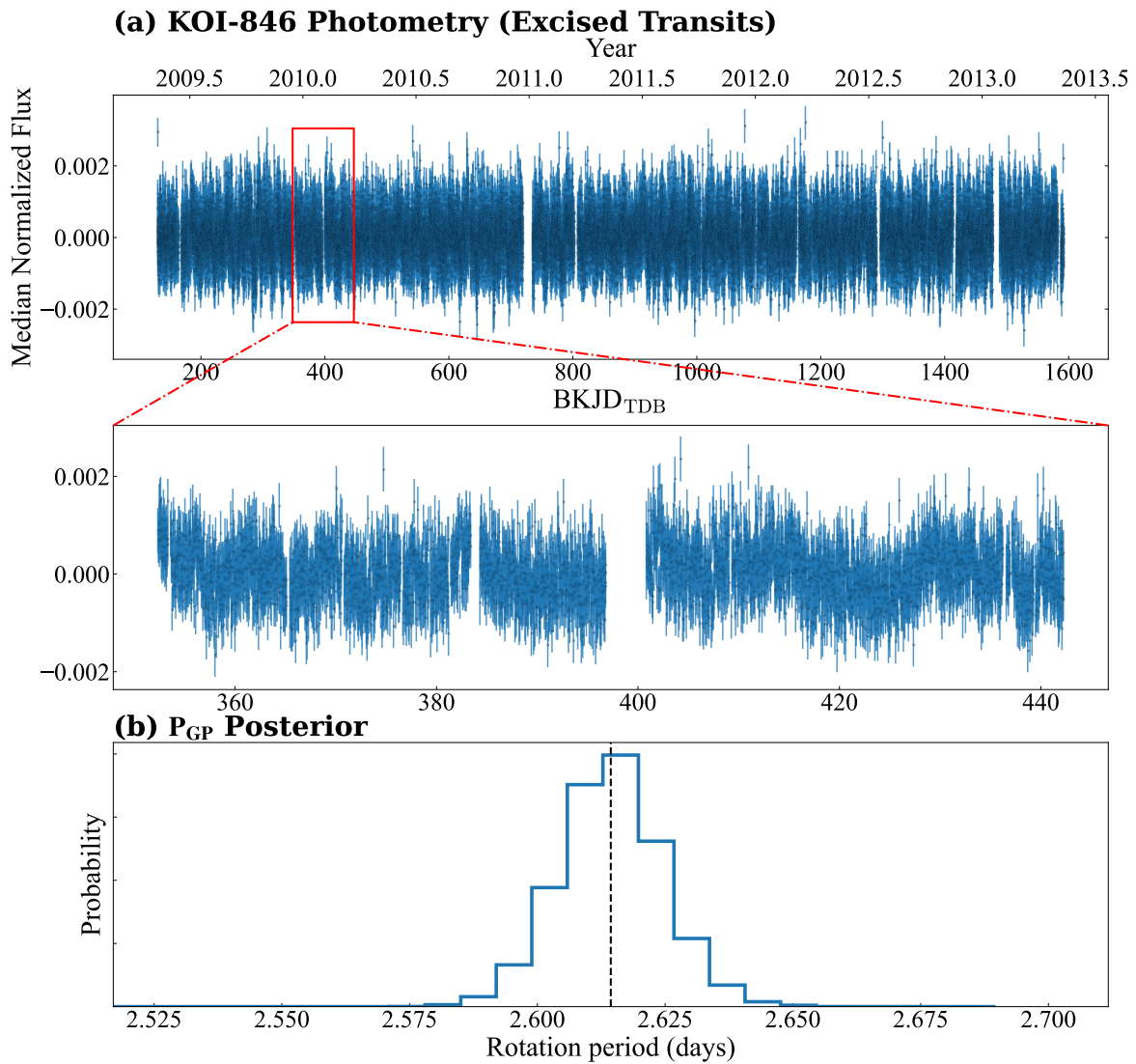


Fig. Set 7.13 – KOI-846. (a) The ARC2 corrected light curve for KOI-846, after excising the transits, with an inset displaying a subset of the Kepler data. (b) The posterior distribution for the Gaussian process period, which we interpret as a measurement of the stellar rotation period.

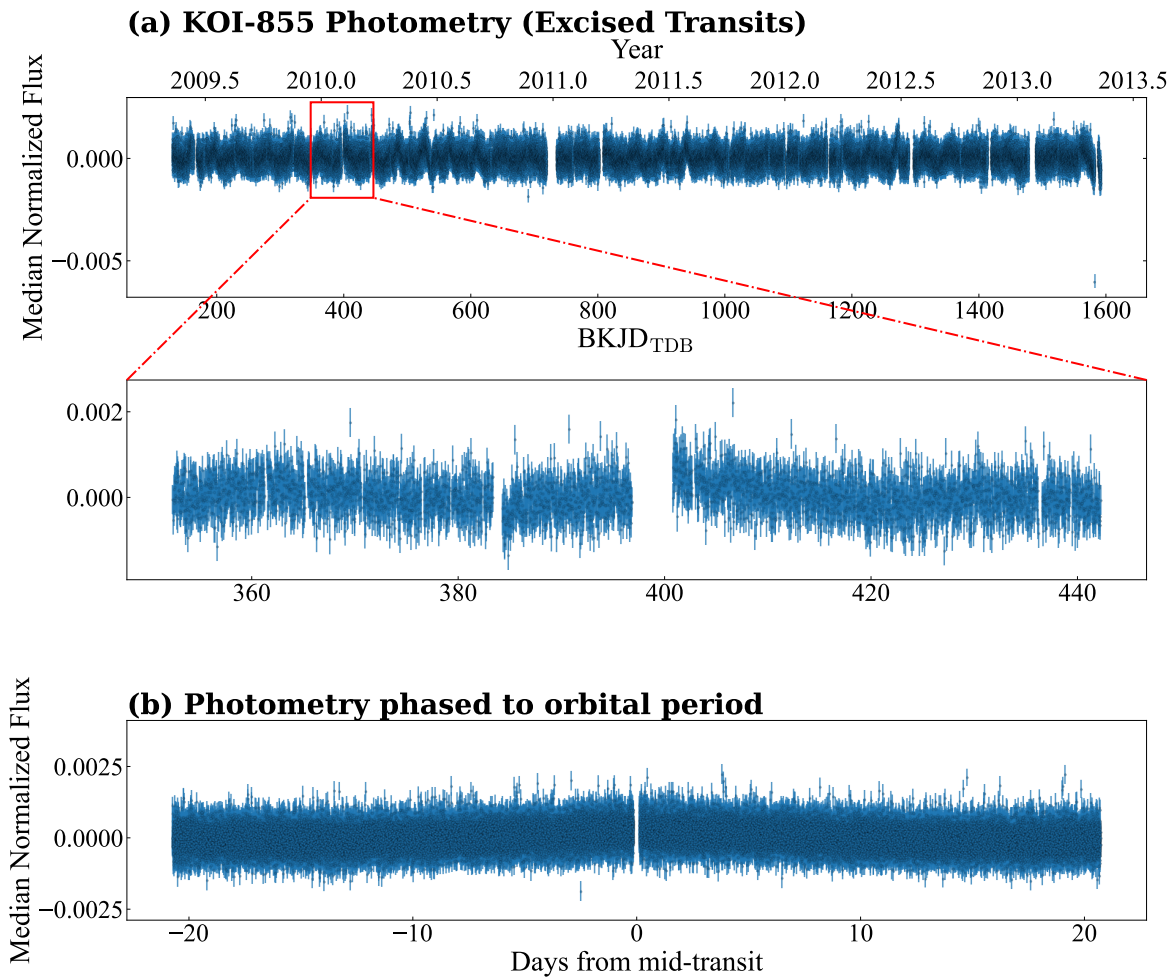


Fig. Set 7.14 – KOI-855. (a) The ARC2 corrected light curve for KOI-855, after excising the transits, with an inset displaying the quarter 2 data. (b) The out-of-transit photometric variability after phasing to the orbital ephemeris. The derived rotation period is identical (within the 1σ uncertainty) to the orbital period.

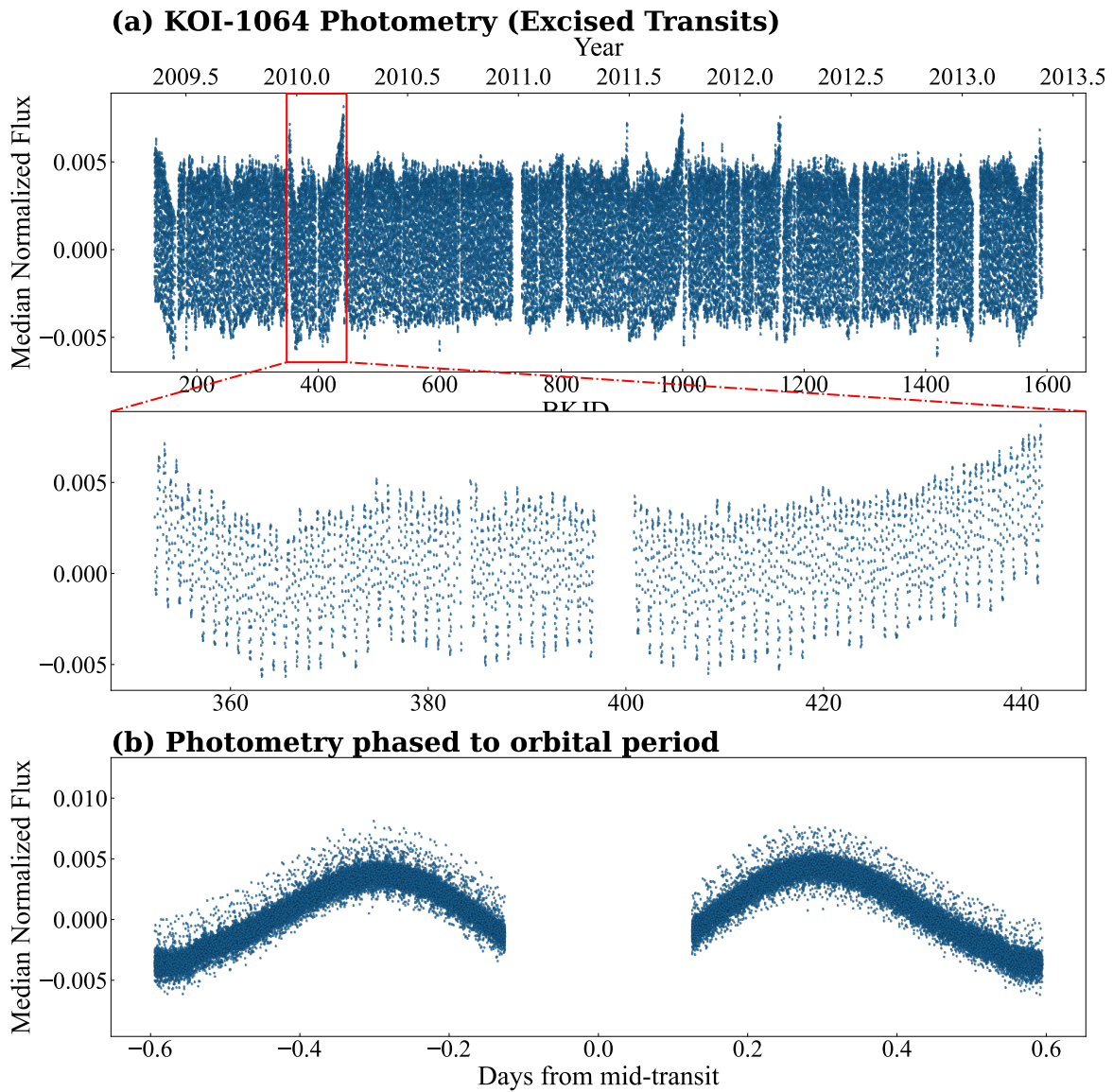


Fig. Set 7.15 – KOI-1064. (a) The ARC2 corrected light curve for KOI-1064, after excising the transits, with an inset displaying the quarter 2 data. (b) The out-of-transit photometric variability after phasing to the orbital ephemeris. The derived rotation period is identical (within the 1σ uncertainty) to the orbital period.

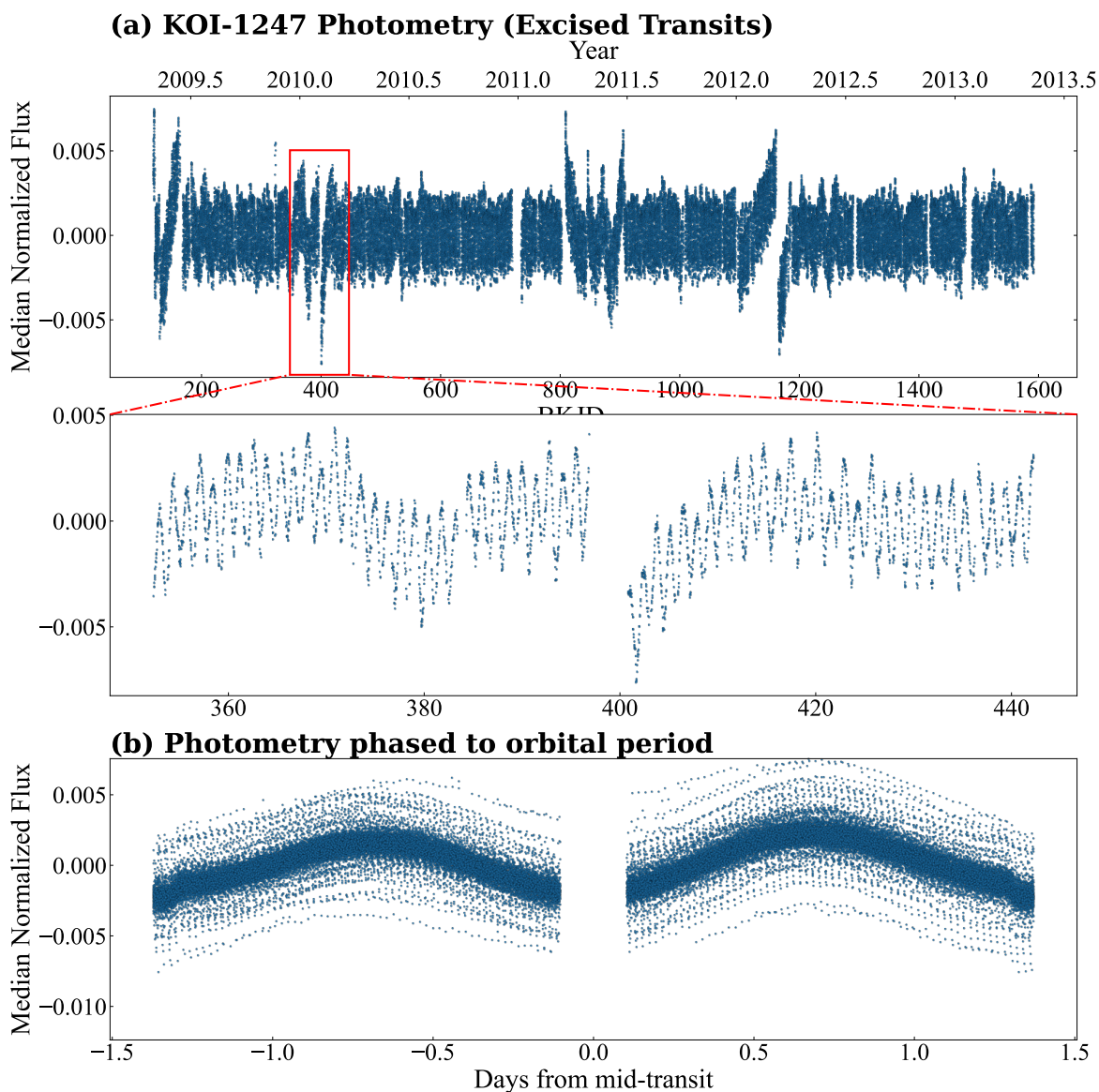


Fig. Set 7.16 – KOI-1247. (a) The ARC2 corrected light curve for KOI-1247, after excising the transits, with an inset displaying the quarter 2 data. (b) The out-of-transit photometric variability after phasing to the orbital ephemeris. The derived rotation period is identical (within the 1σ uncertainty) to the orbital period.

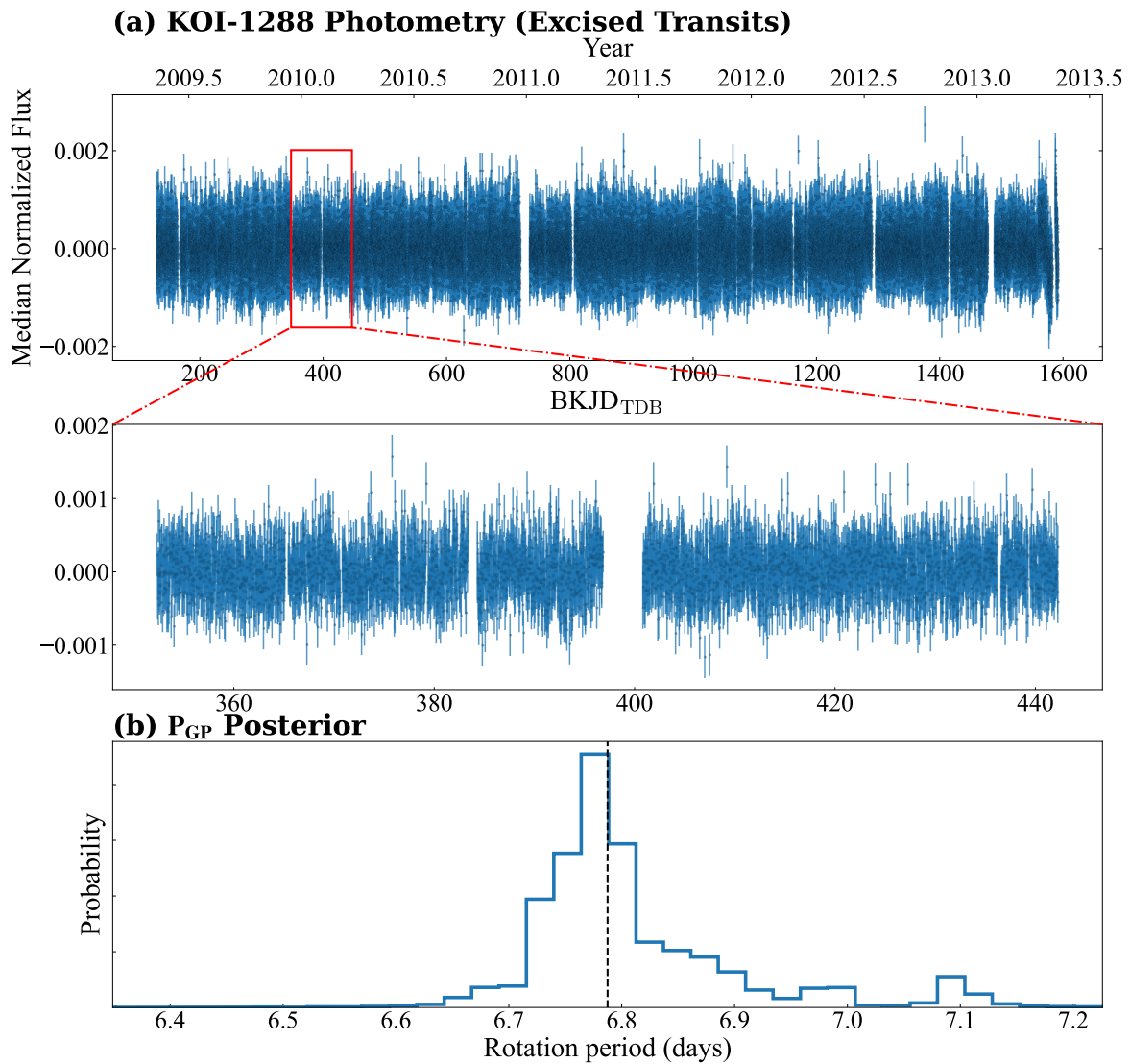


Fig. Set 7.17 – KOI-1288. (a) The ARC2 corrected light curve for KOI-1288, after excising the transits, with an inset displaying a subset of the Kepler data. (b) The posterior distribution for the Gaussian process period, which we interpret as a measurement of the stellar rotation period.

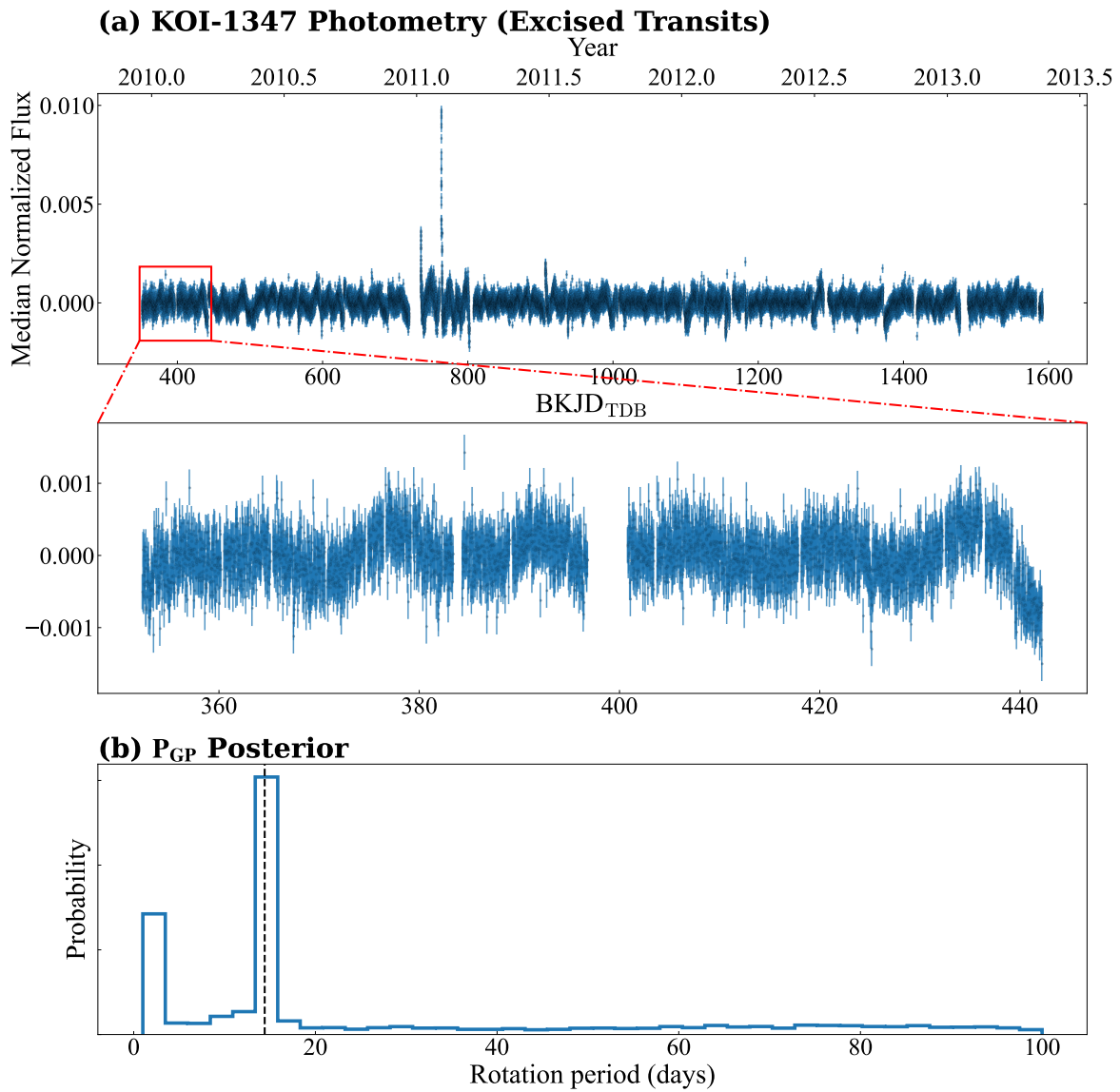


Fig. Set 7.18 – KOI-1347. (a) The ARC2 corrected light curve for KOI-1347, after excising the transits, with an inset displaying a subset of the Kepler data. (b) The posterior distribution for the Gaussian process period, which we interpret as a measurement of the stellar rotation period.

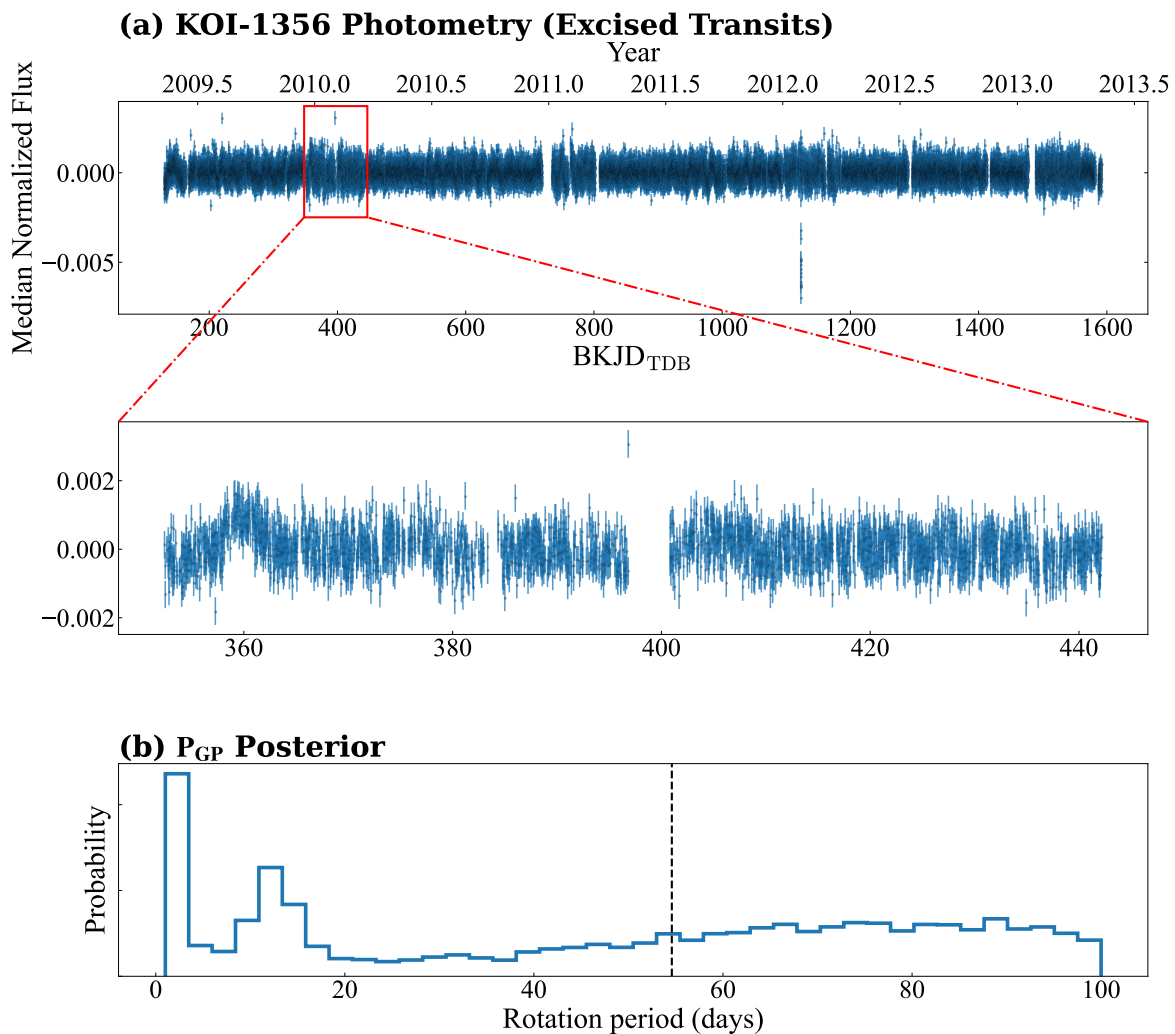


Fig. Set 7.19 – KOI-1356. (a) The ARC2 corrected light curve for KOI-1356, after excising the transits, with an inset displaying a subset of the Kepler data. (b) The posterior distribution for the Gaussian process period, which we interpret as a measurement of the stellar rotation period.

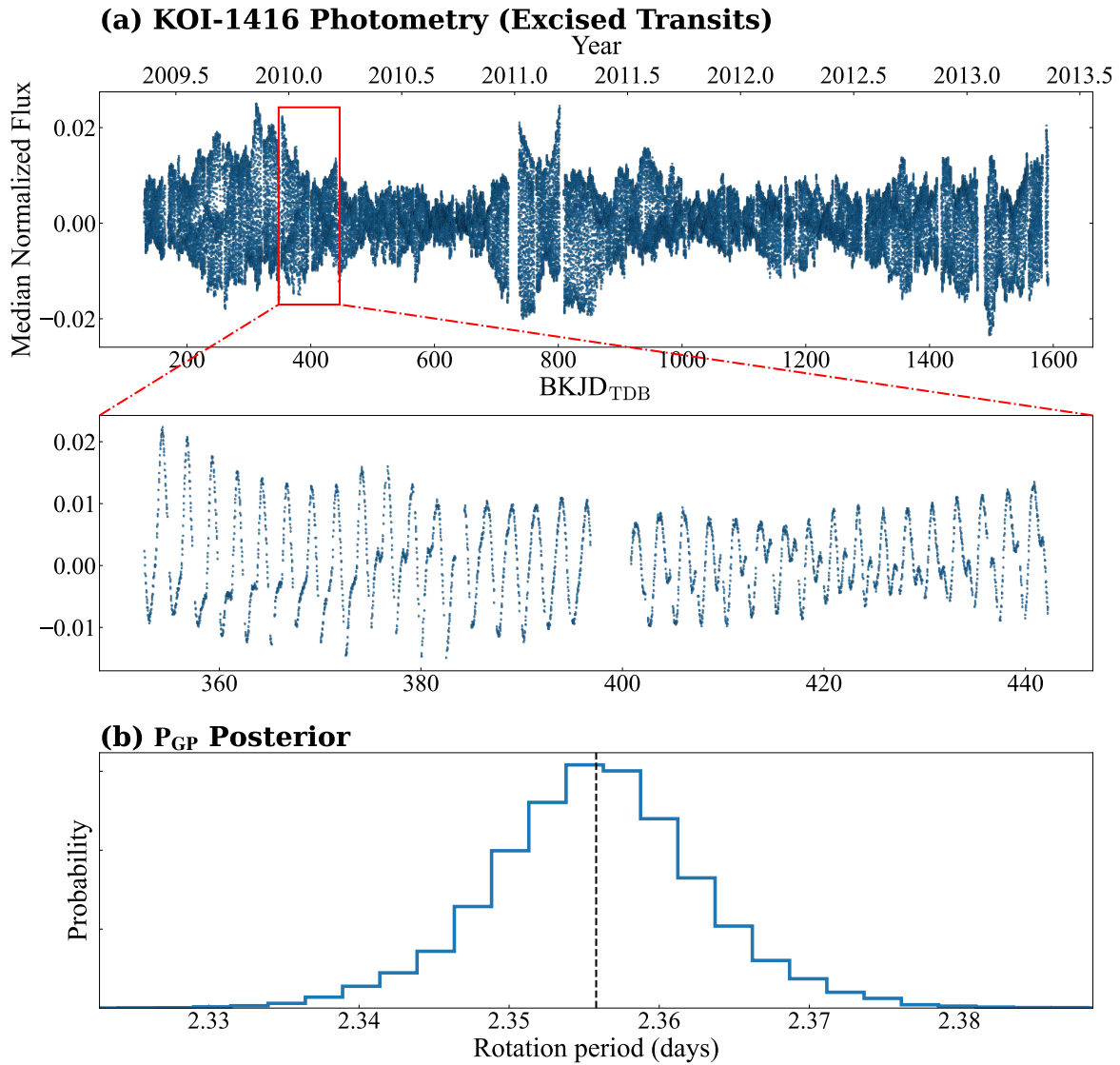


Fig. Set 7.20 – KOI-1416. (a) The ARC2 corrected light curve for KOI-1416, after excising the transits, with an inset displaying a subset of the Kepler data. (b) The posterior distribution for the Gaussian process period, which we interpret as a measurement of the stellar rotation period.

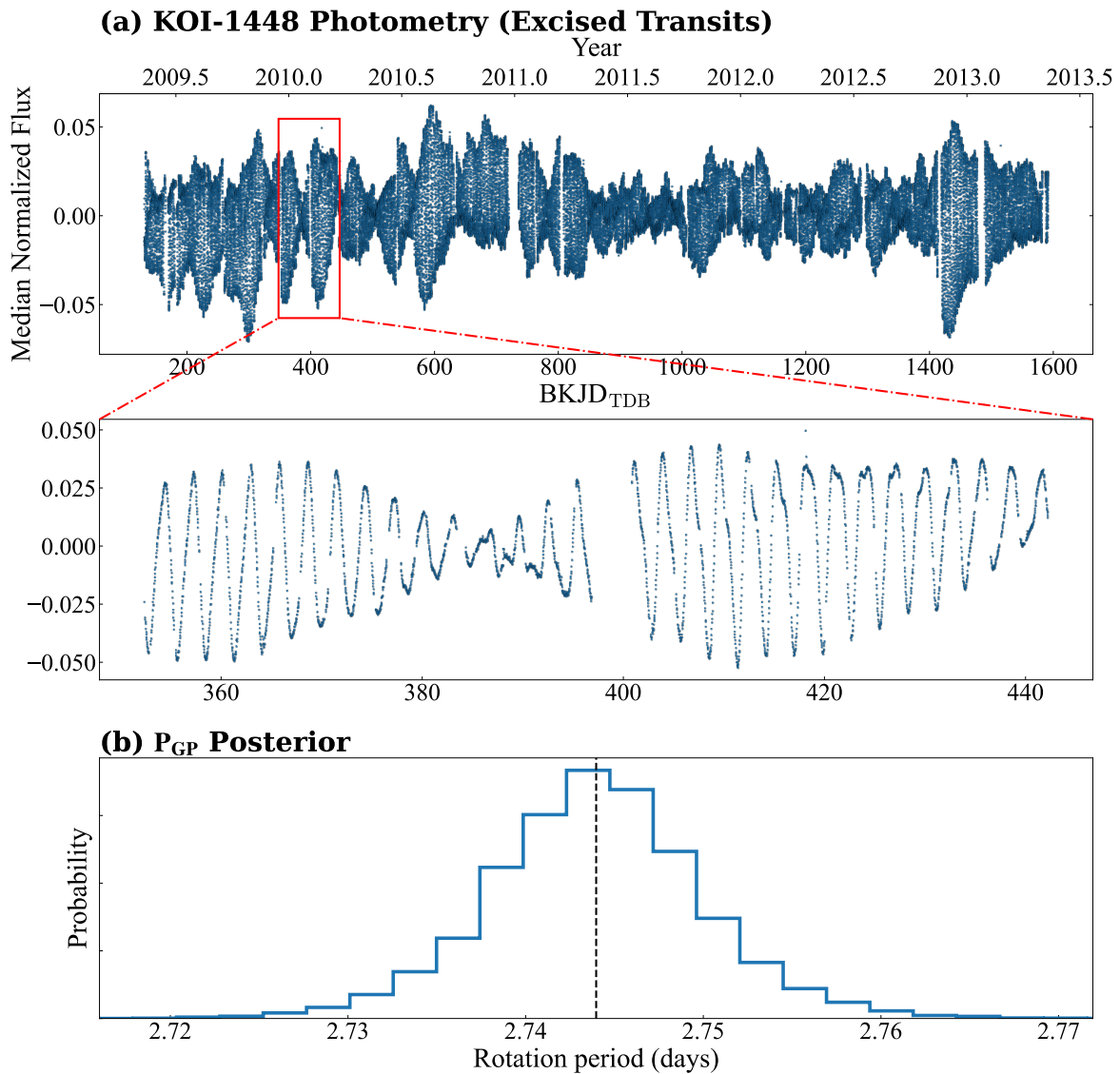


Fig. Set 7.21 – KOI-1448. (a) The ARC2 corrected light curve for KOI-1448, after excising the transits, with an inset displaying a subset of the Kepler data. (b) The posterior distribution for the Gaussian process period, which we interpret as a measurement of the stellar rotation period.

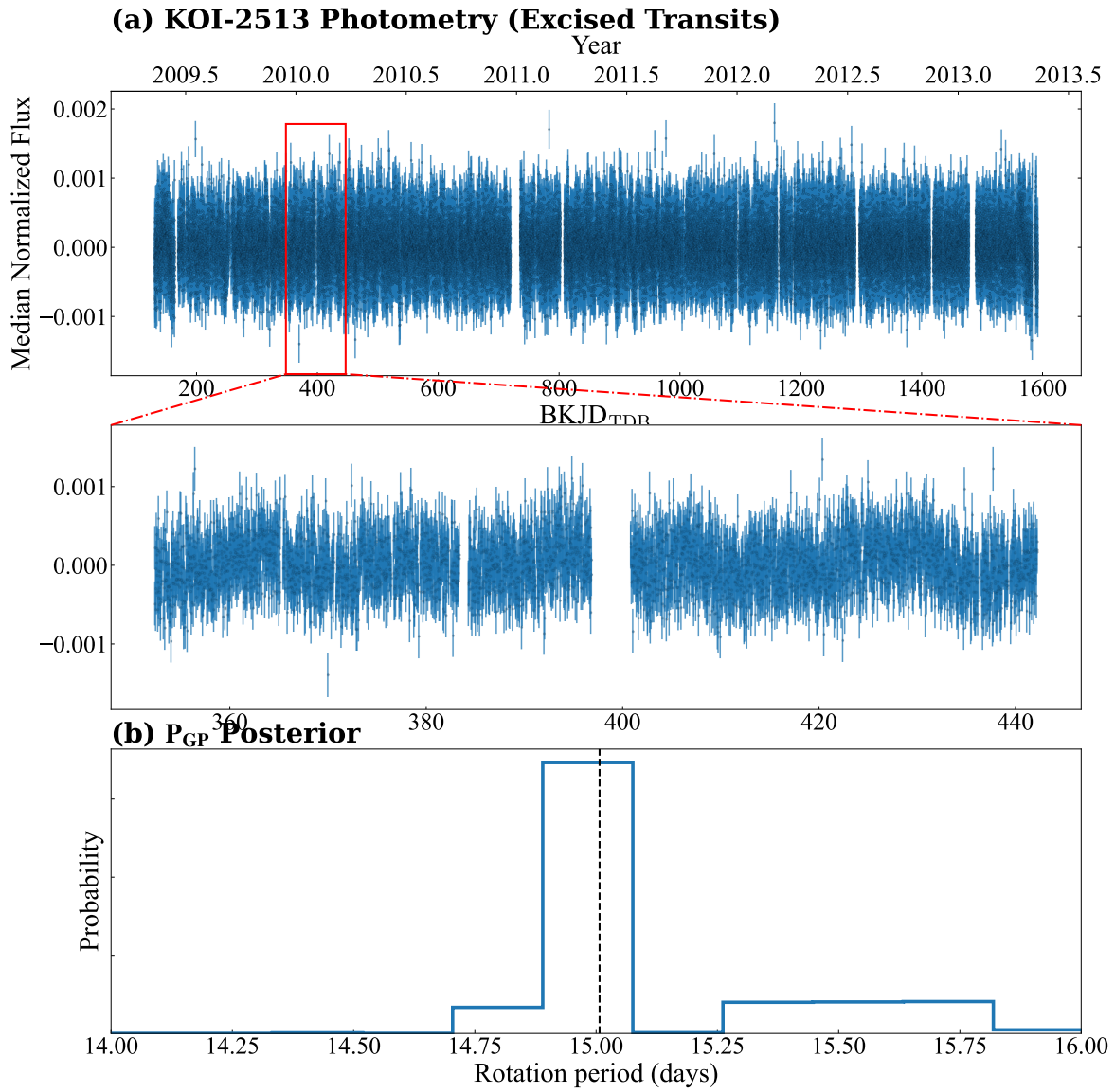


Fig. Set 7.22 – KOI-2513. (a) The ARC2 corrected light curve for KOI-2513, after excising the transits, with an inset displaying a subset of the Kepler data. (b) The posterior distribution for the Gaussian process period, which we interpret as a measurement of the stellar rotation period.

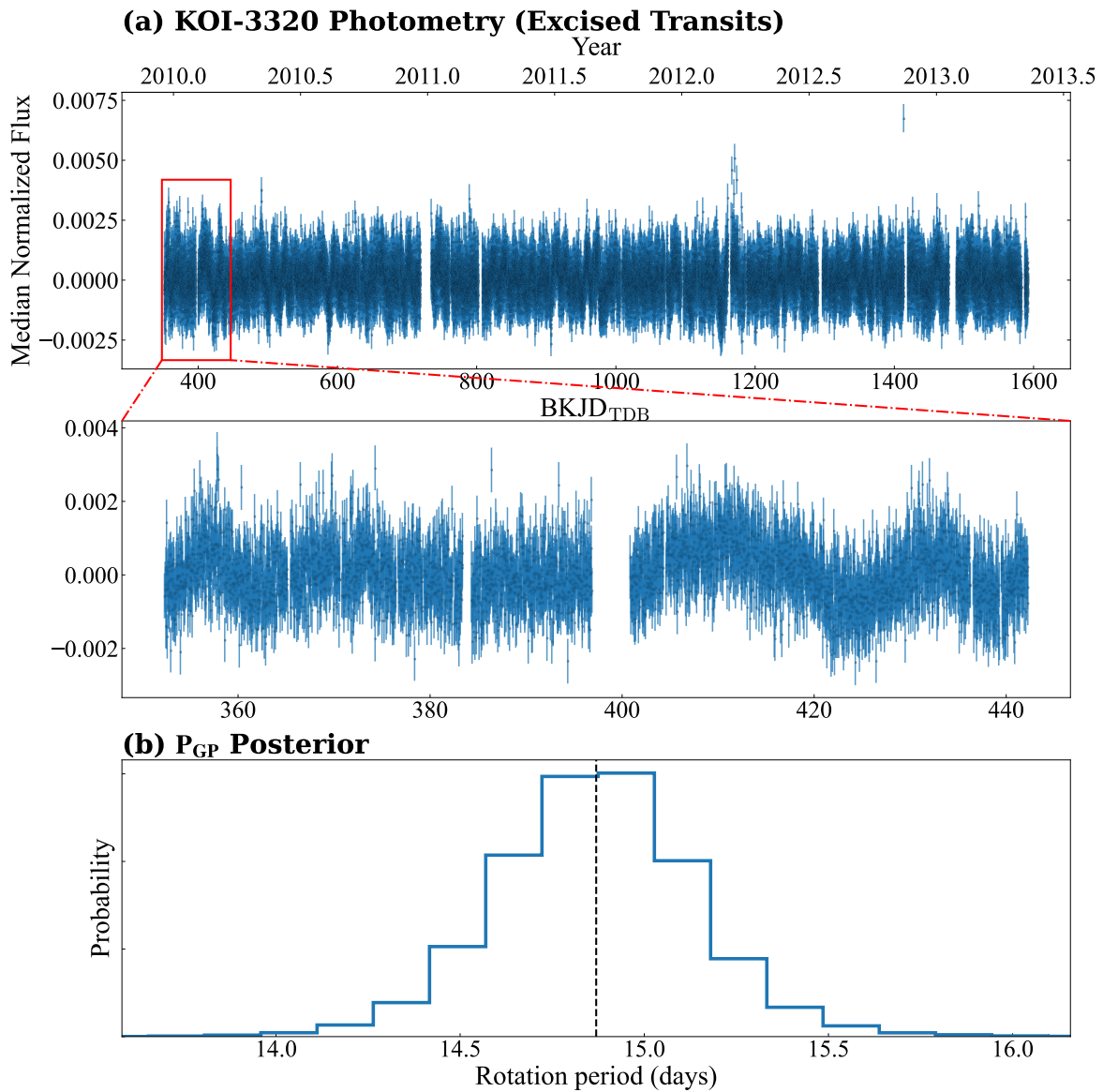


Fig. Set 7.23 – KOI-3320. (a) The ARC2 corrected light curve for KOI-3320, after excising the transits, with an inset displaying a subset of the Kepler data. (b) The posterior distribution for the Gaussian process period, which we interpret as a measurement of the stellar rotation period.

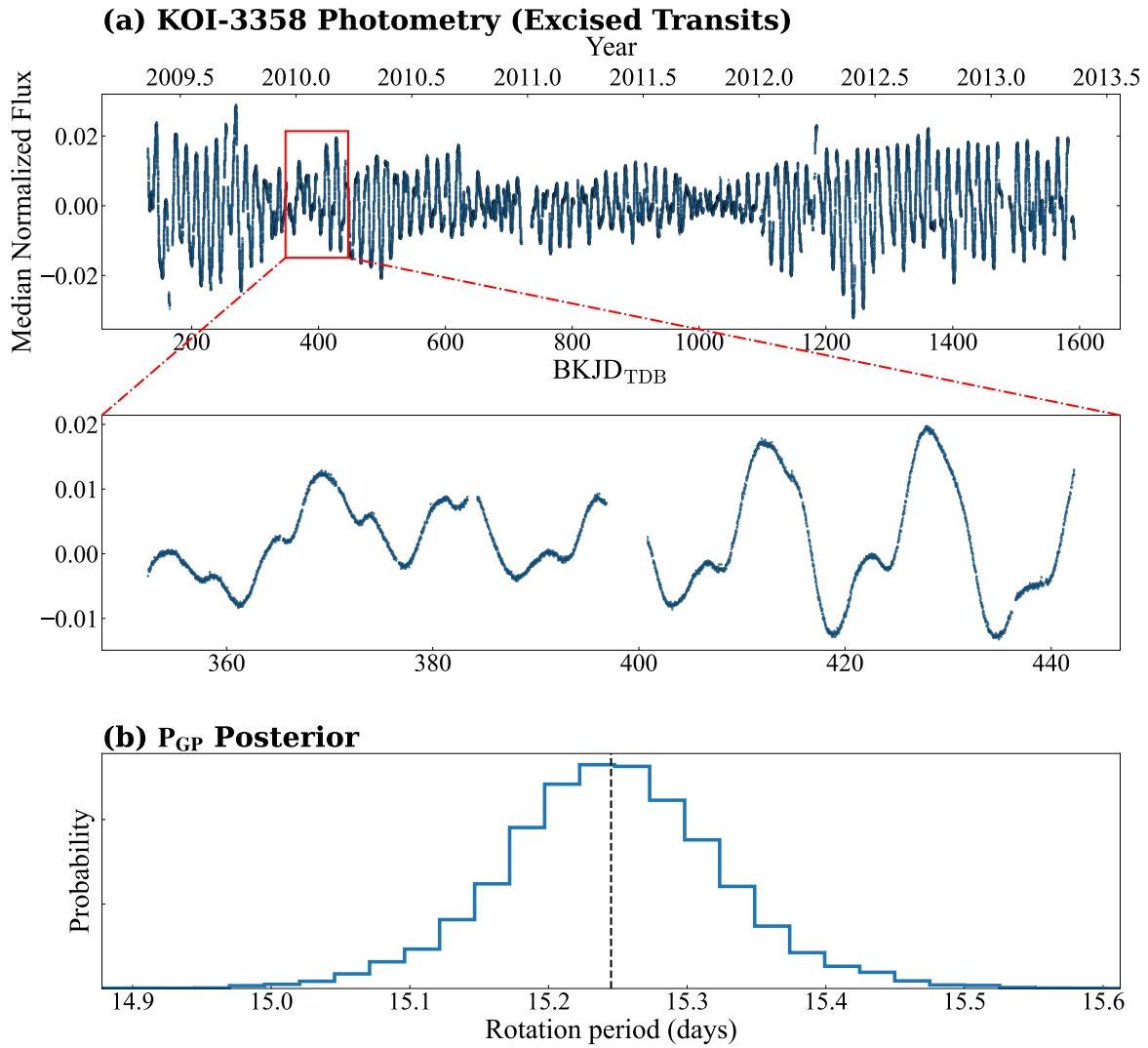


Fig. Set 7.24 – KOI-3358. (a) The ARC2 corrected light curve for KOI-3358, after excising the transits, with an inset displaying a subset of the Kepler data. (b) The posterior distribution for the Gaussian process period, which we interpret as a measurement of the stellar rotation period.

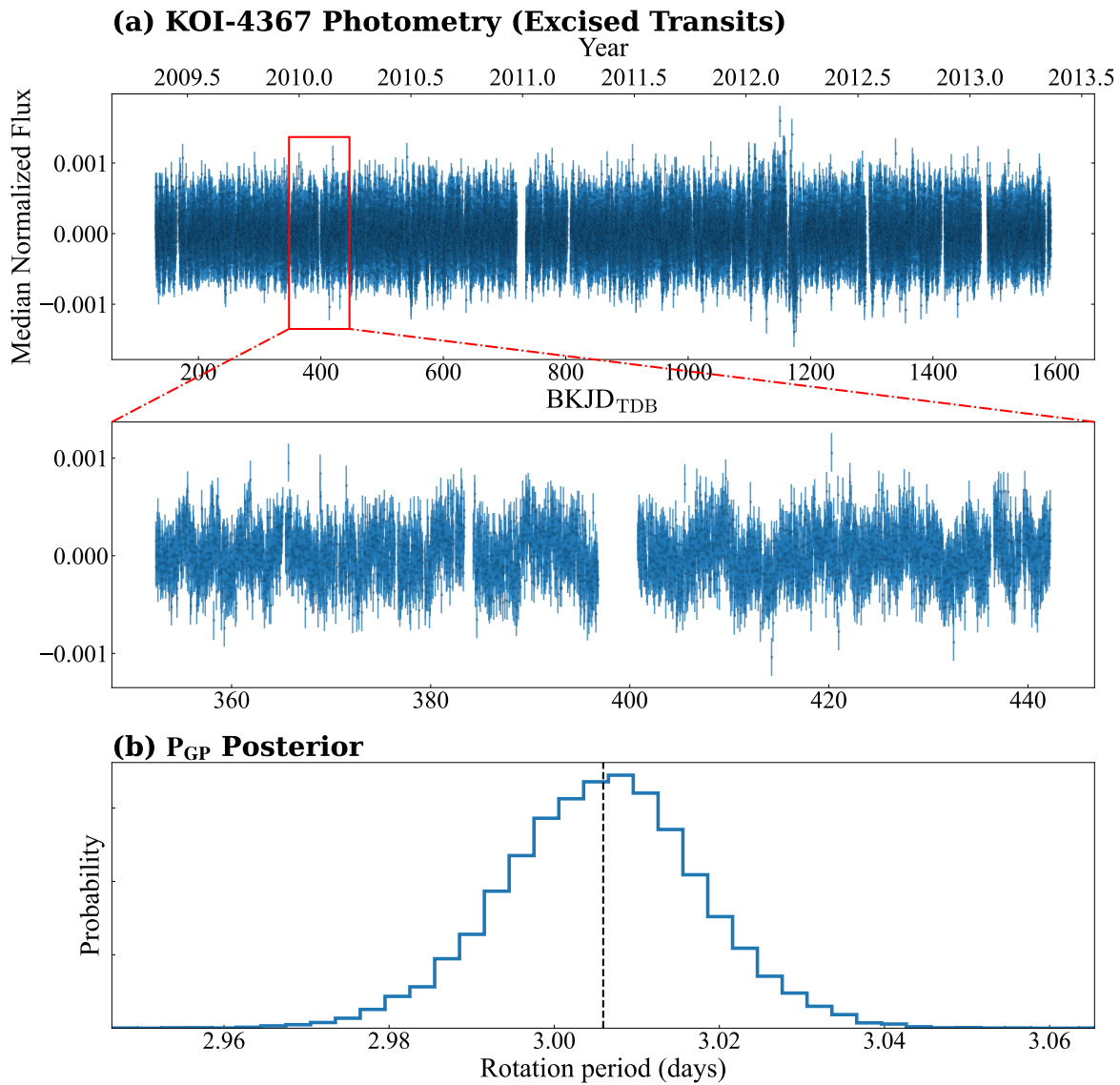


Fig. Set 7.25 – KOI-4367. (a) The ARC2 corrected light curve for KOI-4367, after excising the transits, with an inset displaying a subset of the Kepler data. (b) The posterior distribution for the Gaussian process period, which we interpret as a measurement of the stellar rotation period.

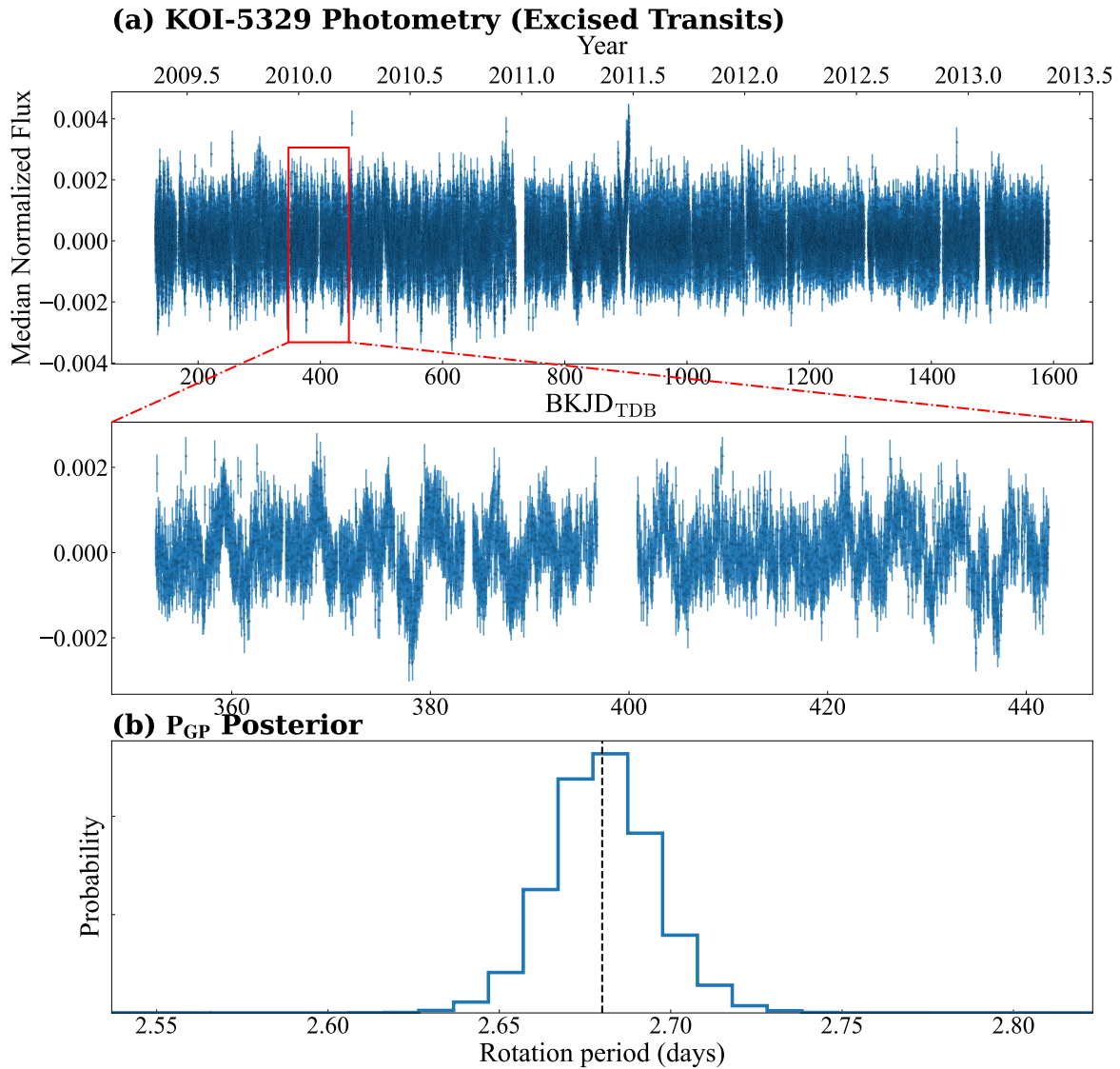


Fig. Set 7.26 – KOI-5329. (a) The ARC2 corrected light curve for KOI-5329, after excising the transits, with an inset displaying a subset of the Kepler data. (b) The posterior distribution for the Gaussian process period, which we interpret as a measurement of the stellar rotation period.

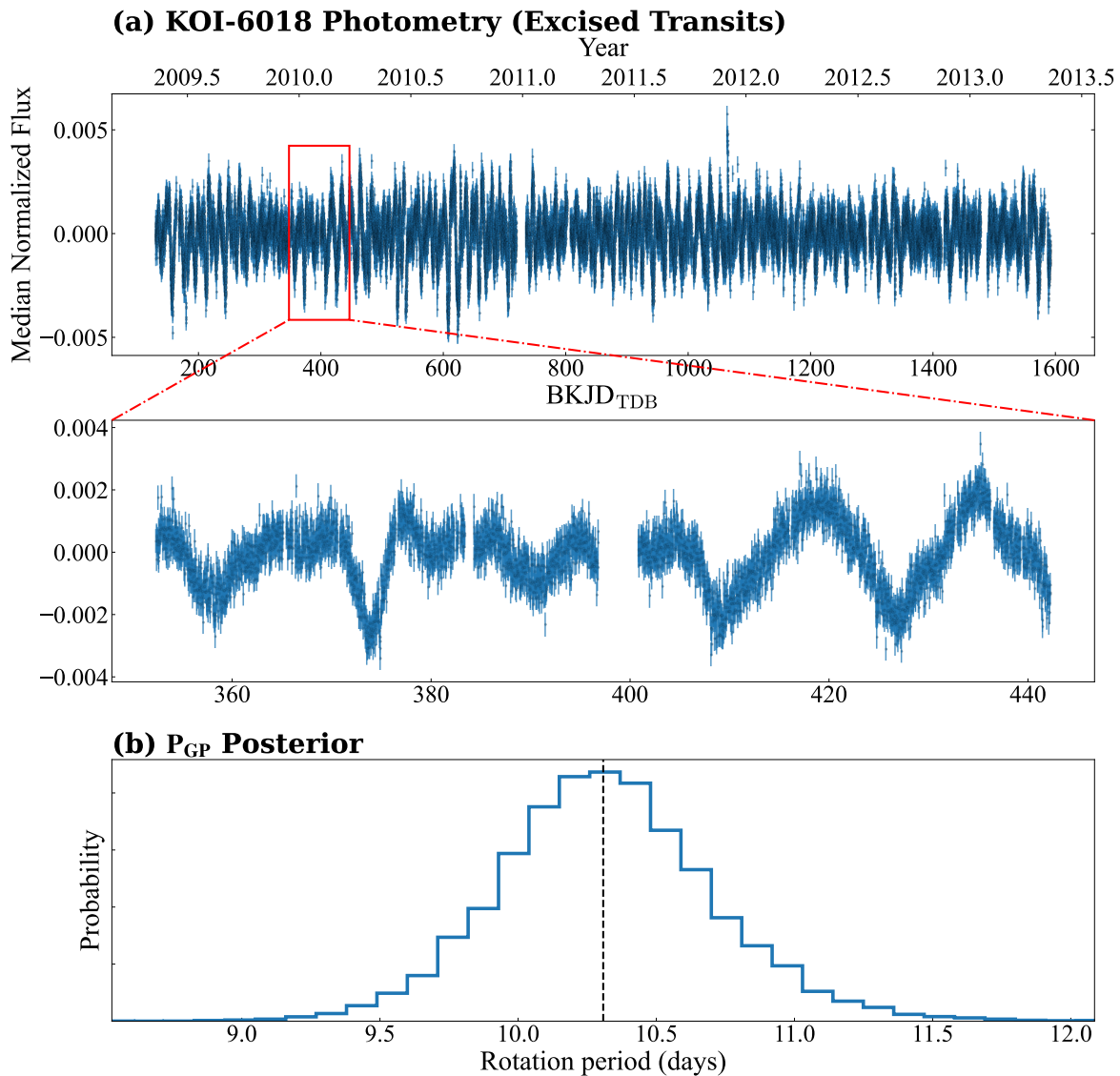


Fig. Set 7.27 – KOI-6018. (a) The ARC2 corrected light curve for KOI-6018, after excising the transits, with an inset displaying a subset of the Kepler data. (b) The posterior distribution for the Gaussian process period, which we interpret as a measurement of the stellar rotation period.

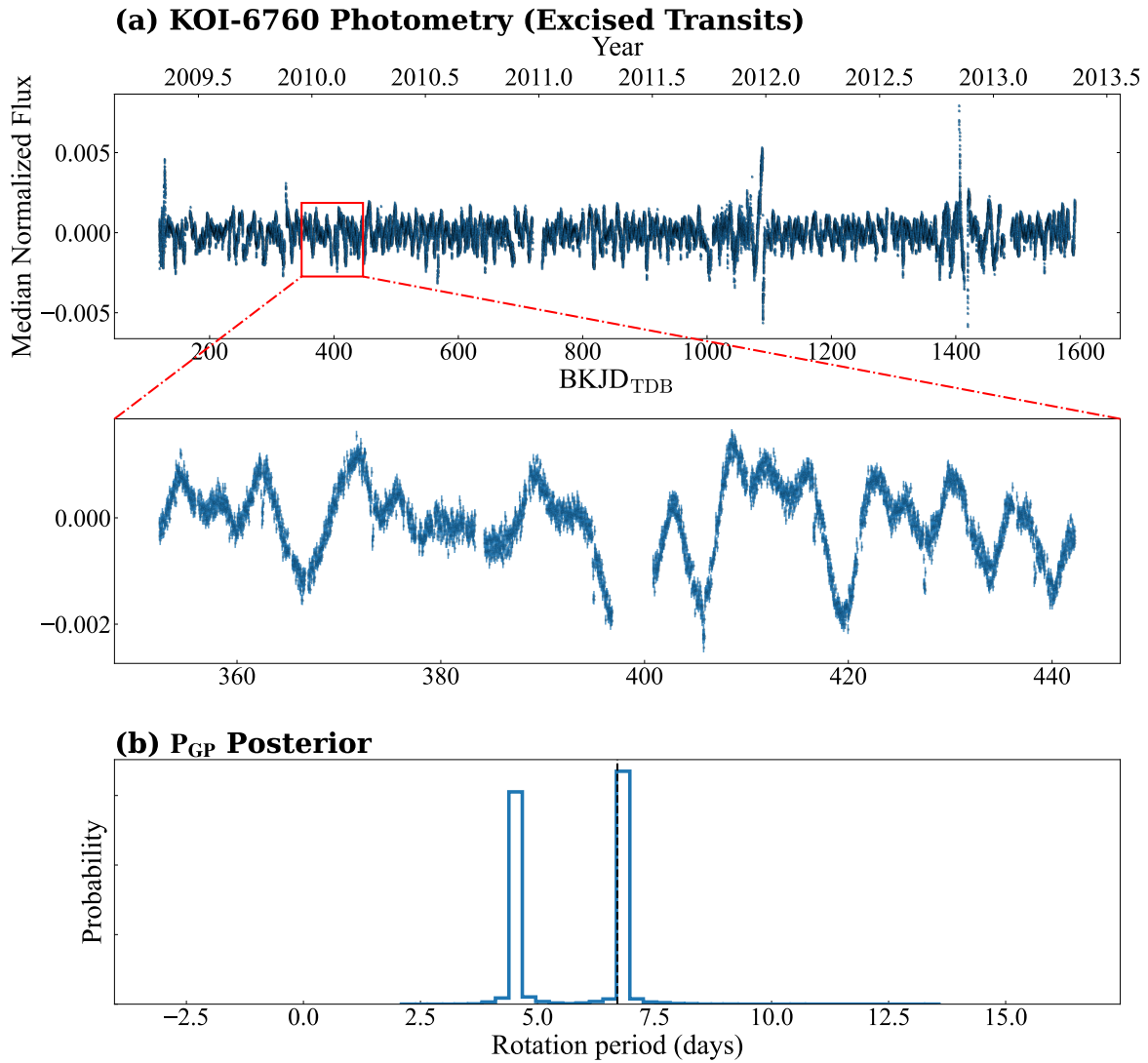


Fig. Set 7.28 – KOI-6760. (a) The ARC2 corrected light curve for KOI-6760, after excising the transits, with an inset displaying a subset of the Kepler data. (b) The posterior distribution for the Gaussian process period, which we interpret as a measurement of the stellar rotation period.

REFERENCES

- Abdurro'uf, Accetta, K., Aerts, C., et al. 2022, *ApJS*, 259, 35, doi: [10.3847/1538-4365/ac4414](https://doi.org/10.3847/1538-4365/ac4414)
- Acton, J. S., Goad, M. R., Burleigh, M. R., et al. 2021, *MNRAS*, 505, 2741, doi: [10.1093/mnras/stab1459](https://doi.org/10.1093/mnras/stab1459)
- Aigrain, S., Parviainen, H., Roberts, S., Reece, S., & Evans, T. 2017, *MNRAS*, 471, 759, doi: [10.1093/mnras/stx1422](https://doi.org/10.1093/mnras/stx1422)
- Alam, S., Albareti, F. D., Allende Prieto, C., et al. 2015, *ApJS*, 219, 12, doi: [10.1088/0067-0049/219/1/12](https://doi.org/10.1088/0067-0049/219/1/12)
- Angus, R., Morton, T., Aigrain, S., Foreman-Mackey, D., & Rajpaul, V. 2018, *MNRAS*, 474, 2094, doi: [10.1093/mnras/stx2109](https://doi.org/10.1093/mnras/stx2109)
- Astropy Collaboration, Price-Whelan, A. M., Sipőcz, B. M., et al. 2018, *AJ*, 156, 123, doi: [10.3847/1538-3881/aabc4f](https://doi.org/10.3847/1538-3881/aabc4f)
- Bailer-Jones, C. A. L., Rybizki, J., Fouesneau, M., Demleitner, M., & Andrae, R. 2021, *AJ*, 161, 147, doi: [10.3847/1538-3881/abd806](https://doi.org/10.3847/1538-3881/abd806)
- Bailer-Jones, C. A. L., Rybizki, J., Fouesneau, M., Mantelet, G., & Andrae, R. 2018, *AJ*, 156, 58, doi: [10.3847/1538-3881/aacb21](https://doi.org/10.3847/1538-3881/aacb21)
- Baraffe, I., Chabrier, G., Allard, F., & Hauschildt, P. H. 1998, *A&A*, 337, 403. <https://arxiv.org/abs/astro-ph/9805009>
- Baraffe, I., Chabrier, G., Barman, T. S., Allard, F., & Hauschildt, P. H. 2003, *A&A*, 402, 701, doi: [10.1051/0004-6361:20030252](https://doi.org/10.1051/0004-6361:20030252)
- Baraffe, I., Homeier, D., Allard, F., & Chabrier, G. 2015, *A&A*, 577, A42, doi: [10.1051/0004-6361/201425481](https://doi.org/10.1051/0004-6361/201425481)
- Baranec, C., Ziegler, C., Law, N. M., et al. 2016, *AJ*, 152, 18, doi: [10.3847/0004-6256/152/1/18](https://doi.org/10.3847/0004-6256/152/1/18)
- Baranec, C., Riddle, R., Law, N. M., et al. 2013, *Journal of Vibration Engineering*, 72, 50021, doi: [10.3791/50021](https://doi.org/10.3791/50021)
- . 2014, *ApJL*, 790, L8, doi: [10.1088/2041-8205/790/1/L8](https://doi.org/10.1088/2041-8205/790/1/L8)
- Baranne, A., Queloz, D., Mayor, M., et al. 1996, *A&AS*, 119, 373
- Bastien, F. A., Stassun, K. G., Basri, G., & Pepper, J. 2016, *ApJ*, 818, 43, doi: [10.3847/0004-637X/818/1/43](https://doi.org/10.3847/0004-637X/818/1/43)
- Bastien, F. A., Stassun, K. G., & Pepper, J. 2014, *ApJL*, 788, L9, doi: [10.1088/2041-8205/788/1/L9](https://doi.org/10.1088/2041-8205/788/1/L9)
- Batalha, N. E., Lewis, T., Fortney, J. J., et al. 2019, *ApJL*, 885, L25, doi: [10.3847/2041-8213/ab4909](https://doi.org/10.3847/2041-8213/ab4909)
- Beaton, R. L., Oelkers, R. J., Hayes, C. R., et al. 2021, *AJ*, 162, 302, doi: [10.3847/1538-3881/ac260c](https://doi.org/10.3847/1538-3881/ac260c)
- Belokurov, V., Penoyre, Z., Oh, S., et al. 2020, *MNRAS*, 496, 1922, doi: [10.1093/mnras/staa1522](https://doi.org/10.1093/mnras/staa1522)
- Bender, C. F., Mahadevan, S., Deshpande, R., et al. 2012, *ApJL*, 751, L31, doi: [10.1088/2041-8205/751/2/L31](https://doi.org/10.1088/2041-8205/751/2/L31)
- Berger, T. A., Huber, D., Gaidos, E., van Saders, J. L., & Weiss, L. M. 2020, *AJ*, 160, 108, doi: [10.3847/1538-3881/aba18a](https://doi.org/10.3847/1538-3881/aba18a)
- Birkby, J., Nefs, B., Hodgkin, S., et al. 2012, *MNRAS*, 426, 1507, doi: [10.1111/j.1365-2966.2012.21514.x](https://doi.org/10.1111/j.1365-2966.2012.21514.x)
- Blanton, M. R., Bershady, M. A., Abolfathi, B., et al. 2017, *AJ*, 154, 28, doi: [10.3847/1538-3881/aa7567](https://doi.org/10.3847/1538-3881/aa7567)
- Bonomo, A. S., Desidera, S., Benatti, S., et al. 2017, *A&A*, 602, A107, doi: [10.1051/0004-6361/201629882](https://doi.org/10.1051/0004-6361/201629882)
- Borucki, W. J., Koch, D., Basri, G., et al. 2010, *Science*, 327, 977, doi: [10.1126/science.1185402](https://doi.org/10.1126/science.1185402)
- Bouchy, F., Hébrard, G., Udry, S., et al. 2009, *A&A*, 505, 853, doi: [10.1051/0004-6361/200912427](https://doi.org/10.1051/0004-6361/200912427)
- Bouma, L. G., Masuda, K., & Winn, J. N. 2018, *AJ*, 155, 244, doi: [10.3847/1538-3881/aabfb810.48550/arXiv.1804.07764](https://doi.org/10.3847/1538-3881/aabfb810.48550/arXiv.1804.07764)
- Bryson, S., Kunimoto, M., Kopparapu, R. K., et al. 2021, *AJ*, 161, 36, doi: [10.3847/1538-3881/abc418](https://doi.org/10.3847/1538-3881/abc418)
- Bryson, S. T., Jenkins, J. M., Gilliland, R. L., et al. 2013, *PASP*, 125, 889, doi: [10.1086/671767](https://doi.org/10.1086/671767)
- Burrows, A., Heng, K., & Nampaisarn, T. 2011, *ApJ*, 736, 47, doi: [10.1088/0004-637X/736/1/47](https://doi.org/10.1088/0004-637X/736/1/47)
- Cañas, C. I., Bender, C. F., Mahadevan, S., et al. 2018, *ApJL*, 861, L4, doi: [10.3847/2041-8213/aacbc5](https://doi.org/10.3847/2041-8213/aacbc5)
- Cañas, C. I., Wang, S., Mahadevan, S., et al. 2019a, *ApJ*, 870, L17, doi: [10.3847/2041-8213/aafa1e](https://doi.org/10.3847/2041-8213/aafa1e)
- Cañas, C. I., Stefánsson, G., Monson, A. J., et al. 2019b, *ApJL*, 877, L29, doi: [10.3847/2041-8213/ab21c0](https://doi.org/10.3847/2041-8213/ab21c0)

- Cañas, C. I., Mahadevan, S., Bender, C. F., et al. 2022, *AJ*, 163, 89, doi: [10.3847/1538-3881/ac415f](https://doi.org/10.3847/1538-3881/ac415f)
- Carmichael, T. W., Quinn, S. N., Mustill, A. J., et al. 2020, *AJ*, 160, 53, doi: [10.3847/1538-3881/ab9b84](https://doi.org/10.3847/1538-3881/ab9b84)
- Chabrier, G., Gallardo, J., & Baraffe, I. 2007, *A&A*, 472, L17, doi: [10.1051/0004-6361:20077702](https://doi.org/10.1051/0004-6361:20077702)
- Chabrier, G., Johansen, A., Janson, M., & Rafikov, R. 2014, in *Protostars and Planets VI*, ed. H. Beuther, R. S. Klessen, C. P. Dullemond, & T. Henning, 619, doi: [10.2458/azu_uapress.9780816531240-ch027](https://doi.org/10.2458/azu_uapress.9780816531240-ch027)
- Chaturvedi, P., Sharma, R., Chakraborty, A., Anandarao, B. G., & Prasad, N. J. S. S. V. 2018, *AJ*, 156, 27, doi: [10.3847/1538-3881/aac5de](https://doi.org/10.3847/1538-3881/aac5de)
- Chen, J., & Kipping, D. 2017, *ApJ*, 834, 17, doi: [10.3847/1538-4357/834/1/17](https://doi.org/10.3847/1538-4357/834/1/17)
- Choi, J., Dotter, A., Conroy, C., et al. 2016, *ApJ*, 823, 102, doi: [10.3847/0004-637X/823/2/102](https://doi.org/10.3847/0004-637X/823/2/102)
- Christiansen, J. L., Jenkins, J. M., Caldwell, D. A., et al. 2012, *PASP*, 124, 1279, doi: [10.1086/668847](https://doi.org/10.1086/668847)
- Ciardi, D. R., Beichman, C. A., Horch, E. P., & Howell, S. B. 2015, *ApJ*, 805, 16, doi: [10.1088/0004-637X/805/1/1610.48550/arXiv.1503.03516](https://doi.org/10.1088/0004-637X/805/1/1610.48550/arXiv.1503.03516)
- Coughlin, J. L., Mullally, F., Thompson, S. E., et al. 2016, *ApJS*, 224, 12, doi: [10.3847/0067-0049/224/1/12](https://doi.org/10.3847/0067-0049/224/1/12)
- Croll, B., Rappaport, S., & Levine, A. M. 2015, *MNRAS*, 449, 1408, doi: [10.1093/mnras/stv297](https://doi.org/10.1093/mnras/stv297)
- Csizmadia, S., & CoRoT Team. 2016, III.6 Exploration of the brown dwarf regime around solar-like stars by CoRoT, 143, doi: [10.1051/978-2-7598-1876-1.c036](https://doi.org/10.1051/978-2-7598-1876-1.c036)
- Cui, K., Liu, J., Yang, S., et al. 2019, *MNRAS*, 489, 5513, doi: [10.1093/mnras/stz2432](https://doi.org/10.1093/mnras/stz2432)
- Cutri, R. M., Skrutskie, M. F., van Dyk, S., et al. 2003, *VizieR Online Data Catalog*, 2246
- Delrez, L., Gillon, M., Queloz, D., et al. 2018, in *Society of Photo-Optical Instrumentation Engineers (SPIE) Conference Series*, Vol. 10700, *Ground-based and Airborne Telescopes VII*, ed. H. K. Marshall & J. Spyromilio, 107001I, doi: [10.1117/12.2312475](https://doi.org/10.1117/12.2312475)
- Díaz, R. F., Almenara, J. M., Santerne, A., et al. 2014, *MNRAS*, 441, 983, doi: [10.1093/mnras/stu601](https://doi.org/10.1093/mnras/stu601)
- Dieterich, S. B., Simler, A., Henry, T. J., & Jao, W.-C. 2021, *AJ*, 161, 172, doi: [10.3847/1538-3881/abd2c2](https://doi.org/10.3847/1538-3881/abd2c2)
- Dorn, C., Khan, A., Heng, K., et al. 2015, *A&A*, 577, A83, doi: [10.1051/0004-6361/201424915](https://doi.org/10.1051/0004-6361/201424915)
- Dotter, A. 2016, *ApJS*, 222, 8, doi: [10.3847/0067-0049/222/1/8](https://doi.org/10.3847/0067-0049/222/1/8)
- Duquenois, A., & Mayor, M. 1991, *A&A*, 500, 337
- Eastman, J. D., Rodriguez, J. E., Agol, E., et al. 2019, arXiv e-prints, arXiv:1907.09480, <https://arxiv.org/abs/1907.09480>
- Ehrenreich, D., Lagrange, A. M., Bouchy, F., et al. 2011, *A&A*, 525, A85, doi: [10.1051/0004-6361/201015729](https://doi.org/10.1051/0004-6361/201015729)
- Eisenstein, D. J., Weinberg, D. H., Agol, E., et al. 2011, *AJ*, 142, 72, doi: [10.1088/0004-6256/142/3/72](https://doi.org/10.1088/0004-6256/142/3/72)
- Engel, M., Faigler, S., Shahaf, S., & Mazeh, T. 2020, *MNRAS*, 497, 4884, doi: [10.1093/mnras/staa2182](https://doi.org/10.1093/mnras/staa2182)
- Espinoza, N., Kossakowski, D., & Brahm, R. 2019, *MNRAS*, 490, 2262, doi: [10.1093/mnras/stz2688](https://doi.org/10.1093/mnras/stz2688)
- Everett, M. E., Howell, S. B., & Kinemuchi, K. 2012, *PASP*, 124, 316, doi: [10.1086/665529](https://doi.org/10.1086/665529)
- Faigler, S., & Mazeh, T. 2011, *MNRAS*, 415, 3921, doi: [10.1111/j.1365-2966.2011.19011.x](https://doi.org/10.1111/j.1365-2966.2011.19011.x)
- Feiden, G. A. 2016, *A&A*, 593, A99, doi: [10.1051/0004-6361/201527613](https://doi.org/10.1051/0004-6361/201527613)
- Feiden, G. A., & Chaboyer, B. 2013, *ApJ*, 779, 183, doi: [10.1088/0004-637X/779/2/183](https://doi.org/10.1088/0004-637X/779/2/183)
- Fitton, S., Tofflemire, B. M., & Kraus, A. L. 2022, *Research Notes of the American Astronomical Society*, 6, 18, doi: [10.3847/2515-5172/ac4bb710.48550/arXiv.2206.02695](https://doi.org/10.3847/2515-5172/ac4bb710.48550/arXiv.2206.02695)
- Fleming, S. W., Mahadevan, S., Deshpande, R., et al. 2015, *AJ*, 149, 143, doi: [10.1088/0004-6256/149/4/143](https://doi.org/10.1088/0004-6256/149/4/143)
- Foreman-Mackey, D., Agol, E., Ambikasaran, S., & Angus, R. 2017, *AJ*, 154, 220, doi: [10.3847/1538-3881/aa9332](https://doi.org/10.3847/1538-3881/aa9332)
- Forgan, D. H., Hall, C., Meru, F., & Rice, W. K. M. 2018, *MNRAS*, 474, 5036, doi: [10.1093/mnras/stx2870](https://doi.org/10.1093/mnras/stx2870)
- Fulton, B. J., Petigura, E. A., Blunt, S., & Sinukoff, E. 2018, *PASP*, 130, 044504, doi: [10.1088/1538-3873/aaaaa8](https://doi.org/10.1088/1538-3873/aaaaa8)
- Gaia Collaboration, Vallenari, A., Brown, A. G. A., et al. 2022, arXiv e-prints, arXiv:2208.00211, <https://arxiv.org/abs/2208.00211>

- García Pérez, A. E., Allende Prieto, C., Holtzman, J. A., et al. 2016, *AJ*, 151, 144, doi: [10.3847/0004-6256/151/6/144](https://doi.org/10.3847/0004-6256/151/6/144)
- Gilhool, S. H., Blake, C. H., Terrien, R. C., et al. 2018, *VizieR Online Data Catalog*, J/AJ/155/38
- Ginsburg, A., Sipőcz, B. M., Brasseur, C. E., et al. 2019, *AJ*, 157, 98, doi: [10.3847/1538-3881/aa9c33](https://doi.org/10.3847/1538-3881/aa9c33)
- Green, G. M. 2018, *The Journal of Open Source Software*, 3, 695, doi: [10.21105/joss.00695](https://doi.org/10.21105/joss.00695)
- Green, G. M., Schlafly, E., Zucker, C., Speagle, J. S., & Finkbeiner, D. 2019, *ApJ*, 887, 93, doi: [10.3847/1538-4357/ab5362](https://doi.org/10.3847/1538-4357/ab5362)
- Green, G. M., Schlafly, E. F., Finkbeiner, D., et al. 2018, *MNRAS*, 478, 651, doi: [10.1093/mnras/sty1008](https://doi.org/10.1093/mnras/sty1008)
- Grether, D., & Lineweaver, C. H. 2006, *ApJ*, 640, 1051, doi: [10.1086/500161](https://doi.org/10.1086/500161)
- Grievés, N., Ge, J., Thomas, N., et al. 2017, *MNRAS*, 467, 4264, doi: [10.1093/mnras/stx334](https://doi.org/10.1093/mnras/stx334)
- Grievés, N., Bouchy, F., Lendl, M., et al. 2021, *A&A*, 652, A127, doi: [10.1051/0004-6361/202141145](https://doi.org/10.1051/0004-6361/202141145)
- Gunn, J. E., Siegmund, W. A., Mannery, E. J., et al. 2006, *AJ*, 131, 2332, doi: [10.1086/500975](https://doi.org/10.1086/500975)
- Gustafsson, B., Edvardsson, B., Eriksson, K., et al. 2008, *A&A*, 486, 951, doi: [10.1051/0004-6361:200809724](https://doi.org/10.1051/0004-6361:200809724)
- Halbwachs, J. L., Mayor, M., & Udry, S. 2005, *A&A*, 431, 1129, doi: [10.1051/0004-6361:20041219](https://doi.org/10.1051/0004-6361:20041219)
- Henden, A. A., Levine, S., Terrell, D., et al. 2018, in *American Astronomical Society Meeting Abstracts*, Vol. 232, American Astronomical Society Meeting Abstracts #232, 223.06
- Hill, G. J., Lee, H., MacQueen, P. J., et al. 2021, *AJ*, 162, 298, doi: [10.3847/1538-3881/ac2c02](https://doi.org/10.3847/1538-3881/ac2c02)
- Holl, B., Perryman, M., Lindegren, L., Segransan, D., & Raimbault, M. 2022, *A&A*, 661, A151, doi: [10.1051/0004-6361/201936393](https://doi.org/10.1051/0004-6361/201936393)
- Holtzman, J. A., Shetrone, M., Johnson, J. A., et al. 2015, *AJ*, 150, 148, doi: [10.1088/0004-6256/150/5/148](https://doi.org/10.1088/0004-6256/150/5/148)
- Holtzman, J. A., Hasselquist, S., Shetrone, M., et al. 2018, *AJ*, 156, 125, doi: [10.3847/1538-3881/aad4f9](https://doi.org/10.3847/1538-3881/aad4f9)
- Horne, K. 1986, *PASP*, 98, 609, doi: [10.1086/131801](https://doi.org/10.1086/131801)
- Howell, S. B., Sobek, C., Haas, M., et al. 2014, *PASP*, 126, 398, doi: [10.1086/676406](https://doi.org/10.1086/676406)
- Huang, C. X., Vanderburg, A., Pál, A., et al. 2020a, *Research Notes of the American Astronomical Society*, 4, 204, doi: [10.3847/2515-5172/abca2e](https://doi.org/10.3847/2515-5172/abca2e)
- . 2020b, *Research Notes of the American Astronomical Society*, 4, 206, doi: [10.3847/2515-5172/abca2d](https://doi.org/10.3847/2515-5172/abca2d)
- Hunter, J. D. 2007, *Computing In Science & Engineering*, 9, 90, doi: [10.1109/MCSE.2007.55](https://doi.org/10.1109/MCSE.2007.55)
- Husser, T. O., Wende-von Berg, S., Dreizler, S., et al. 2013, *A&A*, 553, A6, doi: [10.1051/0004-6361/201219058](https://doi.org/10.1051/0004-6361/201219058)
- Irwin, J. M., Berta-Thompson, Z. K., Charbonneau, D., et al. 2015, in *Cambridge Workshop on Cool Stars, Stellar Systems, and the Sun*, Vol. 18, 18th Cambridge Workshop on Cool Stars, Stellar Systems, and the Sun, 767–772. <https://arxiv.org/abs/1409.0891>
- Irwin, J. M., Quinn, S. N., Berta, Z. K., et al. 2011, *ApJ*, 742, 123, doi: [10.1088/0004-637X/742/2/123](https://doi.org/10.1088/0004-637X/742/2/123)
- Jackson, R. J., Deliyannis, C. P., & Jeffries, R. D. 2018, *MNRAS*, 476, 3245, doi: [10.1093/mnras/sty374](https://doi.org/10.1093/mnras/sty374)
- Jenkins, J. M., Twicken, J. D., McCauliff, S., et al. 2016, in *Proc. SPIE*, Vol. 9913, *Software and Cyberinfrastructure for Astronomy IV*, 99133E, doi: [10.1117/12.2233418](https://doi.org/10.1117/12.2233418)
- Jensen-Clem, R., Duev, D. A., Riddle, R., et al. 2018, *AJ*, 155, 32, doi: [10.3847/1538-3881/aa9be6](https://doi.org/10.3847/1538-3881/aa9be6)
- Jönsson, H., Holtzman, J. A., Allende Prieto, C., et al. 2020, *AJ*, 160, 120, doi: [10.3847/1538-3881/aba592](https://doi.org/10.3847/1538-3881/aba592)
- Kanodia, S., Wolfgang, A., Stefánsson, G. K., Ning, B., & Mahadevan, S. 2019, *ApJ*, 882, 38, doi: [10.3847/1538-4357/ab334c](https://doi.org/10.3847/1538-4357/ab334c)
- Kanodia, S., & Wright, J. 2018, *Research Notes of the American Astronomical Society*, 2, 4, doi: [10.3847/2515-5172/aaa4b7](https://doi.org/10.3847/2515-5172/aaa4b7)
- Kanodia, S., Mahadevan, S., Ramsey, L. W., et al. 2018, in *Society of Photo-Optical Instrumentation Engineers (SPIE) Conference Series*, Vol. 10702, *Ground-based and Airborne Instrumentation for Astronomy VII*, ed. C. J. Evans, L. Simard, & H. Takami, 107026Q, doi: [10.1117/12.2313491](https://doi.org/10.1117/12.2313491)

- Kaplan, K. F., Bender, C. F., Terrien, R. C., et al. 2019, in *Astronomical Society of the Pacific Conference Series*, Vol. 523, *Astronomical Data Analysis Software and Systems XXVII*, ed. P. J. Teuben, M. W. Pound, B. A. Thomas, & E. M. Warner, 567
- Kervella, P., Arenou, F., Mignard, F., & Thévenin, F. 2019, *A&A*, 623, A72, doi: [10.1051/0004-6361/201834371](https://doi.org/10.1051/0004-6361/201834371)
- Kervella, P., Arenou, F., & Thévenin, F. 2022, *A&A*, 657, A7, doi: [10.1051/0004-6361/202142146](https://doi.org/10.1051/0004-6361/202142146)
- Kesseli, A. Y., Muirhead, P. S., Mann, A. W., & Mace, G. 2018, *AJ*, 155, 225, doi: [10.3847/1538-3881/aabccb](https://doi.org/10.3847/1538-3881/aabccb)
- Kiefer, F., Hébrard, G., Lecavelier des Etangs, A., et al. 2021, *A&A*, 645, A7, doi: [10.1051/0004-6361/202039168](https://doi.org/10.1051/0004-6361/202039168)
- Kiefer, F., Hébrard, G., Sahlmann, J., et al. 2019, *A&A*, 631, A125, doi: [10.1051/0004-6361/201935113](https://doi.org/10.1051/0004-6361/201935113)
- Kinemuchi, K., Barclay, T., Fanelli, M., et al. 2012, *PASP*, 124, 963, doi: [10.1086/667603](https://doi.org/10.1086/667603)
- Kirk, B., Conroy, K., Prša, A., et al. 2016, *AJ*, 151, 68, doi: [10.3847/0004-6256/151/3/68](https://doi.org/10.3847/0004-6256/151/3/68)
- Koch, D. G., Borucki, W. J., Basri, G., et al. 2010, *ApJL*, 713, L79, doi: [10.1088/2041-8205/713/2/L79](https://doi.org/10.1088/2041-8205/713/2/L79)
- Kopparapu, R. k., Wolf, E. T., Arney, G., et al. 2017, *ApJ*, 845, 5, doi: [10.3847/1538-4357/aa7cf9](https://doi.org/10.3847/1538-4357/aa7cf9)
- Kopparapu, R. K., Ramirez, R., Kasting, J. F., et al. 2013, *ApJ*, 765, 131, doi: [10.1088/0004-637X/765/2/131](https://doi.org/10.1088/0004-637X/765/2/131)
- Kraus, A. L., Tucker, R. A., Thompson, M. I., Craine, E. R., & Hillenbrand, L. A. 2011, *ApJ*, 728, 48, doi: [10.1088/0004-637X/728/1/48](https://doi.org/10.1088/0004-637X/728/1/48)
- Law, N. M., Morton, T., Baranec, C., et al. 2014, *ApJ*, 791, 35, doi: [10.1088/0004-637X/791/1/35](https://doi.org/10.1088/0004-637X/791/1/35)
- Lindgren, L. 2018, Re-normalising the astrometric chi-square in Gaia DR2, Technical note, Lund Observatory. http://www.rssd.esa.int/doc_fetch.php?id=3757412
- Lindgren, L., Klioner, S. A., Hernández, J., et al. 2021, *A&A*, 649, A2, doi: [10.1051/0004-6361/202039709](https://doi.org/10.1051/0004-6361/202039709)
- Lockwood, A. C., Johnson, J. A., Bender, C. F., et al. 2014, *ApJL*, 783, L29, doi: [10.1088/2041-8205/783/2/L29](https://doi.org/10.1088/2041-8205/783/2/L29)
- López-Morales, M. 2007, *ApJ*, 660, 732, doi: [10.1086/513142](https://doi.org/10.1086/513142)
- López-Morales, M., & Ribas, I. 2005, *ApJ*, 631, 1120, doi: [10.1086/432680](https://doi.org/10.1086/432680)
- Ma, B., & Ge, J. 2014, *MNRAS*, 439, 2781, doi: [10.1093/mnras/stu134](https://doi.org/10.1093/mnras/stu134)
- MacDonald, J., & Mullan, D. J. 2017, *ApJ*, 850, 58, doi: [10.3847/1538-4357/aa9611](https://doi.org/10.3847/1538-4357/aa9611)
- Magnier, E. A., Schlafly, E. F., Finkbeiner, D. P., et al. 2020, *ApJS*, 251, 6, doi: [10.3847/1538-4365/abb82a](https://doi.org/10.3847/1538-4365/abb82a)
- Mahadevan, S., Ramsey, L., Bender, C., et al. 2012, in *Society of Photo-Optical Instrumentation Engineers (SPIE) Conference Series*, Vol. 8446, *Proc. SPIE*, 84461S, doi: [10.1117/12.926102](https://doi.org/10.1117/12.926102)
- Mahadevan, S., Ramsey, L. W., Terrien, R., et al. 2014, in *Proc. SPIE*, Vol. 9147, *Ground-based and Airborne Instrumentation for Astronomy V*, 91471G, doi: [10.1117/12.2056417](https://doi.org/10.1117/12.2056417)
- Majewski, S. R., Schiavon, R. P., Frinchaboy, P. M., et al. 2017, *AJ*, 154, 94, doi: [10.3847/1538-3881/aa784d](https://doi.org/10.3847/1538-3881/aa784d)
- Maldonado, J., & Villaver, E. 2017, *A&A*, 602, A38, doi: [10.1051/0004-6361/201630120](https://doi.org/10.1051/0004-6361/201630120)
- Mandel, K., & Agol, E. 2002, *ApJ*, 580, L171, doi: [10.1086/345520](https://doi.org/10.1086/345520)
- Mann, A. W., Feiden, G. A., Gaidos, E., Boyajian, T., & von Braun, K. 2015, *ApJ*, 804, 64, doi: [10.1088/0004-637X/804/1/64](https://doi.org/10.1088/0004-637X/804/1/64)
- Mann, A. W., Dupuy, T., Kraus, A. L., et al. 2019, *ApJ*, 871, 63, doi: [10.3847/1538-4357/aaf3bc](https://doi.org/10.3847/1538-4357/aaf3bc)
- Marley, M. S., Saumon, D., Visscher, C., et al. 2021, *ApJ*, 920, 85, doi: [10.3847/1538-4357/ac141d](https://doi.org/10.3847/1538-4357/ac141d)
- Mathur, S., Huber, D., Batalha, N. M., et al. 2017, *ApJS*, 229, 30, doi: [10.3847/1538-4365/229/2/30](https://doi.org/10.3847/1538-4365/229/2/30)
- Matson, R. A., Gies, D. R., Guo, Z., & Williams, S. J. 2017, *AJ*, 154, 216, doi: [10.3847/1538-3881/aa8fd6](https://doi.org/10.3847/1538-3881/aa8fd6)
- McCullough, P. R., Crouzet, N., Deming, D., & Madhusudhan, N. 2014, *ApJ*, 791, 55, doi: [10.1088/0004-637X/791/1/55](https://doi.org/10.1088/0004-637X/791/1/55)
- McKinney, W. 2010, in *Proceedings of the 9th Python in Science Conference*, ed. S. van der Walt & J. Millman, 51 – 56

- McQuillan, A., Mazeh, T., & Aigrain, S. 2014, *ApJS*, 211, 24, doi: [10.1088/0067-0049/211/2/24](https://doi.org/10.1088/0067-0049/211/2/24)
- Meibom, S., & Mathieu, R. D. 2005, *ApJ*, 620, 970, doi: [10.1086/427082](https://doi.org/10.1086/427082)
- Mészáros, S., Allende Prieto, C., Edvardsson, B., et al. 2012, *AJ*, 144, 120, doi: [10.1088/0004-6256/144/4/120](https://doi.org/10.1088/0004-6256/144/4/120)
- Metcalf, A., Anderson, T., Bender, C., et al. 2019, *Optica*, 6, 233, doi: [10.1364/OPTICA.6.000233](https://doi.org/10.1364/OPTICA.6.000233)
- Morales, J. C., Gallardo, J., Ribas, I., et al. 2010, *ApJ*, 718, 502, doi: [10.1088/0004-637X/718/1/502](https://doi.org/10.1088/0004-637X/718/1/502)
- Morales, J. C., Ribas, I., & Jordi, C. 2008, *A&A*, 478, 507, doi: [10.1051/0004-6361:20078324](https://doi.org/10.1051/0004-6361:20078324)
- Morales, J. C., Ribas, I., Jordi, C., et al. 2009, *ApJ*, 691, 1400, doi: [10.1088/0004-637X/691/2/1400](https://doi.org/10.1088/0004-637X/691/2/1400)
- Morgan, D. P., West, A. A., Garcés, A., et al. 2012, *AJ*, 144, 93, doi: [10.1088/0004-6256/144/4/93](https://doi.org/10.1088/0004-6256/144/4/93)
- Morton, T. D. 2012, *ApJ*, 761, 6, doi: [10.1088/0004-637X/761/1/6](https://doi.org/10.1088/0004-637X/761/1/6)
- Morton, T. D., Bryson, S. T., Coughlin, J. L., et al. 2016, *ApJ*, 822, 86, doi: [10.3847/0004-637X/822/2/86](https://doi.org/10.3847/0004-637X/822/2/86)
- Moutou, C., Bonomo, A. S., Bruno, G., et al. 2013, *A&A*, 558, L6, doi: [10.1051/0004-6361/201322201](https://doi.org/10.1051/0004-6361/201322201)
- Mullally, F., Barclay, T., & Barentsen, G. 2016a, K2fov: Field of view software for NASA's K2 mission. <http://ascl.net/1601.009>
- Mullally, F., Coughlin, J. L., Thompson, S. E., et al. 2016b, *PASP*, 128, 074502, doi: [10.1088/1538-3873/128/965/074502](https://doi.org/10.1088/1538-3873/128/965/074502)
- Newton, E. R., Irwin, J., Charbonneau, D., et al. 2017, *ApJ*, 834, 85, doi: [10.3847/1538-4357/834/1/85](https://doi.org/10.3847/1538-4357/834/1/85)
- Nidever, D. L., Holtzman, J. A., Allende Prieto, C., et al. 2015, *AJ*, 150, 173, doi: [10.1088/0004-6256/150/6/173](https://doi.org/10.1088/0004-6256/150/6/173)
- Nielsen, M. B., Gizon, L., Schunker, H., & Karoff, C. 2013, *A&A*, 557, L10, doi: [10.1051/0004-6361/201321912](https://doi.org/10.1051/0004-6361/201321912)
- Ninan, J. P., Bender, C. F., Mahadevan, S., et al. 2018, in *Society of Photo-Optical Instrumentation Engineers (SPIE) Conference Series*, Vol. 10709, Proc. SPIE, 107092U, doi: [10.1117/12.2312787](https://doi.org/10.1117/12.2312787)
- Otegi, J. F., Dorn, C., Helled, R., et al. 2020, *A&A*, 640, A135, doi: [10.1051/0004-6361/202038006](https://doi.org/10.1051/0004-6361/202038006)
- Owen, R. E., Siegmund, W. A., Limmongkol, S., & Hull, C. L. 1994, in *Society of Photo-Optical Instrumentation Engineers (SPIE) Conference Series*, Vol. 2198, Instrumentation in Astronomy VIII, ed. D. L. Crawford & E. R. Craine, 110–114, doi: [10.1117/12.176689](https://doi.org/10.1117/12.176689)
- Pan, Y., Fu, J.-N., Zong, W., et al. 2020, *ApJ*, 905, 67, doi: [10.3847/1538-4357/abc250](https://doi.org/10.3847/1538-4357/abc250)
- Parsons, S. G., Gänsicke, B. T., Marsh, T. R., et al. 2018, *MNRAS*, 481, 1083, doi: [10.1093/mnras/sty2345](https://doi.org/10.1093/mnras/sty2345)
- Parviainen, H., Tingley, B., Deeg, H. J., et al. 2019, *A&A*, 630, A89, doi: [10.1051/0004-6361/201935709](https://doi.org/10.1051/0004-6361/201935709)
- Penoyre, Z., Belokurov, V., Wyn Evans, N., Everall, A., & Koposov, S. E. 2020, *MNRAS*, 495, 321, doi: [10.1093/mnras/staa1148](https://doi.org/10.1093/mnras/staa1148)
- Pepe, F., Mayor, M., Galland, F., et al. 2002, *A&A*, 388, 632, doi: [10.1051/0004-6361:20020433](https://doi.org/10.1051/0004-6361:20020433)
- Perruchot, S., Kohler, D., Bouchy, F., et al. 2008, *Society of Photo-Optical Instrumentation Engineers (SPIE) Conference Series*, Vol. 7014, The SOPHIE spectrograph: design and technical key-points for high throughput and high stability, 70140J, doi: [10.1117/12.787379](https://doi.org/10.1117/12.787379)
- Petigura, E. A., Howard, A. W., Marcy, G. W., et al. 2017, *AJ*, 154, 107, doi: [10.3847/1538-3881/aa80de](https://doi.org/10.3847/1538-3881/aa80de)
- Phillips, M. W., Tremblin, P., Baraffe, I., et al. 2020, *A&A*, 637, A38, doi: [10.1051/0004-6361/201937381](https://doi.org/10.1051/0004-6361/201937381)
- Pont, F., Husnoo, N., Mazeh, T., & Fabrycky, D. 2011, *MNRAS*, 414, 1278, doi: [10.1111/j.1365-2966.2011.18462.x](https://doi.org/10.1111/j.1365-2966.2011.18462.x)
- Rackham, B., Espinoza, N., Apai, D., et al. 2017, *ApJ*, 834, 151, doi: [10.3847/1538-4357/aa4f6c](https://doi.org/10.3847/1538-4357/aa4f6c)
- Rackham, B. V., Apai, D., & Giampapa, M. S. 2018, *ApJ*, 853, 122, doi: [10.3847/1538-4357/aaa08c](https://doi.org/10.3847/1538-4357/aaa08c)
- . 2019, *AJ*, 157, 96, doi: [10.3847/1538-3881/aaf892](https://doi.org/10.3847/1538-3881/aaf892)
- Raghavan, D., McAlister, H. A., Henry, T. J., et al. 2010, *ApJS*, 190, 1, doi: [10.1088/0067-0049/190/1/1](https://doi.org/10.1088/0067-0049/190/1/1)

- Ramsey, L. W., Adams, M. T., Barnes, T. G., et al. 1998, in *Society of Photo-Optical Instrumentation Engineers (SPIE) Conference Series*, Vol. 3352, *Advanced Technology Optical/IR Telescopes VI*, ed. L. M. Stepp, 34–42, doi: [10.1117/12.319287](https://doi.org/10.1117/12.319287)
- Reiners, A., Zechmeister, M., Caballero, J. A., et al. 2018, *A&A*, 612, A49, doi: [10.1051/0004-6361/201732054](https://doi.org/10.1051/0004-6361/201732054)
- Ribas, I. 2003, *A&A*, 398, 239, doi: [10.1051/0004-6361:20021609](https://doi.org/10.1051/0004-6361:20021609)
- Ricker, G. R., Winn, J. N., Vanderspek, R., et al. 2015, *Journal of Astronomical Telescopes, Instruments, and Systems*, 1, 014003, doi: [10.1117/1.JATIS.1.1.014003](https://doi.org/10.1117/1.JATIS.1.1.014003)
- Sahlmann, J., Ségransan, D., Queloz, D., et al. 2011, *A&A*, 525, A95, doi: [10.1051/0004-6361/201015427](https://doi.org/10.1051/0004-6361/201015427)
- Santerne, A., Díaz, R. F., Almenara, J. M., et al. 2015, *MNRAS*, 451, 2337, doi: [10.1093/mnras/stv1080](https://doi.org/10.1093/mnras/stv1080)
- Santerne, A., Moutou, C., Tsantaki, M., et al. 2016, *A&A*, 587, A64, doi: [10.1051/0004-6361/201527329](https://doi.org/10.1051/0004-6361/201527329)
- Serenelli, A., Weiss, A., Aerts, C., et al. 2021, *A&A Rv*, 29, 4, doi: [10.1007/s00159-021-00132-9](https://doi.org/10.1007/s00159-021-00132-9)
- Shetrone, M., Cornell, M. E., Fowler, J. R., et al. 2007, *PASP*, 119, 556, doi: [10.1086/519291](https://doi.org/10.1086/519291)
- Smith, J. C., Stumpe, M. C., Van Cleve, J. E., et al. 2012, *PASP*, 124, 1000, doi: [10.1086/667697](https://doi.org/10.1086/667697)
- Somers, G., & Pinsonneault, M. H. 2015, *ApJ*, 807, 174, doi: [10.1088/0004-637X/807/2/174](https://doi.org/10.1088/0004-637X/807/2/174)
- Speagle, J. S. 2020, *MNRAS*, 493, 3132, doi: [10.1093/mnras/staa278](https://doi.org/10.1093/mnras/staa278)
- Spruit, H. C. 1992, in *Surface Inhomogeneities on Late-Type Stars*, ed. P. B. Byrne & D. J. Mullan, Vol. 397, 78, doi: [10.1007/3-540-55310-X_137](https://doi.org/10.1007/3-540-55310-X_137)
- Stassun, K. G., Kratter, K. M., Scholz, A., & Dupuy, T. J. 2012, *ApJ*, 756, 47, doi: [10.1088/0004-637X/756/1/47](https://doi.org/10.1088/0004-637X/756/1/47)
- Stassun, K. G., & Torres, G. 2021, *ApJL*, 907, L33, doi: [10.3847/2041-8213/abdaad](https://doi.org/10.3847/2041-8213/abdaad)
- Stassun, K. G., Oelkers, R. J., Paegert, M., et al. 2019, *AJ*, 158, 138, doi: [10.3847/1538-3881/ab3467](https://doi.org/10.3847/1538-3881/ab3467)
- Stefánsson, G., Hearty, F., Robertson, P., et al. 2016, *ApJ*, 833, 175, doi: [10.3847/1538-4357/833/2/175](https://doi.org/10.3847/1538-4357/833/2/175)
- Stefánsson, G., Cañas, C., Wisniewski, J., et al. 2020, *AJ*, 159, 100, doi: [10.3847/1538-3881/ab5f15](https://doi.org/10.3847/1538-3881/ab5f15)
- Stevens, D. J., Gaudi, B. S., & Stassun, K. G. 2018, *ApJ*, 862, 53, doi: [10.3847/1538-4357/aaccf5](https://doi.org/10.3847/1538-4357/aaccf5)
- Strassmeier, K. G. 2009, *A&A Rv*, 17, 251, doi: [10.1007/s00159-009-0020-6](https://doi.org/10.1007/s00159-009-0020-6)
- Stumpe, M. C., Smith, J. C., Van Cleve, J. E., et al. 2012, *PASP*, 124, 985, doi: [10.1086/667698](https://doi.org/10.1086/667698)
- Tal-Or, L., Faigler, S., & Mazeh, T. 2015, *A&A*, 580, A21, doi: [10.1051/0004-6361/201526425](https://doi.org/10.1051/0004-6361/201526425)
- Thompson, S. E., Fraquelli, D., Van Cleve, J. E., & Caldwell, D. A. 2016, *Kepler Archive Manual*, Kepler Science Document KDMC-10008-006
- Thompson, S. E., Coughlin, J. L., Hoffman, K., et al. 2018, *ApJS*, 235, 38, doi: [10.3847/1538-4365/aab4f9](https://doi.org/10.3847/1538-4365/aab4f9)
- Torres, G., Andersen, J., & Giménez, A. 2010, *A&A Rv*, 18, 67, doi: [10.1007/s00159-009-0025-1](https://doi.org/10.1007/s00159-009-0025-1)
- Torres, G., & Ribas, I. 2002, *ApJ*, 567, 1140, doi: [10.1086/338587](https://doi.org/10.1086/338587)
- Torres, G., Fressin, F., Batalha, N. M., et al. 2011, *ApJ*, 727, 24, doi: [10.1088/0004-637X/727/1/24](https://doi.org/10.1088/0004-637X/727/1/24)
- Triaud, A. H. M. J., Martin, D. V., Ségransan, D., et al. 2017, *A&A*, 608, A129, doi: [10.1051/0004-6361/201730993](https://doi.org/10.1051/0004-6361/201730993)
- Troup, N. W., Nidever, D. L., De Lee, N., et al. 2016, *AJ*, 151, 85, doi: [10.3847/0004-6256/151/3/85](https://doi.org/10.3847/0004-6256/151/3/85)
- Twicken, J. D., Jenkins, J. M., Seader, S. E., et al. 2016, *AJ*, 152, 158, doi: [10.3847/0004-6256/152/6/158](https://doi.org/10.3847/0004-6256/152/6/158)
- Ulmer-Moll, S., Santos, N. C., Figueira, P., Brinchmann, J., & Faria, J. P. 2019, *A&A*, 630, A135, doi: [10.1051/0004-6361/201936049](https://doi.org/10.1051/0004-6361/201936049)
- Van Cleve, J. E., Christiansen, J. L., Jenkins, J. M., et al. 2016, *Kepler Data Characteristics Handbook*, Kepler Science Document KSCI-19040-005
- van der Walt, S., Colbert, S. C., & Varoquaux, G. 2011, *Computing in Science and Engineering*, 13, 22, doi: [10.1109/MCSE.2011.37](https://doi.org/10.1109/MCSE.2011.37)
- van Roestel, J., Kupfer, T., Bell, K. J., et al. 2021, *ApJL*, 919, L26, doi: [10.3847/2041-8213/ac22b7](https://doi.org/10.3847/2041-8213/ac22b7)

- Virtanen, P., Gommers, R., Oliphant, T. E., et al. 2020, *Nature Methods*, 17, 261, doi: [10.1038/s41592-019-0686-2](https://doi.org/10.1038/s41592-019-0686-2)
- Wandel, A. 2018, *ApJ*, 856, 165, doi: [10.3847/1538-4357/aaae6e](https://doi.org/10.3847/1538-4357/aaae6e)
- West, A. A., Weisenburger, K. L., Irwin, J., et al. 2015, *ApJ*, 812, 3, doi: [10.1088/0004-637X/812/1/3](https://doi.org/10.1088/0004-637X/812/1/3)
- Wheatley, P. J., West, R. G., Goad, M. R., et al. 2018, *MNRAS*, 475, 4476, doi: [10.1093/mnras/stx2836](https://doi.org/10.1093/mnras/stx2836)
- Whitworth, A. 2018, arXiv e-prints, arXiv:1811.06833, <https://arxiv.org/abs/1811.06833>
- Whitworth, A., Bate, M. R., Nordlund, Å., Reipurth, B., & Zinnecker, H. 2007, in *Protostars and Planets V*, ed. B. Reipurth, D. Jewitt, & K. Keil, 459
- Wilson, J. C., Hearty, F., Skrutskie, M. F., et al. 2012, in *Proc. SPIE*, Vol. 8446, *Ground-based and Airborne Instrumentation for Astronomy IV*, 84460H, doi: [10.1117/12.927140](https://doi.org/10.1117/12.927140)
- Wilson, J. C., Hearty, F. R., Skrutskie, M. F., et al. 2019, *PASP*, 131, 055001, doi: [10.1088/1538-3873/ab0075](https://doi.org/10.1088/1538-3873/ab0075)
- Wilson, R. F., Teske, J., Majewski, S. R., et al. 2018, *AJ*, 155, 68, doi: [10.3847/1538-3881/aa9f27](https://doi.org/10.3847/1538-3881/aa9f27)
- Wilson, R. F., Cañas, C. I., Majewski, S. R., et al. 2022, *AJ*, 163, 128, doi: [10.3847/1538-3881/ac3a06](https://doi.org/10.3847/1538-3881/ac3a06)
- Wolfgang, A., Rogers, L. A., & Ford, E. B. 2016, *ApJ*, 825, 19, doi: [10.3847/0004-637X/825/1/19](https://doi.org/10.3847/0004-637X/825/1/19)
- Wood, M. L., Mann, A. W., & Kraus, A. L. 2021, *AJ*, 162, 128, doi: [10.3847/1538-3881/ac0ae910.48550/arXiv.2106.09040](https://doi.org/10.3847/1538-3881/ac0ae910.48550/arXiv.2106.09040)
- Wright, E. L., Eisenhardt, P. R. M., Mainzer, A. K., et al. 2010, *AJ*, 140, 1868, doi: [10.1088/0004-6256/140/6/1868](https://doi.org/10.1088/0004-6256/140/6/1868)
- Wright, J. T., & Eastman, J. D. 2014, *PASP*, 126, 838, doi: [10.1086/678541](https://doi.org/10.1086/678541)
- Zamora, O., García-Hernández, D. A., Allende Prieto, C., et al. 2015, *AJ*, 149, 181, doi: [10.1088/0004-6256/149/6/181](https://doi.org/10.1088/0004-6256/149/6/181)
- Zasowski, G., Cohen, R. E., Chojnowski, S. D., et al. 2017, *AJ*, 154, 198, doi: [10.3847/1538-3881/aa8df9](https://doi.org/10.3847/1538-3881/aa8df9)
- Ziegler, C., Tokovinin, A., Briceño, C., et al. 2020, *AJ*, 159, 19, doi: [10.3847/1538-3881/ab55e9](https://doi.org/10.3847/1538-3881/ab55e9)
- Ziegler, C., Tokovinin, A., Latiolais, M., et al. 2021, *AJ*, 162, 192, doi: [10.3847/1538-3881/ac17f6](https://doi.org/10.3847/1538-3881/ac17f6)
- Ziegler, C., Law, N. M., Morton, T., et al. 2017, *AJ*, 153, 66, doi: [10.3847/1538-3881/153/2/66](https://doi.org/10.3847/1538-3881/153/2/66)
- Ziegler, C., Law, N. M., Baranec, C., et al. 2018, *AJ*, 155, 161, doi: [10.3847/1538-3881/aab042](https://doi.org/10.3847/1538-3881/aab042)
- Zucker, S. 2003, *MNRAS*, 342, 1291, doi: [10.1046/j.1365-8711.2003.06633.x](https://doi.org/10.1046/j.1365-8711.2003.06633.x)